Improvements of Vacuum-assisted Resin Transfer Molding Process and Applications to Composite Structures

陳, 丁丁

https://doi.org/10.15017/1470615

出版情報：九州大学, 2014, 博士（工学）, 課程博士
バージョン：

Improvements of Vacuum-assisted Resin Transfer Molding Process and Applications to Composite Structures

by

DINGDING CHEN

A Dissertation Presented to

Department of Molecular and Material Sciences

Interdisciplinary Graduate School of Engineering Sciences

Kyushu University

June 2014

ABSTRACT

A vacuum-assisted resin transfer molding (VARTM) process was established to fabricate carbon fiber-reinforced polymer (CFRP) structures for a high-strength, lightweight wind-lens power system. Several topics were studied, including experimental methods for basic tests of composite materials, improvements to the VARTM process, and applications for the VARTM process. The chapters are organized as follows.

Chapter 1 provides the background for this dissertation. The VARTM process is described in detail. The main objectives and an outline of this dissertation are briefly introduced.

Chapter 2 introduces the techniques developed for subsequent research on composite materials. A digital image analysis technique was developed to recognize voids from micrographs to evaluate the void content of a specimen. A two-dimensional digital image correlation technique was used to estimate the distribution of the fiber volume fraction of a CFRP plate after determining the area coefficients of thermal expansion (CTEs) of the CFRP samples. A full-field thickness-change monitoring system for the infusion step in the VARTM process was established using a three-dimensional digital image correlation technique. Experimental results were used to validate these techniques, which form the basis of the subsequent research.

Chapter 3 introduces two improvements to VARTM processes. The void content and the fiber volume fraction are two key parameters deciding properties of a composite material. Two primary contributors to void formation, non-uniform resin flow and continuous evaporation of

resin under low pressure, were experimentally studied. Improved pressure control at the vent is proposed to reduce the void content of the manufactured composite material: at the start of the resin infusion, the pressure at the vent is set to the full vacuum of the equipment, while after the resin has saturated all of the reinforcements, the pressure at the vent is increased slightly. With this method, a lower void content is obtained. One the other hand, a cover mold is proposed to be added, inserted between the distribution medium and the peel ply, to achieve a higher fiber volume fraction in the final product. The results demonstrate that there are three advantages to use a cover mold. First, in the filling stage, a rigid cover mold can prevent shrinkage of the part at the resin flow front, and even cause slight expansion of the unsaturated part. Second, a cover mold can limit the amount of excess resin needed to infuse the saturated part. Third, in the post-filling stage, the cover mold can be used to accelerate extrusion of the excess resin in the package. The overall effect is to increase the fiber volume fraction in the final product.

Chapter 4 introduces two applications for VARTM processes. First, two novel joints made from partially un-molded CFRP plates were designed to increase the strength of joints between CFRP parts. In the partially un-molded plate, a portion of the fabric stack was molded with resin while the rest of the fabric stack remained dry. The plate was made using a manufacturing process developed from VARTM. A new double-lap joint sandwiched a normal CFRP plate between the dry fabric layers of a partially un-molded plate. The other laminated joint overlapped the dry fabric layers of two partially un-molded plates. Both joints were molded by resin transfer. Tensile testing indicated that the two novel joints were more than twice as strong

as a classical double-lap joint, and half as strong as a normal, joint-free CFRP plate. Second, a wind-lens was manufactured using VARTM. A simple and low cost method for manufacturing a mold for VARTM is presented. Two-dimensional structures were used to construct a three-dimensional skeleton of a mold. Putty was then applied to the skeleton to obtain a smooth, hard, and strong surface. Finally, a high-elongation plastic film was tightly stretched and attached to the surface of the mold to ensure an airtight seal. The approach was validated by the successful fabrication of a carbon fiber-reinforced plastic part using the mold.

Chapter 5 summarizes the main conclusions of this dissertation and describes possible future major research topics related to this study.

This dissertation starts by describing how to fabricate a high-strength and lightweight "wind-lens" wind-power system, and finishes by fabricating an actual CFRP wind-lens, resulting in a rounded, complete research project on the establishment, development, and application of a VARTM process.

Keywords: VARTM; CFRP; joint; void content; fiber volume fraction; digital image correlation; digital image analysis; infusion monitoring; fabrication of mold.

CONTENTS

CHAPTER 1

Introduction

This chapter provides the background for this dissertation. The VARTM process is described in detail. The main objectives and an outline of this dissertation are briefly introduced.

1.1 General background

The development and application of renewable and clean new energy have become global issues due to the limited supply of fossil fuels and environmental problems caused by their use. Especially in Japan, the application of alternative energy sources is very important, because Japan is, generally, a resource-poor country. Nuclear energy is one alternative energy source, and it has been developed extensively in Japan. Japan generates 30% of its electrical power from nuclear reactors, and had planned to increase that to 40%. However, the Fukushima Daiichi nuclear disaster caused by the earthquake in March 2011 demonstrated the potentially fatal risks when using nuclear power. Other clean energy sources are expected to replace it.

Wind energy is a promising alternative. It is developing rapidly and will play a major role in the new energy field. However, in comparison with the overall demand for energy, the scale of wind power usage is still small; in fact, the level of development in Japan is extremely small. As an island nation, it is difficult to find suitable areas for wind-power plants. At the same time, the complex terrain and the turbulent nature of the local winds make it difficult to apply current wind-power techniques widely in Japan.

To address these problems, a new efficient wind-power turbine system has been developed by a research group at the Division of Renewable Energy Dynamics of the Research Institute for Applied Mechanics, Kyushu University [1-3]. This system has a diffuser shroud at the circumference of its rotor to concentrate the wind energy, as shown in Figure 1-1 and Figure 1-2. This diffuser is called a “wind-lens”. With this system, even low-speed winds can be used for

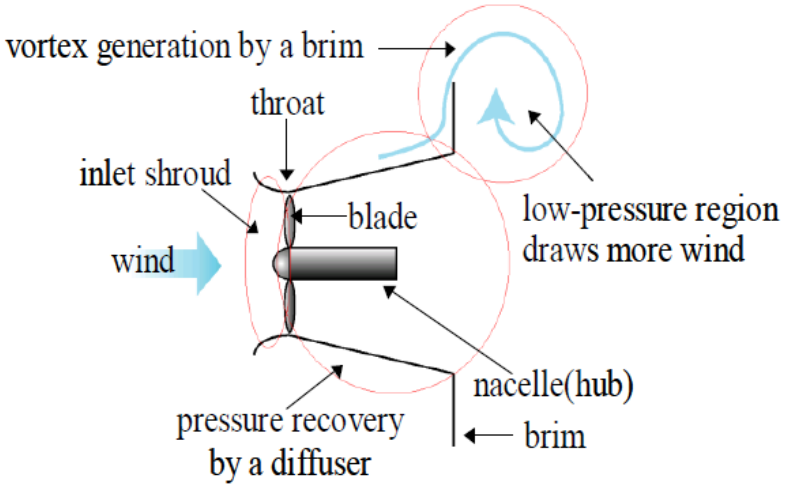

Figure 1-1 Wind power turbine system with a diffuser designed by Kyushu University [3].

Figure 1-2 Photograph of the wind-lens power system.

power. Moreover, a plan for an offshore wind farm is under study. In the future, this wind-power turbine system will likely be used offshore to harness wind power over the sea, as shown in Figure 1-3. Such a wind-power turbine system will be based on a floating structure. Consequently, high-strength and lightweight materials will be required.

Generally, there are three requirements for materials in a turbine system [4]:

1. high material stiffness is needed to maintain optimal aerodynamic performance,
2. low density is needed to reduce gravity forces, and
3. long fatigue life is needed to reduce material degradation.

Fiber-reinforced composite materials are promising candidates. Due to the excellent mechanical properties of some fibers, fiber-reinforced composite materials, combining fibers and a matrix, usually have high stiffness to weight and strength to weight ratios. Consequently, they are attractive for aircraft [5-9] and other vehicle [10-14] applications. Their applications in the wind-energy field are also becoming more appreciated [15-17].

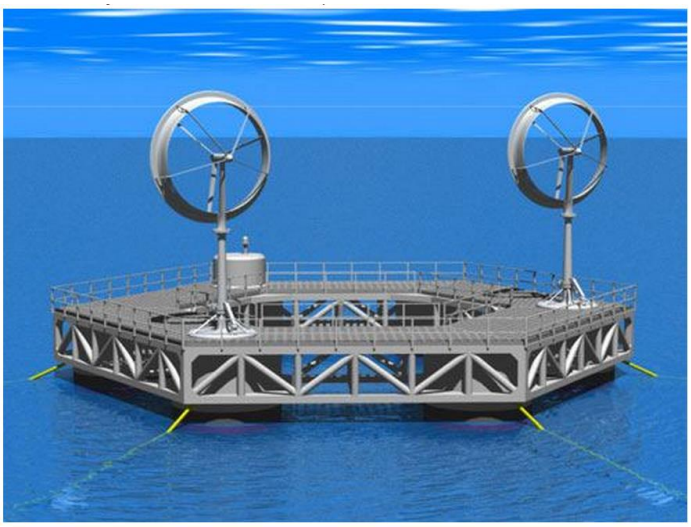

Figure 1-3 Hakata-bay offshore wind farm plan (RIAM offshore wind farm team).

By far, the most widely used fibers are glass fibers, carbon fibers, aramid, polyethylene, and cellulose [4]. Key data for these fibers and their composites are presented in Table 1-1. It is clear that carbon fibers and their composites have excellent combinations of very high stiffness,

Table 1-1 Composite materials based on the fibers listed and a polymer matrix with properties E_m = 3 GPa, σ_m = 100 MPa, and ρ_m = 1.2 g/cm^3. [4]

	Fiber			Composites					
Type	Stiffness E_f GPa	Tensile strength σ_f MPa	Density ρ_f g/cm^3	Volume fraction V_f	Orientation θ	Stiffness E_c GPa	Tensile strength σ_c MPa	Density ρ_c g/cm^3	Merit $E_c^{1/2}/\rho_c$
Glass-E	72	3500	2.54	0.5	0°	38	1800	1.87	3.3
				0.3	Random	9.3	420	1.60	1.9
Carbon	350	4000	1.77	0.5	0°	176	2050	1.49	8.9
				0.3	Random	37	470	1.37	4.4
Aramid	120	3600	1.45	0.5	0°	61	1850	1.33	5.9
				0.3	Random	14.1	430	1.27	2.9
Polyethylene	117	2600	0.97	0.5	0°	60	1350	1.09	7.1
				0.3	Random	13.8	330	1.13	3.3
Cellulose	80	1000	1.50	0.5	0°	41	550	1.35	4.7
				0.3	Random	10.1	170	1.29	2.5

high strength, and low density. Therefore, carbon-fiber reinforced composites (CFRPs) would be useful for fabricating a wind-lens for a wind-power generating system at sea.

To date, several techniques have been developed for manufacturing composite structures, such as the wet hand-lay-up process, prepreg technology, and resin-infusion processes. The wet hand-lay-up technique is the traditional technique for building boats in open molds, and has been used for decades. This technique has also been used to fabricate a wind turbine blade as early as the 1950s [18]. A problem with this technique is that it is not easy to control the properties of the final product.

Prepreg technology, such as the autoclave process shown in Figure 1-4, is based on the use of a semi-raw product where the fiber fabrics are pre-impregnated with resin that has not yet cured. At room temperature, the resin is like a tacky solid, and the tacky prepregs can be stacked on top of each other to build the desired laminate. By increasing the temperature, the resin becomes viscous, and the laminate can be consolidated under pressure and cured into a final component. Using this technique, it is relatively easy to control and obtain constant materials properties and higher fiber content. Consequently, prepreg technology is widely used in the aerospace and aircraft industry. An autoclave is generally required to increase the temperature, making the resin viscous, and to provide high pressure, obtaining a high fiber volume fraction; this limits the size of the finished product. The low flowability of the prepreg process also makes it difficult to prepare complex structures. Prepreg, itself, is also expensive, making this a very high-cost technology.

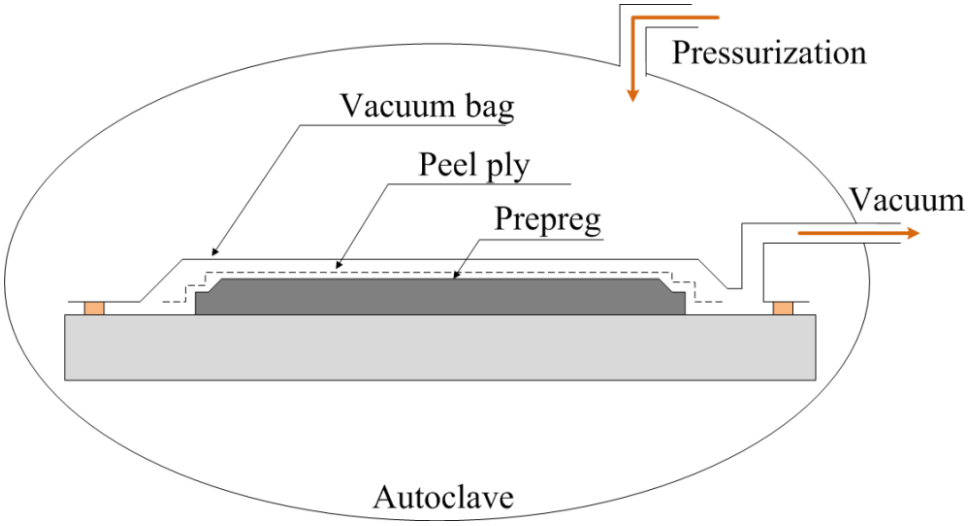

Figure 1-4 Illustration of a autoclave process.

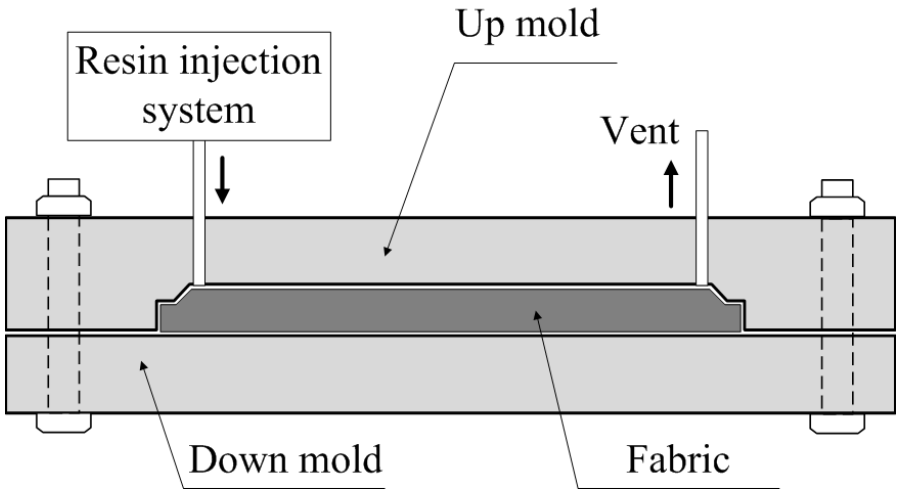

Figure 1-5 Illustration of a RTM process.

Resin infusion molding (RTM), shown in Figure 1-5, is a relatively low cost process compared with prepreg technology. It involves placing dry fibers in a mold, encapsulating and sealing off the fiber package, injecting the liquid resin into the package, and curing the components. Depending on the resin, an autoclave is unnecessary. Moreover, flexible dry fibers, instead of prepreg, are used in this process. Consequently, it is easy to make large and complex

structures using this technology. The most important issue in the process is to ensure that all fibers are thoroughly wetted with the resin to avoid spots with dry fibers in the finished product.

Each technology has its own advantages and disadvantages. The choice of method will determine the quality and cost of the final wind-lens power system.

1.2 Introduction of the VARTM process

Vacuum-assisted resin transfer molding (VARTM) process was developed from RTM process in which a solid closed mold is used to seal the liquid resin. In VARTM processes, an open solid mold with flexible vacuum bag tape-sealed is used to replace the closed mold as shown in Figure 1-6.

In a VARTM process, reinforcements are stacked on a solid mold which is prepared with release agent, and covered by a peel ply and a distribution medium. They are enclosed together with an inlet and a vent in a vacuum bag and sealed with tape. Figure 1-7 shows a photograph of a vacuum package in our experiments. After drawing vacuum in the package, the resin can be infused from the inlet by the pressure difference between the inside and the outside of the package. After the reinforcement is completely infused, the inlet is closed. In order to get a higher fiber volume fraction, the vent is usually left open to extrude the extra resin inside the vacuum package until the resin becomes too viscous to flow. After the resin cures, a laminate composite is obtained after demolding process.

A release agent painted on a solid mold and peel ply are used to separate the final product from the other layers. Without them, the final composite product will attach to the mold and the

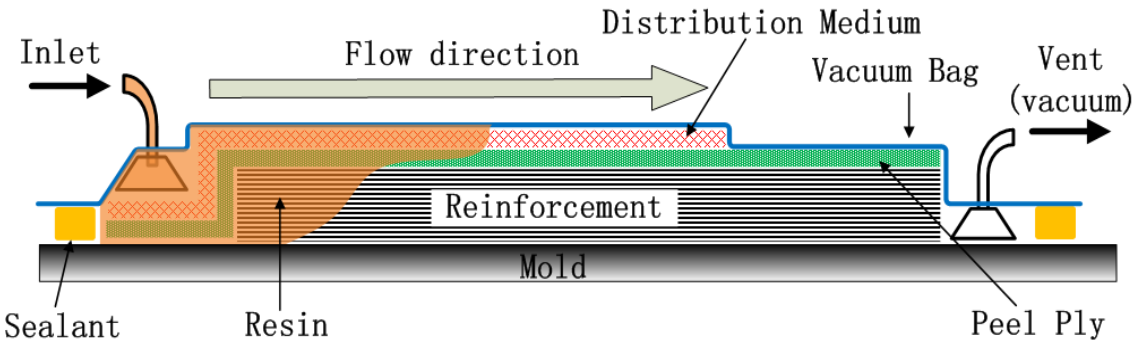

Figure 1-6 Illustration of a VARTM process.

Figure 1-7 Photograph of the package in a VARTM process.

distribution medium, making the demolding process very difficult. Because the infusion pressure is only 1 atmosphere, the infusion speed inside the reinforcement is very slow. For large and thick parts, the vacuum level may not be sufficient to complete the infusion. Consequently, a distribution medium is often required [19-21], such as a plastic mesh, which has much higher in-plane permeability than a fabric stack, allowing for fast surface resin wet-out. Subsequent resin penetration allows for complete infusion. A spiral tube is often used

in the inlet and vent structures to make a point inlet (and vent) become a line inlet (and vent). It is critical to choose the location of the vent appropriately to completely infuse the reinforcement and avoid creating resin-starved regions near the vent locations after the inlet is closed.

Because only a simple single-sided mold and fabric, instead of prepreg, are required, the most important advantages of VARTM processes are their relatively low costs and the ability to manufacture large-scale composite parts with complex shapes. A problem with the process is that the void content of the fabricated composite part is higher and the fiber volume fraction is lower than products made by other common processes, such as with an autoclave. The void content usually remains in the range of 2-5%. The nominal fiber volume fraction is dependant on the preform architecture, but is typically in the range of 50-60% [22].

1.3 Objective and outline

1.3.1 Objective and outline

After comparing the processes for manufacturing CFRP structures, the VARTM process seems promising for fabricating a wind-lens power system. Focusing on this target, a VARTM process platform was developed. To obtain a high-quality wind-lens power system using CFRP material through a VARTM process, research on improving and applying VARTM was performed and is described in this dissertation.

The outline of this dissertation is as follows.

Chapter 1 introduces the background and the target of this research. The commonly used VARTM process is introduced in detail because it forms the basis of this research.

Chapter 2 develops techniques to analyze the fabrication processes and the composite products. The void and fiber volume fractions are two key physical properties of a fiber-reinforced composite material. A digital image analysis technique was developed to estimate the void content. A two-dimensional digital image correlation technique was used to estimate the distribution of the fiber volume fraction for a composite plate. And, a three-dimensional digital image correlation test system was established to monitor the full-field thickness evolution during the infusion step.

Chapter 3 focuses on improvements to achieve lower void content composites and higher fiber volume fraction. Pressure control in the vent is proposed to reduce the void content. An additional rigid cover mold is proposed, inserted between the peel ply layer and the distribution medium to increase the fiber volume fraction.

Chapter 4 introduces some applications for the VARTM process. Novel joints based on the VARTM process are proposed to improve the connection properties between composite parts. Fabrication trials for a wind-lens for a power system are described.

Chapter 5 summarizes the major results of this dissertation.

1.3.2 Materials used

Resin and fiber fabric are the basic materials used in VARTM processes. The resin used throughout the experiments in this dissertation was XNR6815, with XNH6815 hardener from Nagase & Co., Ltd. This is an epoxy resin that can be cured at room temperature. The initial viscosity of the resin mixed with hardener is 260 mPa•s s at 25°C. The pot life (2× the initial

viscosity) is 100 min. The fiber fabrics used throughout the experiments in this dissertation were from Saertex GmbH & Co., KG. The key parameters of the three stitched carbon-fiber fabrics that were primarily used are listed in Table 1-2.

Table 1-2 Key parameters of mainly used carbon fiber fabrics.

Style	Construction			Total areal weigth (g/m^2)
	Direction	Material	Areal weight (g/m^2)	
[90°]	90°	TENAX STS	504	511
[+30°/–30°]	+30°	TENAX HTS40 F13 12K	220	449
	–30°	TENAX HTS40 F13 12K	220	
[+45°/0°/-45°/90°]	+45°	TENAX IMS60 24K	263	1074
	0°	TENAX IMS60 24K	267	
	-45°	TENAX IMS60 24K	263	
	90°	TENAX IMS60 24K	275	

Bibliography

[1] Abe K-i, Ohya Y. An investigation of flow fields around flanged diffusers using CFD. Journal of Wind Engineering and Industrial Aerodynamics. 2004;92(3–4):315-330.

[2] Abe K, Nishida M, Sakurai A, Ohya Y, Kihara H, Wada E, et al. Experimental and numerical investigations of flow fields behind a small wind turbine with a flanged diffuser. Journal of Wind Engineering and Industrial Aerodynamics. 2005;93(12):951-970.

[3] Ohya Y, Karasudani T. A Shrouded Wind Turbine Generating High Output Power with Wind-lens Technology. Energies. 2010;3(4):634-649.

[4] Brøndsted P, Lilholt H, Lystrup A. COMPOSITE MATERIALS FOR WIND POWER TURBINE BLADES. Annual Review of Materials Research. 2005;35(1):505-538.

[5] Thuis HGSJ. Development of a composite cargo door for an aircraft. Composite Structures. 1999;47(1–4):813-819.

[6] Shokrieh MM, Taheri Behrooz F. Wing instability of a full composite aircraft. Composite Structures. 2001;54(2–3):335-340.

[7] Okafor AC, Singh N, Enemuoh UE, Rao SV. Design, analysis and performance of adhesively bonded composite patch repair of cracked aluminum aircraft panels. Composite Structures. 2005;71(2):258-270.

[8] Murugan S, Saavedra Flores EI, Adhikari S, Friswell MI. Optimal design of variable fiber spacing composites for morphing aircraft skins. Composite Structures. 2012;94(5):1626-1633.

[9] Kapidžić Z, Nilsson L, Ansell H. Finite element modeling of mechanically fastened composite-aluminum joints in aircraft structures. Composite Structures. 2014;109(0):198-210.

[10] Schouwenaars R, Cerrud S, Ortiz A. Mechanical analysis of fracture in an automotive radiator head produced from a nylon–glass fiber composite. Composites Part A: Applied Science and Manufacturing. 2002;33(4):551-558.

[11] Corum JM, Battiste RL, Ruggles-Wrenn MB. Low-energy impact effects on candidate automotive structural composites. Composites Science and Technology. 2003;63(6):755-769.

[12] Ruggles-Wrenn MB, Corum JM, Battiste RL. Short-term static and cyclic behavior of two automotive carbon-fiber composites. Composites Part A: Applied Science and Manufacturing. 2003;34(8):731-741.

[13] Lee DG, Sung Kim H, Woon Kim J, Kook Kim J. Design and manufacture of an automotive hybrid aluminum/composite drive shaft. Composite Structures. 2004;63(1):87-99.

[14] Lee SW, Lee DG. Composite hybrid valve lifter for automotive engines. Composite Structures. 2005;71(1):26-33.

[15] Tseng Y-C, Kuo C-Y. Engineering and Construction Torsional Responses of Glass-Fiber/Epoxy Composite Blade Shaft for A small Wind Turbine. Procedia Engineering. 2011;14(0):1996-2002.

[16] Lanting Z. Research on Structural Lay-up Optimum Design of Composite Wind Turbine Blade. Energy Procedia. 2012;14(0):637-642.

[17] Kim T, Hansen AM, Branner K. Development of an anisotropic beam finite element for composite wind turbine blades in multibody system. Renewable Energy. 2013;59(0):172-183.

[18] U. H. Tragende Flugzeugteile aus glasfaserverstarkten Kunststoffen. Luftfahrttechnik. 1960;6(2):34-44.

[19] Chohra M, Advani SG, Gokce A, Yarlagadda S. Modeling of filtration through multiple layers of dual scale fibrous porous media. Polymer Composites. 2006;27(5):570-581.

[20] Gokce A, Chohra M, Advani SG, Walsh SM. Permeability estimation algorithm to simultaneously characterize the distribution media and the fabric preform in vacuum assisted resin transfer molding process. Composites Science and Technology. 2005;65(14):2129-2139.

[21] Simacek P, Advani SG. Modeling resin flow and fiber tow saturation induced by distribution media collapse in VARTM. Composites Science and Technology. 2007;67(13):2757-2769.

[22] Li W, Krehl J, Gillespie Jr JW, Heider D, Endrulat M, Hochrein K, et al. Process and performance evaluation of the vacuum-assisted process. Journal of Composite Materials. 2004;38(20):1803-1814.

CHAPTER 2

Techniques for analyzing manufacturing processes and products

---

This chapter introduces the techniques developed for subsequent research on composite materials. A digital image analysis technique was developed to recognize voids from micrographs to evaluate the void content of a specimen. A two-dimensional digital image correlation technique was used to estimate the distribution of the fiber volume fraction of a CFRP plate after determining the area coefficients of thermal expansion (CTEs) of the CFRP samples. A full-field thickness-change monitoring system for the infusion step in the VARTM process was established using a three-dimensional digital image correlation technique. Experimental results were used to validate these techniques, which form the basis of the subsequent research.

2.1 Introduction

The evaluation of composite materials is one of the most important parts of composites research. Two of the most critical parameters in evaluating a composite material are the fiber volume fraction and the void content. The fiber volume fraction directly determines the strength, especially the strength-to-weight ratio, of a composite material. A high fiber volume fraction leads to high strength. However, voids have negative effects on the modulus and strength of composite materials [1–3]. Therefore, to evaluate fabricated composites, techniques for measuring the fiber volume fraction and the void content are essential.

There are two standard methods for calculating the fiber volume fraction [4]. One is removing the matrix component with a hot-liquid medium [5] or a furnace [6]. Then, the weight ratio can be measured, and the fiber volume fraction can be calculated from the density of each component. In practice, this method is complex. The most important issue is that the method destroys the material. The other method is calculating the thickness of the composite material and the density of the reinforcing components. However, a composite sample fabricated using a VARTM process usually has only one smooth surface, making it difficult to measure the thickness accurately.

Consequently, there is a need for a non-destructive method that can estimate the fiber volume fraction, or even provide a rough distribution. This would be useful for assessing of VARTM fabricated composite products.

For the test of the void content, widely used method is the calculation through the weight

ratio, tested through hot liquid dissolution [5] or ignition method [6, 7], and the density of each component. The material studied in this research was a carbon-fiber-reinforced plastic (CFRP). Unlike glass fiber, carbon fiber can be burned in air. Consequently, it is difficult to accurately calculate the void content from the fiber volume fraction measured by ignition methods. Image analysis of gray micrographs of CFRP specimens is another method to estimate the void content and examine the configuration of voids. Figure 2-1 shows a typical micrograph of the studied CFRP material. The magnification time is 500. The resolution of the images was ca. 1 μm/pixel. Figure 2-1 shows that the voids and other features have different gray levels; consequently, an appropriate intensity threshold is widely used to automatically extract the voids. However, this simple operation cannot readily distinguish some spurious void-like features from real voids [8, 9]. Figure 2-2 is obtained after removing the points in Figure 2-1 whose gray values were higher than 60. There are many spurious void-like features, which derived from two primary sources: the stitched thread borders and fiber shadows. Because the resin is much softer than the carbon fiber, polishing causes the fibers to be slightly higher than the surrounding resin, leading to a shadow around them in the micrographs. Consequently, in order to image the voids correctly, the image processing procedure should be improved.

On the other hand, the fiber volume fraction and the void content of the VARTM manufactured product are strongly affected by the flow of resin in the infusion step. A comprehensive understanding of this flow is essential for engineering better materials. Thickness of the reinforcement is one of the most important factors reflecting the saturation

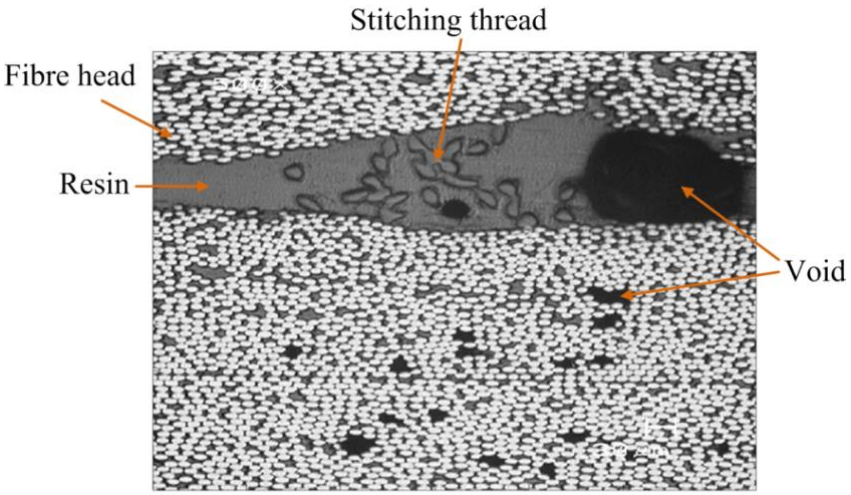

Figure 2-1 Typical micrograph of a CFRP specimen

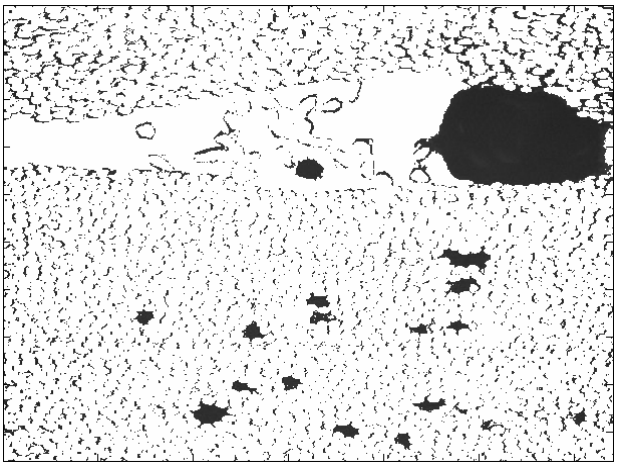

Figure 2-2 Figure 2-1 processed only using gray levels.

state and has been widely studied [10-13]. Conventional techniques for measuring thickness, such as linear variable differential transformers (LVDTs) [10] and laser displacement sensors [14], obtain the thickness at several independent points. Bickerton et al. [15-17] developed a digital speckle stereophotogrammetry system that acted as a full-field test system to monitor the thickness evolution of the entire package. With this system, the full-field thickness change can be recorded during the resin infusion process.

In this chapter, a modified digital image analysis procedure for estimating the void content is introduced. A two-dimensional digital image correlation (2D-DIC) technique was used to estimate the fiber volume fraction distribution of a VARTM fabricated CFRP plate. A full-field monitoring system for recording the thickness evolution of the vacuum package was established using a three-dimensional digital image correlation (3D-DIC) technique. These techniques form the basis of the subsequent research.

2.2 Digital image analysis to estimate void content

2.2.1 Sample preparation

For optical microscopy, a high magnification results in a small depth of field. To obtain a micrograph like that in Figure 2-1, specimens must be ground and polished carefully to prepare a very smooth surface. Before grinding, CFRP specimens are usually mounted in some material (Figure 2-3), such as a resin block, to provide a large volume than be readily held in the hand. The surface will tend to become spherical after polishing; a large volume makes the curvature smaller.

The grinding and polishing processes follow the procedure outlined in Table 2-1. Some noteworthy points and tips are listed below.

1. One of the most important objectives of the first step is to remove the mounting material on the specimens. After this step, the surface of the CFRP specimen should be exposed, instead of covered by the mounting material.
2. In each step, any scratches made in the previous step must be removed completely.

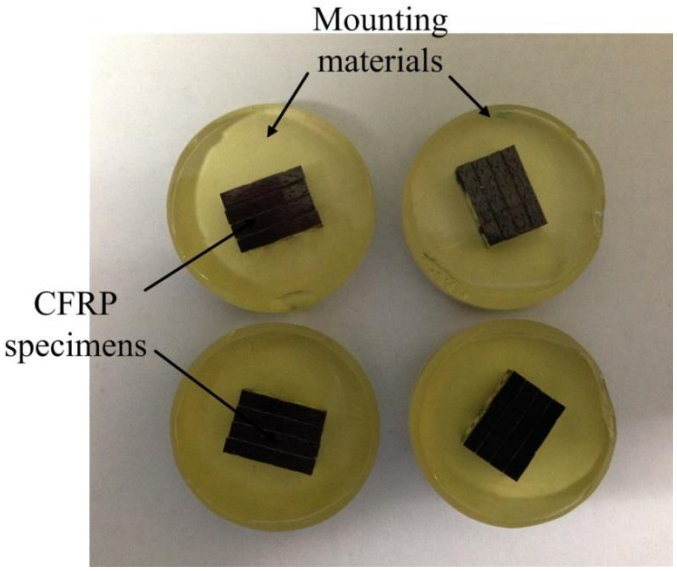

Figure 2-3 CFRP specimens are mounted in resin blocks.

Table 2-1 Grinding and polishing procedure

Step	Polishing Material	Particle Size
1	Sandpaper P800 (#400)	21.8 μm
2	Sandpaper P1200 (#600)	15.3 μm
3	Sandpaper P2000 (#1000)	10.3 μm
4	Sandpaper P2400	8 μm
5	Sandpaper P4000 or Levigated alumina polishing compound on microcloth	5 μm
6	Monocrystalline diamond suspension on microcloth	3 μm

Consequently, the polishing direction is suggested to be different with respect to the direction used in the previous step, making it easy to check the effect of the polishing in the current step. In the first three steps, only scratches visible with the naked eye need to be removed. From the fourth step onwards, the scratches must be examined using a microscope.

3. After each step, the polished specimen must be cleaned carefully using ultrasonic cleaning. In the first three steps, the washing medium can be normal tap water. From Step 4 onwards, it is better to use purified water.

2.2.2 Calculation of void content

In order to image the voids from micrographs correctly, the entire image processing procedure is divided into three steps.

In the first step, the area comprising the real void and its vicinity are extracted. The most obvious difference between a void-like feature and a real void is the size. The voids are typically very large, while void-like features appear as thin lines. Consequently, a gray value criterion and a size criterion are used simultaneously. Before processing, a new matrix, *M*, with the same size of the original image matrix, *I*, is created. In the new matrix, each element is set to 225. To identify a point in *I*, a small square subset ($N_1 \times N_1$) centered at the point is checked by comparing the gray value of all the points in the subset with a threshold (t_1). If the percentage of the points whose gray values are lower than t_1 in the subset is higher than a critical value (P), then the center point is identified as a real void. Once a point is identified as a void, another subset ($N_2 \times N_2$) centered at the point in *I* is copied to the new matrix, *M*, at the same position. After scanning all the points in *I*, *M* is updated and becomes the image in which only the real void area and its vicinity remained. For Figure 2-1, N_1 is set to 7 pixels, t_1 is fixed at 55, P is set to 80%, and N_2 is set to 13 pixels. After this procedure, Figure 2-4(a) is obtained.

In the second step, the matrix and the fibers are removed by simply setting a gray value

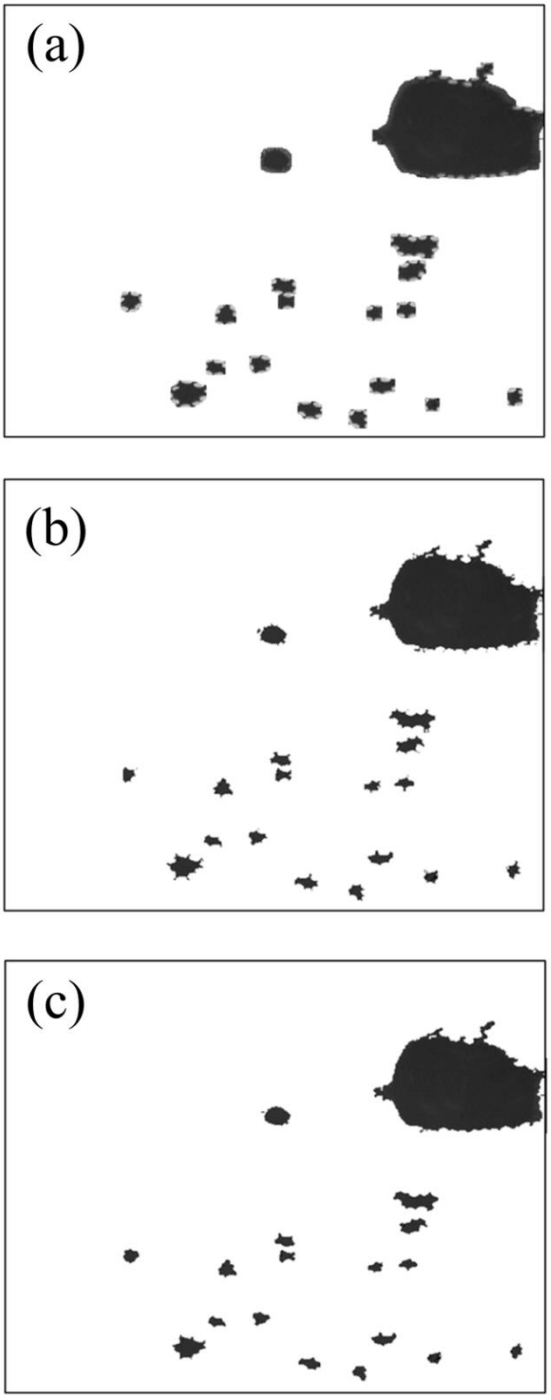

Figure 2-4 Micrographs after improved processing procedures. (a) Real voids and the vicinity are extracted. (b) Fibers and resin are removed from (a). (c) Thin branches at the edge of the void area in (b) are erased.

threshold based on the processed result after Step 1. For Figure 2-4(a), the gray value threshold is set to 60, i.e., removing all the points whose gray value is higher than 60. Figure 2-4(b) shows the result after Step 2. However, once the gray threshold is set, many thin branches still

exist at the edge of the void area, as shown in Figure 2-4(b). These are the shadows of fibers rather than real voids.

In the final Step 3, the thin branches are erased using a similar method as the first step. For Figure 2-4(b), N_1 is set to 5 pixels, t_1 is fixed at 60, and P is set to 40%. Step 3 differs from Step 1 as follows: if P exceeds 40%, then the point, not a subset centered on the point, is retained. Figure 2-4(c) shows the image after Step 3.

In the fully processed image of Figure 2-4(c), the percentage of the black area is considered as the void content of the specimen. To reduce the effect of location on a real calculation, a section larger than 150 × 2 mm^2, composed of more than 120 images having the same resolution as Figure 2-1, should be analyzed for each specimen.

Figure 2-5 shows the void distributions along the infusion direction for a VARTM fabricated CFRP plates. The horizontal axis indicates the distance from the inlet. The blue triangles are the void results estimated using the digital image analysis technique. The black square points were calculated using Equation (2-1):

$$f_{void} = \frac{V_{void}}{V} = \left(\frac{\rho_f^s}{\rho_r} - \frac{\rho_f^s}{\rho_f^v}\right)\frac{1}{h} - \frac{\rho_{CFRP}}{\rho_r} + 1 \qquad (2\text{-}1)$$

where ρ_f^s and ρ_f^V are the areal and volume densities of the fabric, respectively, h is the thickness of the samples, and ρ_r and ρ_{CFRP} are the volume density of the resin and the CFRP samples, respectively. The volume density is determined according to the ASTM D792 standard. For each position, at least three pieces of specimens are cut and measured, and the average

density is calculated. The areal density of the fabric is obtained from the supplier's technical data sheet rather than by measuring; this may have introduced some error in the calculations. For Figure 2-5, the results estimated from the digital image analysis technique and from Equation (2-1) are in good agreement, thus validating the digital image analysis technique for the estimation of void content.

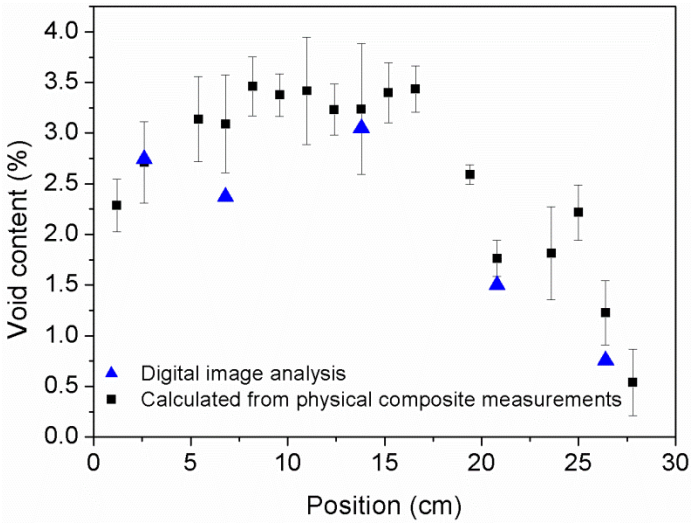

Figure 2-5 Comparison of void content distributions of a VARTM manufactured CFRP plate tested through digital image analysis technique and calculation from physical measurements

2.3 2D-DIC technique for estimating the fiber volume fraction

2.3.1 2D-DIC technique

A sketch of the 2D-DIC technique is shown in Figure 2-6. This method recognizes the same point in two pictures taken before and after the deformation of an object by using correlation equations. Then, it compares the positions of the point in the two pictures to determine the

displacement [18]. A small subset ($N \times M$) centered at pixel point $P(X,Y)$ on the undeformed object image is used to obtain an estimate of the displacement of point P. The intensity values of all points in the subset ($N \times M$) on the undeformed image are compared with those of other subsets on the deformed image using the following equation:

$$C(X+u,Y+v)=\sum_{i=-M}^{M}\sum_{j=-M}^{M}\left|I_d(X+u+i,Y+v+j)-I_u(X+u,Y+v)\right| \tag{2-2}$$

where $N = 2M + 1$, C is a correlation function, I_d and I_u are the intensity values of a point on the deformed and undeformed images, respectively, and u and v are the displacement components in the x and y directions, respectively. The values of u' and v' that minimize C are assumed to be roughly the displacements in pixels. Thus, the precision of the result is only 1 pixel. With some further analysis [19], precision better than 1 pixel can be achieved. Then, using the relationship between a pixel and the real length, the displacement can be obtained with a higher degree of precision.

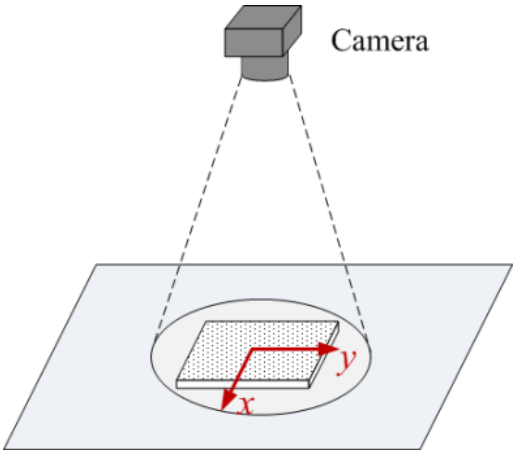

Figure 2-6 Sketch of the 2D-DIC method.

2.3.2 Estimation of the fiber volume fraction

It is known that carbon fiber and the resin have totally different coefficients of thermal expansion (CTEs). Different fiber volume fractions may result in different CTEs. The distribution of the fiber volume fraction was estimated by measuring the area CTEs.

A VARTM fabricated CFRP plate was tested to validate the proposed methodology. The reinforcement consisted of five layers of stitched [+30°/–30°] fabric. The thickness of the plate was ca.2 mm, and the length was ca.290 mm (Figure 2-7). Rectangular specimens were cut from the plate for the tests. The inlet and the vent indicated the infusion direction in the VARTM process. Each specimen was ca.14 mm wide and ca.42 mm long.

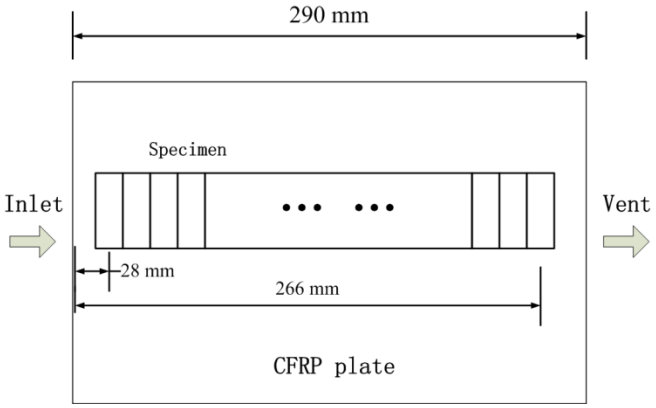

Figure 2-7 Location of specimens.

A sketch of the setup for measuring the CTE is shown in Figure 2-8. Specimens were placed on a heater and covered by a transparent glass plate. A smooth plastic plate was placed in between the specimen and the heater to reduce the friction of the interface. A transparent glass plate was used to press the specimens to prevent warp deformation. The upper surfaces of the

specimens were painted with random patterns to perform the DIC tests. A camera was used to take pictures of the specimens before and after they were heated. The room temperature was 13°C, and the target specimen temperature was set to 30°C. For each specimen, the displacements of 2,201 points located uniformly on the surface were measured using the 2D-DIC technique.

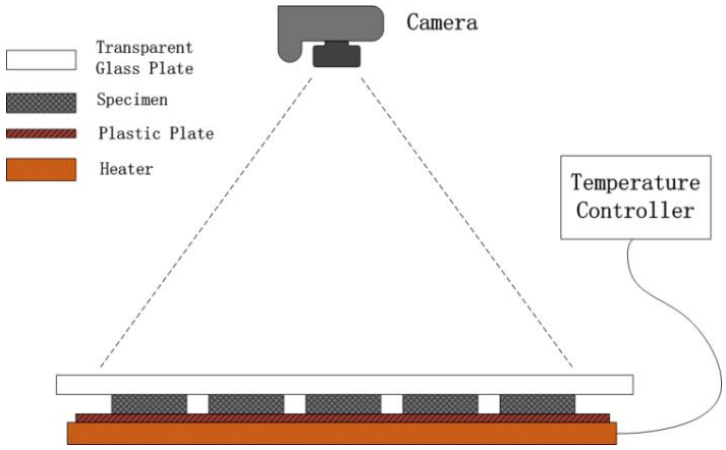

Figure 2-8 Setup for the CTE test.

Strain is the displacement derivative of position, as defined in the following equations:

$$\varepsilon_x = \frac{\partial \delta_x}{\partial x}$$
$$\varepsilon_y = \frac{\partial \delta_y}{\partial y} \quad (2\text{-}3)$$

where ε_x and ε_y are the strains in the x and y directions, respectively, and δ_x and δ_y are the displacements in the x and y directions, respectively. One of the simplest methods to calculate the strain from displacement results is to use the finite difference method. However, this method usually leads to a large error. To obtain an accurate result for the strain of a point, quadric

surface equations were adopted to fit the displacement results of the area in the vicinity of each point as follows:

$$\begin{aligned} \delta_x &= a_0 + a_1 x + a_2 x^2 + a_3 xy + a_4 y + a_5 y^2 \\ \delta_y &= b_0 + b_1 x + b_2 x^2 + b_3 xy + b_4 y + b_5 y^2 \end{aligned} \tag{2-4}$$

The parameters a_i and b_i (i = 1, 2, …, 5) can be fixed through a least-squares procedure using the displacement results of the target point and its ambient points (Figure 2-9). Combining Equations (2-3) and (2-4), the strain can be calculated from

$$\begin{aligned} \varepsilon_x &= a_1 + 2a_2 x + a_3 y \\ \varepsilon_y &= b_3 x + b_4 + 2b_5 y \end{aligned} \tag{2-5}$$

The area strain is the sum of ε_x and ε_y,

$$\varepsilon = \varepsilon_x + \varepsilon_y \tag{2-6}$$

Then, the CTE of the specimen is

$$CTE = \frac{\varepsilon_{ave}}{\Delta T}, \tag{2-7}$$

where ε_{ave} is the average area strain of all the points on the specimen.

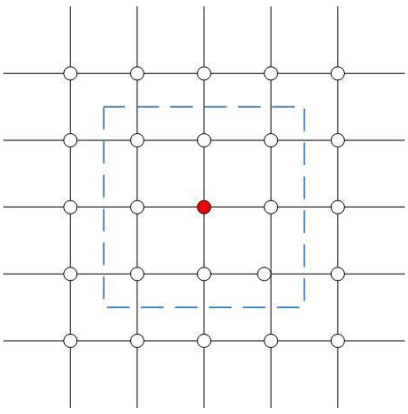

Figure 2-9 Illustration of the calculation of strain.

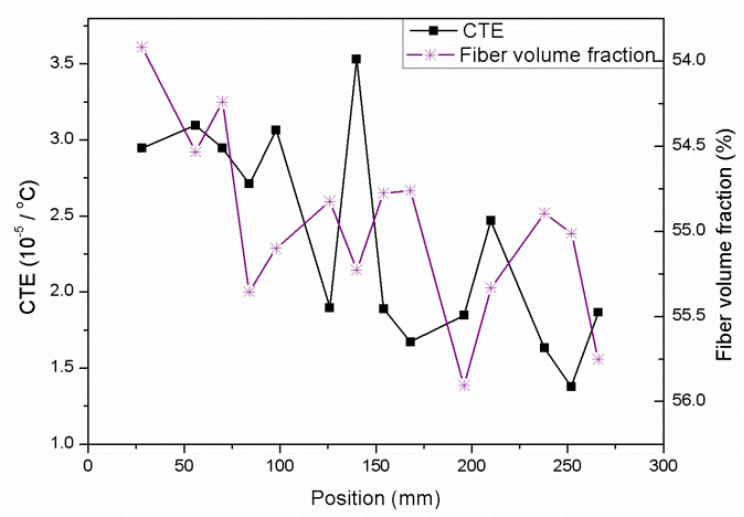

Figure 2-10 CTE and fiber volume fraction results.

Figure 2-10 shows the results for the CTE and fiber volume fraction. The lateral axis shows the distance from the edge of the CFRP plate near the inlet to the specimen location on the plate (Figure 2-7). The fiber volume fractions of the specimens were calculated roughly using the following equation:

$$f_{fiber} = \frac{n \cdot \rho_f^s}{\rho_f^V \cdot h} \quad , \tag{2-8}$$

where n is the number of fabric layers and ρ_f^s and ρ_f^V are the area and volume densities of the fabric, respectively. h is the thickness of the samples, determined using a micrometer. To emphasize the relationship between the CTE and the fiber volume fraction, the scale of the fiber volume fraction on the graph was inverted, spanning from 56.3% to 53.8%. This graph shows that from the inlet to the vent, the CFRP plate had an increasing fiber volume fraction distribution. The specimens near the inlet had a higher CTE. To ensure the reliability of the tests, the CTEs were measured three times. The results are shown in Figure 2-11. Although the results

of each specimen differed slightly, the three tests showed the same distribution, indicating that the tendency was reliable.

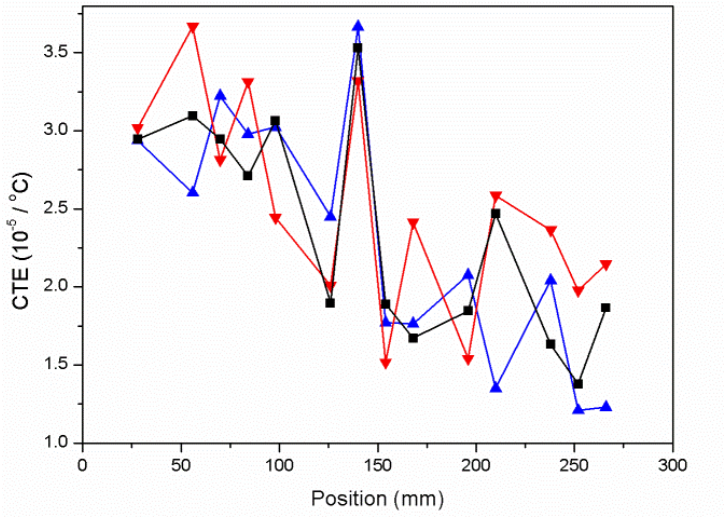

Figure 2-11 Repeatability results from three tests.

The fiber volume fraction distribution in Figure 2-10 seems reasonable because the resin concentrations in the vicinity of the inlet in the resin-infusion stage of the VARTM process usually lead to a larger thickness. The order of the CTE of the resin was 10^{-5} /°C. The coefficient of the fibers was slightly less than 10^{-6}/°C. When a CFRP specimen is heated, the resin component should expand faster than the fibers. However, the small amount of expansion and the high tensile modulus of the fibers will restrict the resin expansion. When the fiber content is higher, this restriction will be stronger. Consequently, a specimen with a higher CTE should have a lower fiber volume fraction, consistent with the relationship seen in Figure 2-10. Additionally, from Figure 2-10, the CTE is sensitive to the fiber volume fraction. From the inlet to the vent, the fiber volume fraction only increases by about 3%; however, the CTE decreases

by nearly 50%, emphasizing the high sensitivity of the method.

Consequently, a CTE test using the 2D-DIC technique provides a feasible non-destructive method of evaluating of the fiber volume fraction distribution in a CFRP plate.

2.4 3D-DIC technique for testing thickness change of the vacuum package in VARTM

2.4.1 3D-DIC technique

Based on the 2D-DIC technique, a 3D–DIC system is constructed using two cameras, which are used to simultaneously monitor an object (Figure 2-12). A spatial coordinate system (*X*, *Y*, *Z*) was constructed for the object, in which the *z*-axis was vertical to the plane, and two plane coordinates (*U*, *V*) were constructed on the camera charge-coupled device (CCD) surface. A displacement of the object (*x*, *y*, *z*) in the spatial coordinate system causes a displacement in the two camera coordinate systems (u_1, v_1) and (u_2, v_2). When the displacement is small, u_i and v_i (i = 1 and 2) can be considered as an overlap of three independent effects caused by *x*, *y*, and *z*, respectively, as expressed by

$$\begin{aligned} u_i &= f_{uxi}(x) + f_{uyi}(y) + f_{uzi}(z) \\ v_i &= f_{vxi}(x) + f_{vyi}(y) + f_{vzi}(z) \end{aligned}, \quad i = 1 \text{ and } 2, \tag{2-9}$$

where the expressions of f are quadratic equations of *x*, *y*, and *z*, respectively [20, 21]. The detailed expression is

$$\begin{aligned} u_i &= a_{ui,x}x^2 + b_{ui,x}x + a_{ui,y}y^2 + b_{ui,y}y + a_{ui,z}z^2 + b_{ui,z}z + c_{ui} \\ v_i &= a_{vi,x}x^2 + b_{vi,x}x + a_{vi,y}y^2 + b_{vi,y}y + a_{vi,z}z^2 + b_{vi,z}z + c_{vi} \end{aligned}, \quad i = 1 \text{ and } 2. \tag{2-10}$$

In each equation, there are seven undetermined parameters. With seven known sites, the

parameters can be fixed. Then, during testing, a displacement of the object (x', y', z') can be calculated by solving Equation (2-10) using the displacements (u_1', v_1') and (u_2', v_2') recorded by the cameras.

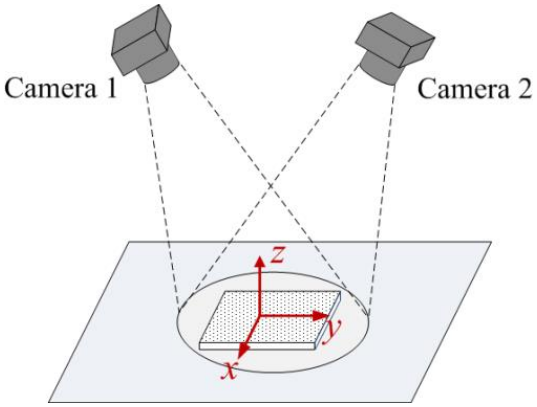

Figure 2-12 Sketch of the 3D-DIC method

2.4.2 Thickness change test system for VARTM

A test system for the thickness change of the vacuum package in VARTM processes is established using 3D-DIC technique as shown in Figure 2-13. Two cameras with the solution of 2592 × 1944 pixels are focused on the vacuum package and are computer-controlled to acquire images simultaneously. Z axis of the spatial coordinate system for the object is along the thickness change direction of the vacuum package. Random patterns are painted on the transparent vacuum bag to assist with the image recognition in the DIC analysis. Two experiments were designed to validate the thickness-change test system. One involved calibrating the system accuracy. The other consisted of measuring the thickness evolution of the vacuum package during vacuum loading–release cycles. The reinforcement used in these two

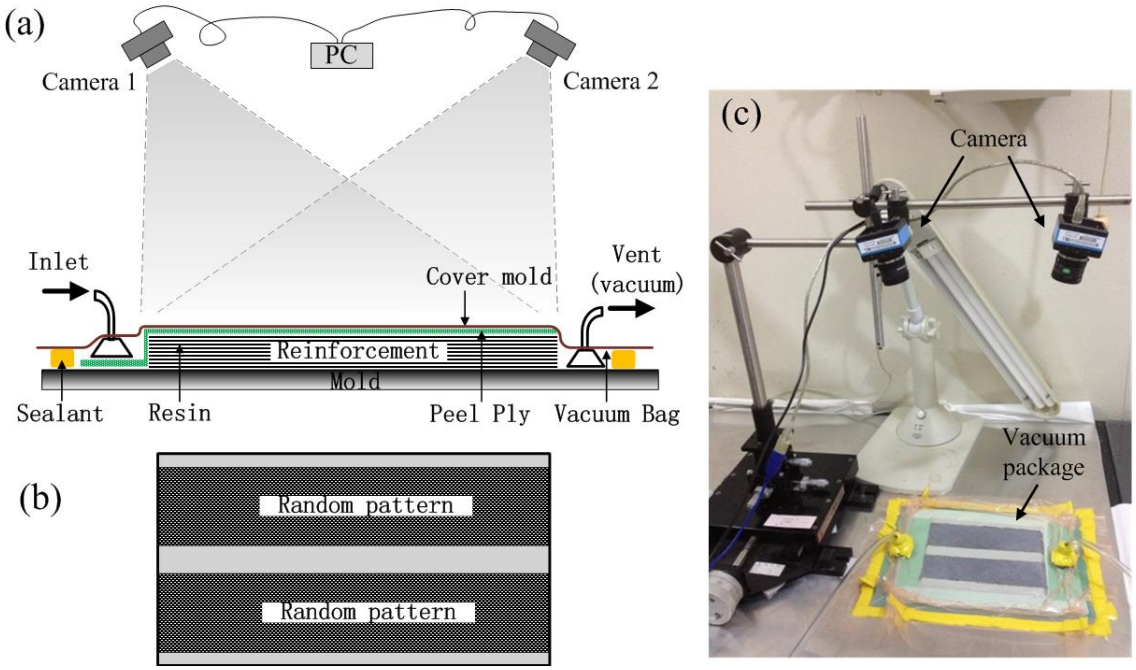

Figure 2-13 (a) Schematic diagram showing the VARTM process with the 3D DIC test system. (b) Top view of the vacuum package. (c) Photo of setup in experiment.

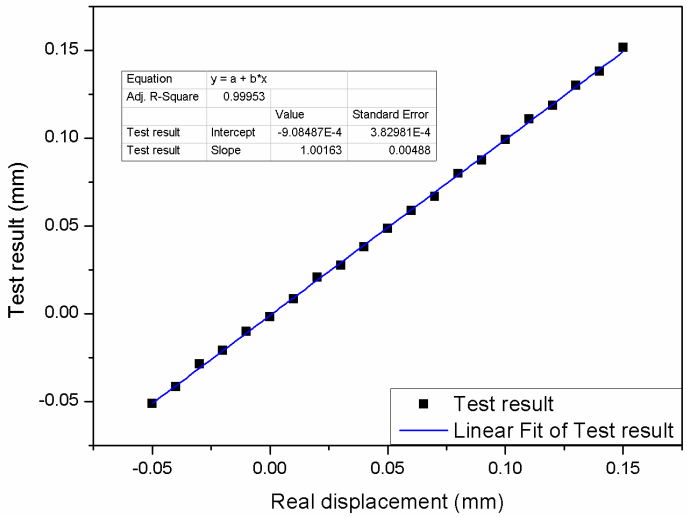

Figure 2-14 Calibration results for the 3D DIC test system.

tests consisted of eight layers of stitched [+30◦/–30◦] fabric.

The precision of the 3D-DIC system was assessed through the following procedure. The

cameras were moved up 0.05 mm, and then moved down 0.2 mm in steps of 0.01 mm. For the test system, an effect equal to this operation would be the displacement of the package from –0.05 mm to 0.15 mm in steps of 0.01 mm. A test result for one point on the random pattern is shown in Figure 2-14. The average calculated step length is 0.0099 mm and the variance is 0.002 mm. Thus, the 3D–DIC system is deemed satisfactorily accurate.

A vacuum loading–release cycle was performed in the vacuum package (Figure 2-13). The initial pressure inside the package was 87.5 kPa. Thus, the pressing load was 13.8 kPa. The package was drawn to full vacuum in steps of 13.8 kPa, with a final pressing load of 101.3 kPa. In each step, the pressure was kept constant for at least 10 min to allow the system to become stable. After this, the package was released to 87.5 kPa (the pressing load returned to 13.8 kPa) following the same procedure. After the system became stable again, the package was reloaded to full vacuum. The thickness change caused by the change of pressure was measured using the 3D-DIC system. Figure 2-15 shows the thickness evolution. The initial thickness when the stack was at 87.5 kPa was set as the reference state. The thickness evolution caused by the loading–release cycles was fitted as follows:

Loading stage: $d = -0.369\ln(P) + 0.988$

Relaxation stage: $d = -0.0897\ln(P) - 0.3$

Reloading stage: $d = 0.0024P - 0.495$

where d is the thickness change and P is the pressure difference between the inside and the

outside of the package. The fitted results are also shown in Figure 2-15. The resulting relationship between the thickness and the pressure was complex. It was affected by the loading mode (from low to high pressure or from high to low pressure) and by the number of cycles. The results show that the cycle loads help compact the stack more tightly and achieve a thinner thickness. Reference [22] reported essentially the same results.

Thus, the 3D-DIC thickness-change test system had a high level of accuracy and could reflect the thickness change in the vacuum package during VARTM.

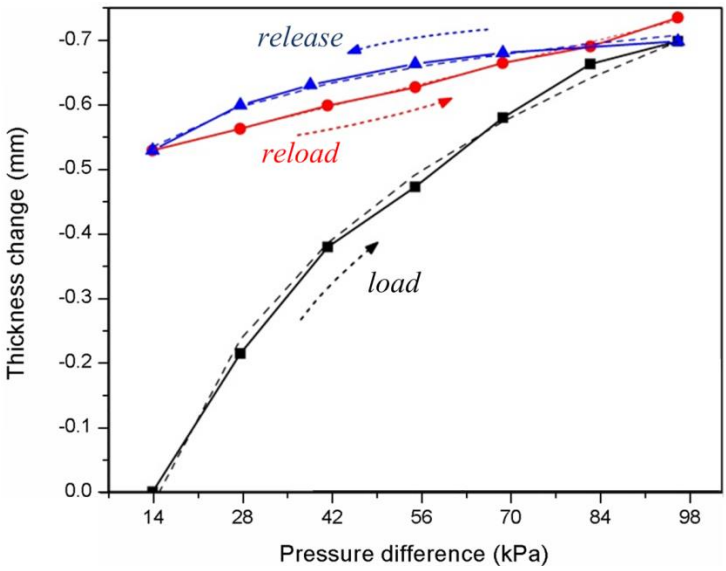

Figure 2-15 Thickness evolution and fitting results.

Bibliography

[1] Chen D, Arakawa K. Mechanical properties of a VARTM manufactured 2D carbon woven/expoxy composite. The 8th International Forum on Advanced Material Science and Technology, Fukuoka, Japan2012. p. 169.

[2] Huang H, Talreja R. Effects of void geometry on elastic properties of unidirectional fiber reinforced composites. Composites Science and Technology. 2005;65(13):1964-1981.

[3] Hagstrand PO, Bonjour F, Månson JAE. The influence of void content on the structural flexural performance of unidirectional glass fibre reinforced polypropylene composites. Composites Part A: Applied Science and Manufacturing. 2005;36(5):705-714.

[4] ASTM. Standard Test Methods for Constituent Content of Composite Materials. vol. ASTM D31712011.

[5] International A. Standard Test Method for Matrix Solids Content and Matrix Content of Composite Prepreg. vol. ASTM D3529M West Conshohocken, PA2010.

[6] ASTM. Standard Test Method for Ignition Loss of Cured Reinforced Resins. vol. D25842011.

[7] Kedari VR, Farah BI, Hsiao K-T. Effects of vacuum pressure, inlet pressure, and mold temperature on the void content, volume fraction of polyester/e-glass fiber composites manufactured with VARTM process. Journal of Composite Materials. 2011;45(26):2727-2742.

[8] Santulli C, Gil RG, Long AC, Clifford MJ. Void content measurements in commingled E-glass/polypropylene composites using image analysis from optical micrographs. Science and

Engineering of Composite Materials. 2002;10(2):77-90.

[9] Paciornik S, D'Almeida JRM. Measurement of Void Content and Distribution in Composite Materials through Digital Microscopy. Journal of Composite Materials. 2009;43(2):101-112.

[10] Simacek P, Eksik Ö, Heider D, Gillespie Jr JW, Advani S. Experimental validation of post-filling flow in vacuum assisted resin transfer molding processes. Composites Part A: Applied Science and Manufacturing. 2012;43(3):370-380.

[11] Simacek P, Heider D, Gillespie Jr JW, Advani S. Post-filling flow in vacuum assisted resin transfer molding processes: Theoretical analysis. Composites Part A: Applied Science and Manufacturing. 2009;40(6–7):913-924.

[12] Correia NC, Robitaille F, Long AC, Rudd CD, Šimáček P, Advani SG. Analysis of the vacuum infusion moulding process: I. Analytical formulation. Composites Part A: Applied Science and Manufacturing. 2005;36(12):1645-1656.

[13] Šimáček P, Advani SG. Desirable features in mold filling simulations for Liquid Composite Molding processes. Polymer Composites. 2004;25(4):355-367.

[14] Yenilmez B, Sozer EM. Compaction of e-glass fabric preforms in the vacuum infusion process: (a) use of characterization database in a model and (b) experiments. Journal of Composite Materials. 2013;47(16):1959-1975.

[15] Timms J, Bickerton S, Kelly PA. Laminate thickness and resin pressure evolution during axisymmetric liquid composite moulding with flexible tooling. Composites Part A: Applied Science and Manufacturing. 2012;43(4):621-630.

[16] Govignon Q, Bickerton S, Kelly PA. Simulation of the reinforcement compaction and resin flow during the complete resin infusion process. Composites Part A: Applied Science and Manufacturing. 2010;41(1):45-57.

[17] Govignon Q, Bickerton S, Morris J, Kelly PA. Full field monitoring of the resin flow and laminate properties during the resin infusion process. Composites Part A: Applied Science and Manufacturing. 2008;39(9):1412-1426.

[18] Sutton M, McNeill S, Helm J, Chao Y. Advances in Two-Dimensional and Three-Dimensional Computer Vision. In: Rastogi P, editor. Photomechanics, vol. 77 Berlin Heidelberg: Springer 2000. p. 323-372.

[19] Uchino M. Sub-micron displacement measurement using a digital image correlation method. ATEM, Nagoya, Japan: The Japan Society of Mechanical Engineers; 2003. p. No.03-207.

[20] Uchino M, Yamaguchi T. 3-Dimensional Deformation Measurement Using Digital Image Correlation Method. JSEM 2006 Annual Conference on Experimental Mechanics, vol. 6 Kasugai, Japan: The Japanese Society for Experimental Mechanics; 2006. p. 77-80.

[21] Uchino M, Yamaguchi T. 3D deformation Measurement using Digital Image Correlation Method. the 2005 Annual Meeting of the JSME/MMD, vol. 5 Fukuoka, Japan: The Japan Society of Mechanical Engineers; 2005. p. 357-358.

[22] Yang JS, Xiao JY, Zeng JC, Jiang DZ, Peng CY. Compaction Behavior and Part Thickness Variation in Vacuum Infusion Molding Process. Appl Compos Mater. 2012;19(3-4):443-458.

CHAPTER 3
Improvements to VARTM processes

This chapter introduces two improvements to VARTM processes. The void content and the fiber volume fraction are two key parameters deciding properties of a composite material. Two primary contributors to void formation, non-uniform resin flow and continuous evaporation of resin under low pressure, were experimentally studied. Improved pressure control at the vent is proposed to reduce the void content of the manufactured composite material: at the start of the resin infusion, the pressure at the vent is set to the full vacuum of the equipment, while after the resin has saturated all of the reinforcements, the pressure at the vent is increased slightly. With this method, a lower void content is obtained. One the other hand, a cover mold is proposed to be added, inserted between the distribution medium and the peel ply, to achieve a higher fiber volume fraction in the final product. The results demonstrate that there are three advantages to use a cover mold. First, in the filling stage, a rigid cover mold can prevent shrinkage of the part at the resin flow front, and even cause slight expansion of the unsaturated part. Second, a cover mold can limit the amount of excess resin needed to infuse the saturated part. Third, in the post-filling stage, the cover mold can be used to accelerate extrusion of the excess resin in the package. The overall effect is to increase the fiber volume fraction in the final product.

3.1 Introduction

VARTM is a technique that is widely used for molding complicated composite structures, such as those used in marine vessels and next-generation airplanes [1]. VARTM has the advantages of ease of operation and low cost. While promising, VARTM still suffers from a relatively low fiber volume fractions and a high void content in the final products.

For a composite material, the presence of voids usually negatively affects its mechanical properties such as tensile, flexural, and fatigue strengths [2-6]. Therefore, extensive research has been conducted to correlate void formation with VARTM processes [7-11].

In liquid composite molding (LCM) processes, air entrapped by the non-uniform flow of resin is one of the most important sources of voids. At the micro level, voids are generated by the different flow speeds of resin inside and between fiber tows. These flows are governed by Darcy's law and capillary interaction, respectively [12-14]. When the flow between tows is faster, voids will appear inside the fiber tows. Based on this knowledge, Kedari [10] controlled the temperature and pressure difference between the inlet and vent to optimize the ratio between the velocities inside and between fiber tows and thereby reduced the void content. At the macro level, voids are generated by a non-uniform flow-front of resin [15, 16]. Techniques have been developed to monitor the flow of resin [17-19] and simulate the resin infusion process [20-22]. To achieve a uniform flow-front and thereby reduce the void content, an induction heating technique [20, 21], a novel injection line consisting of multiple segments [23], and some other methods [24] have been proposed.

However, in a vacuum-assisted LCM process, the low pressure induces another source of voids: evaporation of resin. In the VARTM process, there are a great number of liquid-solid interfaces where nucleation can readily take place. These nuclei develop into bubble embryos. Once the bubble embryos become larger than the critical size for bubble growth, they continue to grow [25, 26]. Many bubbles can be nucleated and grow at the fiber–matrix interface in VARTM processes because of the vacuum employed [27]. The generated bubbles become voids in the final product.

The fiber volume fraction directly affects the properties of composite materials. A high fiber volume fraction usually leads to high strength. In VARTM processes, the volume of reinforcement is fixed. Consequently, the fiber volume fraction is determined by the amount of resin, depending on the infused resin less the extruded amount. However, few studies have considered increasing the fiber volume fraction.

In this chapter, methods are proposed to decrease the void content and increase the fiber volume fraction. Controlling the infusion pressure is proposed to minimize void formation stemming from entrapped air and resin evaporation to improve the VARTM process, based on studying the factors that lead to void formation. The resin flow in the resin-infusion process is also considered. Based on an understanding of the resin flow, a cover mold inserted between the peel ply and the distribution medium is proposed to promote the resin flow and increase the fiber volume fraction in the final product.

3.2 Reduction of void content

3.2.1 Formation of voids

(a) Effect of entrapped air

Figure 3-1 shows the experimental setup used to study the formation of voids from entrapped air in the VARTM process. A chamber, 120 × 280 × 5 mm^3 in size, as shown in Figure 3-1(b), was fabricated to simulate a stack of reinforcements. The chamber was made of transparent poly(methyl methacrylate) (PMMA) so that the resin inside the chamber could be observed clearly. An additional PMMA bar was placed in the center of the chamber to divide it into two parts. Holes were drilled in the right and left walls of the chamber to allow the resin to flow in

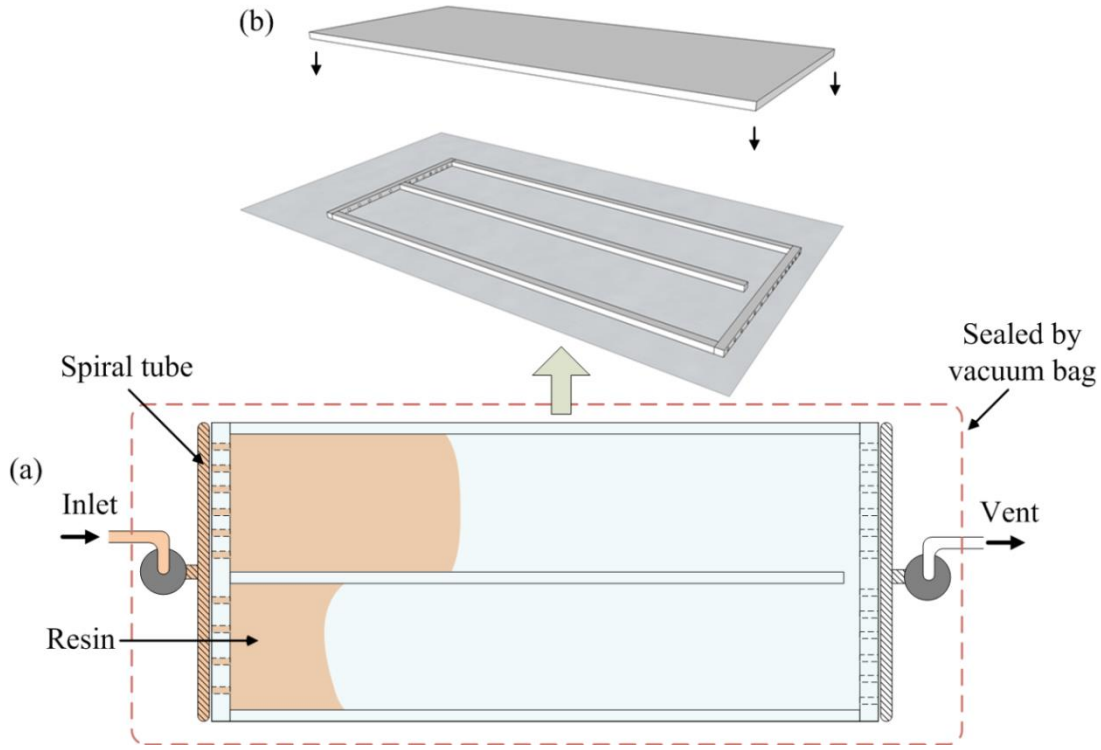

Figure 3-1 (a) Sketch of experimental setup used to study void formation caused by entrapped air. (b) Structure of the chamber.

and out. To obtain different flow velocities, more holes were drilled in the upper part. The inlet and the vent for infusion were made from a rubber connector and a segment of spiral tube. The whole chamber, including the spiral tube and connectors, was sealed in a vacuum bag.

The pressure at the inlet was normal atmospheric. The pressure at the vent was controlled at 50 kPa, which implied that there was still some air in the chamber. Figure 3-2 shows the details of the resin flow. Because of the special design of the inlet, the resin flowed much more quickly in the upper part of the chamber (Figure 3-2(b)). After it reached the end of the upper part, the resin flowed into the lower part (Figure 3-2(c) and (d)), thereby entrapping a large amount of air and generating a very large bubble. The bubble shrank to a constant size (Figure 3-2(f)). Because the bubble moved too slowly to flow out of the chamber, the entrapped air became a

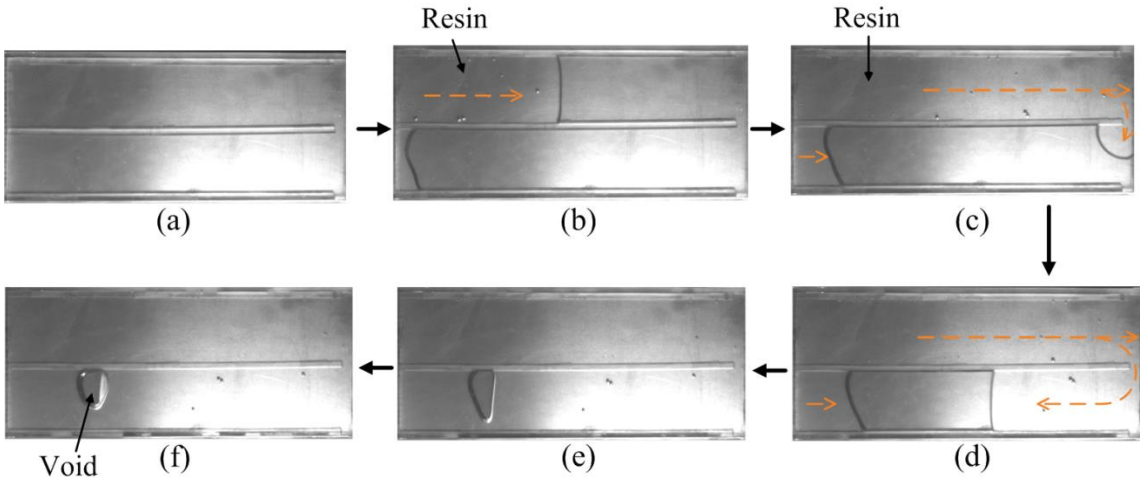

Figure 3-2 Void formation caused by entrapped air. (a) Before infusion. (b) Beginning of infusion. (c) Resin in the upper part of the chamber flows into the lower part. (d) Air is entrapped by resin. (e) Bubble shrinks. (f) Void forms.

void in the cured resin. After the bubble formed, it continued to shrink until it reached a constant size, instead of disappearing, because of its air content. If the chamber was under full vacuum, the phenomenon of entrapped air could be avoided. However, full vacuum has its own negative effects.

(b) Effect of low pressure

The primary negative effect of low pressure in the VARTM process is the evaporation of resin. Figure 3-3 shows the experiment used to examine the evaporation phenomenon of resin under a vacuum. A U-shaped tube was filled with resin, and one end was sealed while the other end was connected to a vacuum pump. Drawing vacuum in the tube led to evaporation of the resin. Gas generated in the resin stored in the right part of the tube was collected at the end of the tube. The height of the space (L) was used to represent the degree of evaporation of the resin. The U-shaped tube was made of soft plastic so that it was easy to change the shape of the tube to obtain a constant liquid level difference (d). The outer and inner diameters of the tube were 14 and 10 mm, respectively. The tube was bound tightly with several loops to limit deformation caused by the pressure difference between the inside and outside of the tube, as shown in Figure 3-3(b). Resin (60 mL, mixed with hardener) was used in the tests. The amount of air generated over 2 min was recorded to estimate the evaporation speed. The evaporated gas was removed from the tube after each 2 min measurement, and thus L was reset to 0 each time. During the tests, the liquid level difference, d, was maintained at 10 mm.

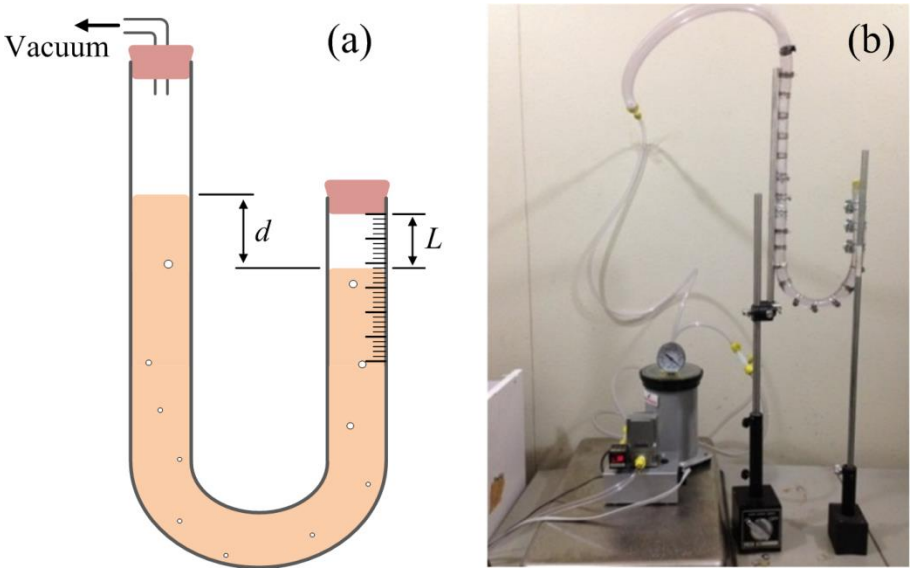

Figure 3-3 Experimental setup used to study resin evaporation.

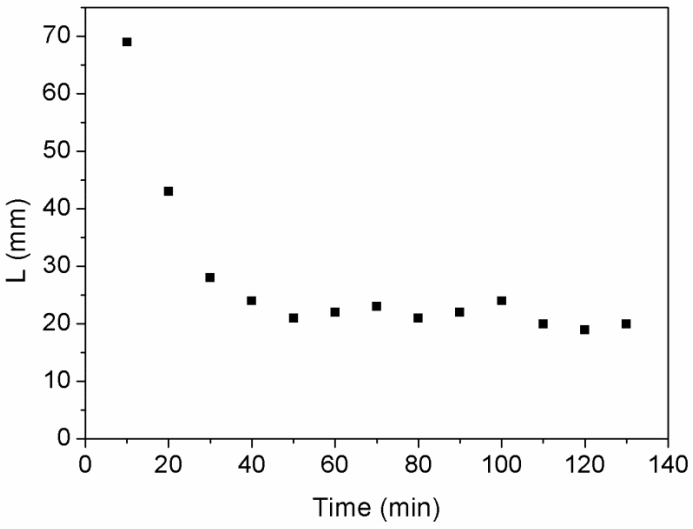

Figure 3-4 Results of resin evaporation.

Figure 3-4 shows the results of an evaporation test. *L* presents the amount of air generated over each 2 min. The evaporation speed was quite high initially, but decreased quickly. After 30 min, the evaporation reached a constant speed: about 20 mm of air collected in the tube every two minutes. The high evaporation speed at the beginning was probably caused by the air

dissolving in the resin. The dissolved air was removed at low pressure. However, the amount of the air was limited, and so it had no effect on the evaporation speed later in the tests. The constant evaporation speed after 30 min showed that evaporation, which has the potential to generate voids, cannot be avoided in a normal VARTM process, whether the resin is degassed or not.

3.2.2 Reduction of void content

Four VARTM processes were designed to further study void formation. Some key details are shown in Table 3-1. The experimental equipment and the structure of the vacuum package in the four cases are illustrated in Figure 3-5. Reinforcements (20 × 30 cm^2), composed of five layers of the [30°/–30°] stitched carbon fiber fabric, were stacked in a solid mold and covered with a peel ply and a 0.5-mm-thick aluminum plate that made the top surface of the manufactured CFRP plate smooth. The stack consisting of the fabric, peel ply, and aluminum plate was partially covered by a distribution medium to promote the flow of the resin. The distance between the end of the distribution material and the end of the stack was 65 mm. To allow the resin to flow from the distribution medium to the reinforcement, the aluminum plate was perforated (Figure 3-6); the hole diameter was 1 mm and the distance between two neighboring holes was 2 mm. The inlet and the vent were located on either side of the stack. The infused resin was stored in a container at atmospheric pressure (ca. 101.3 kPa). The vacuum chamber connected to the vent had two functions. First, the chamber was used to store the extra resin extruded from the vacuum package. Second, the chamber was used to control the pressure at the

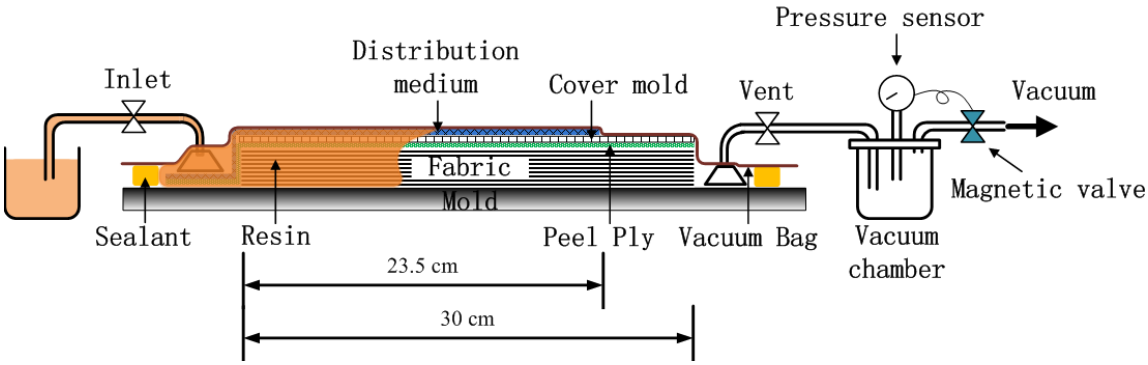

Figure 3-5 Schematic diagram of the VARTM process used in the experiments.

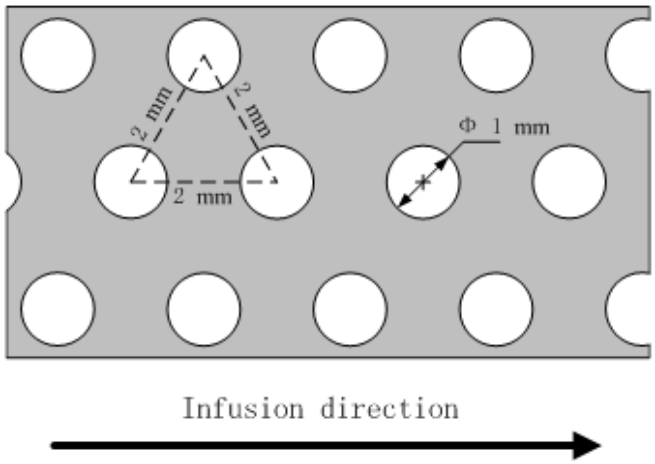

Figure 3-6 Perforation pattern of the cover plates.

vent to a desired value set by a digital pressure sensor (E8F2–AN0B, OMRON Corporation) and a magnetic valve (BN–7M21–8A, Nihon Seiki Co., Ltd.).

The main differences between the four cases were the pressure at the vent and the degassing pressure. In Case *A*, the resin was degassed at a pressure of 8.3 kPa for 2 h before mixing with hardener. After mixing, the mixture was degassed for another 15 min at the same pressure. During the infusion process, the pressure at the vent (the same as the pressure in the vacuum

Table 3-1 Details of four fabrication processes designed to minimize the void content.

Case	Degassing pressure, kPa	Inlet pressure, kPa	Vent pressure, kPa	Time inlet was closed, min	Time vent was closed, min
A	8.3	101.3	15.3	29	150
B	8.3	101.3	ca. 0	19	150
C	ca. 0	101.3	ca. 0	19	150
D	ca. 0	101.3	ca. 0 → 15.3 at 16 min	19	150

*The times when the inlet and the vent were closed were referenced to the initial opening of the inlet.

package) was 15.3 kPa. The inlet was closed at 29 min when the resin began to flow out from the vent. The vent was closed at 2 h 30 min. The times at which the inlet and the vent were closed were referenced to the initial opening of the inlet. In this case, the evaporation of resin was reduced and some air was introduced into the package, emphasizing the effect of entrapped air on void formation. In Case *B*, the resin was degassed following the same procedure. However, the pressure at the vent was set to a high vacuum level (ca. 0 kPa) so that there was almost no air remaining in the package. This avoided the phenomenon of entrapped air. The resin flowed much faster because of the higher pressure difference between the inlet and the vent. Consequently, the inlet was closed after a shorter time, i.e., 19 min. This case was designed to examine the effect of evaporation on void formation. In Case *C*, the resin was degassed at a pressure of ca. 0 kPa for 2 h before mixing with hardener. After mixing, the mixture was degassed for another 15 min at the same pressure. The pressure at the vent was also

set to 0 kPa. Case *C* is a widely used procedure. Case *D* was designed to obtain the lowest void content in the manufactured composite. In this case, the resin was degassed following the same procedure as for Case *C*. At the beginning of the infusion, the pressure at the vent was nearly 0 kPa. At about 16 min, when the resin had saturated the entire stack and had reached the vent, the pressure at the vent was switched to 15.3 kPa. The inlet was closed at 19 min and the vent was closed at 2 h 30 min.

Figure 3-7 and Figure 3-8 show the void distributions along the infusion direction for the fabricated Cases *A* and *B* CFRP plates, respectively. The horizontal axis indicates the distance from the inlet. The blue triangles are the void results estimated using the method described in Section 2. The black square points were calculated using Equation (2-1).For each position, at least three pieces of specimens were cut and measured, and the average density was calculated. The areal density of the fabric was obtained from the supplier's technical data sheet rather than by measuring; this may have introduced some error in the calculations. For Figure 3-7 and Figure 3-8, the results estimated from the digital image analysis technique and from Equation (2-1) were in good agreement, thus validating the digital image analysis technique for the estimation of void content.

Table 3-2 summarizes the void content and the fiber volume fraction of the specimens from each case. Figure 3-7 shows that the void content of Case *A* increased and then decreased from the inlet to the vent. The average void content obtained using the image analysis technique was 2.08%. For Case *B*, the distribution was much more uniform. The average void content was

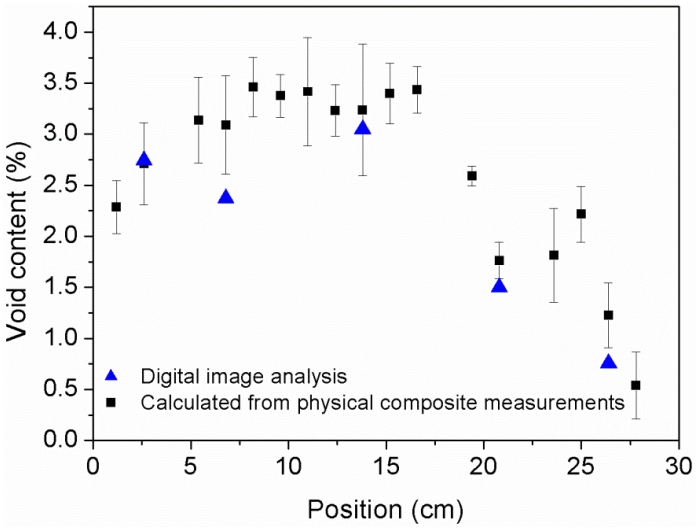

Figure 3-7 Void content distribution of a CFRP plate fabricated for Case A.

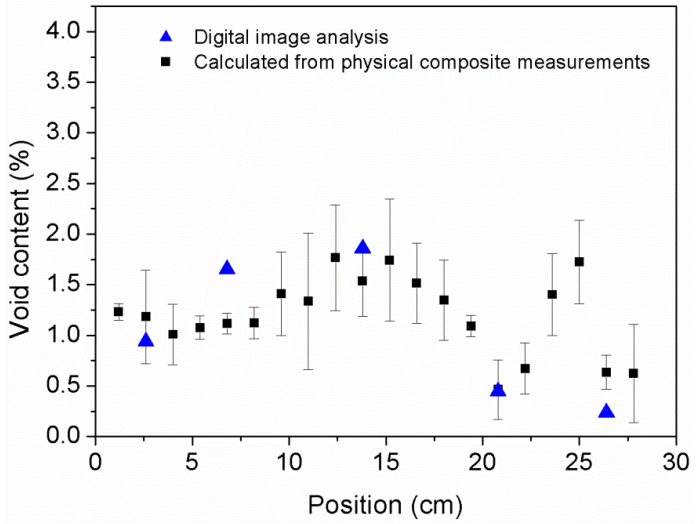

Figure 3-8 Void content distribution of a CFRP plate fabricated for Case B.

Table 3-2 Void content and fiber volume fraction of the specimens from each case.

Case	Void content		Fiber volume fraction	
	Average value	Difference to Case *C*	Average value	Difference to Case *C*
A	2.08%	1.26%	54.2%	-4.4%
B	1.03%	0.21%	56.2%	-2.4%
C	0.82%		58.6%	
D	0.07%	-0.75%	57.8%	-0.8%

1.03%. The lowest void content was also found in the vicinity of the vent. Figure 3-9 shows two micrograph segments of polished surfaces for Case *A*. Figure 3-9(a) was imaged 7 cm from the inlet side of the CFRP plate, and contains many large voids in resin-rich areas and some small voids inside the fiber tows. Figure 3-9(b) shows the polished surface 26 cm from the inlet side of the CFRP plate. The number of voids is much smaller. Another evident difference is that almost no small voids can be found inside the fiber tows in this picture, only some large voids between tows. Figure 3-10 shows micrographs taken 7 and 26 cm from the inlet side of the CFRP plate for Case *B*. Similar to the findings for Case *A*, large voids were present in the resin-rich areas at both positions; however, small voids in the fiber tows were only found at the 7 cm location.

Based on the void content results for Figure 3-7, the manufactured CFRP plate of Case *A* was divided into two parts: 0–23 cm and 23–30 cm. The first part had a very high void content while the segment from 23–30 cm had a much lower value. This substantial difference was likely caused by the distribution medium, which extended 23.5 cm from the inlet. The resin flowed horizontally in the section of the stack between the end of the distribution medium and the end of the stack. Air was entrapped by the resin primarily because of mismatched flow speeds within and between the fiber tows [10, 13, 14, 28]. However, in the portion covered by the distribution medium, the resin saturated the stack vertically. The complex flow pattern made it easier to entrap more air, and thereby led to a much higher void content. Another possible factor contributing to such a void content distribution was the evolution of the fluid pressure

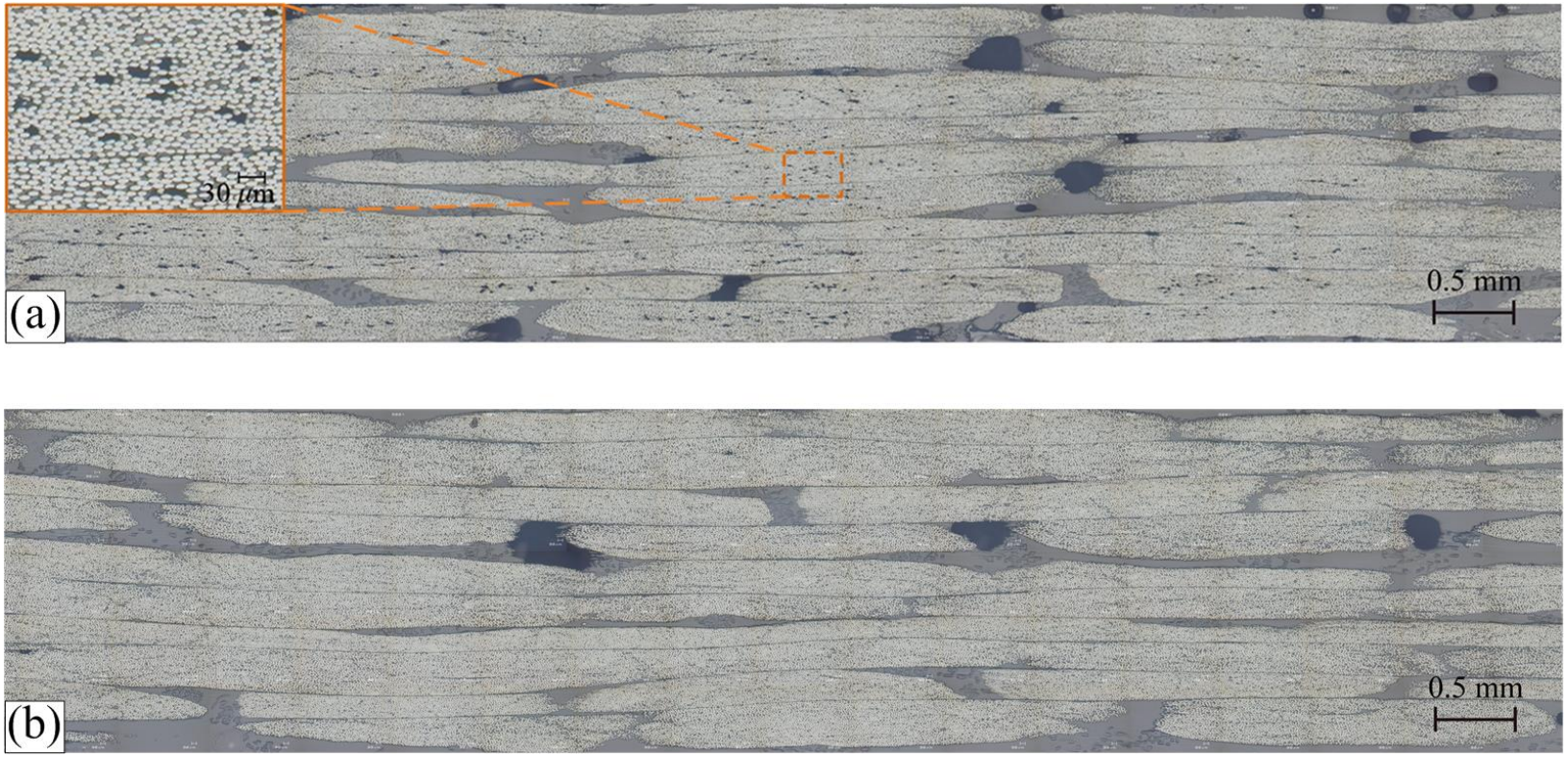

Figure 3-9 Micrographs of samples at the (a) 7 and (b) 26 cm locations for Case *A*.

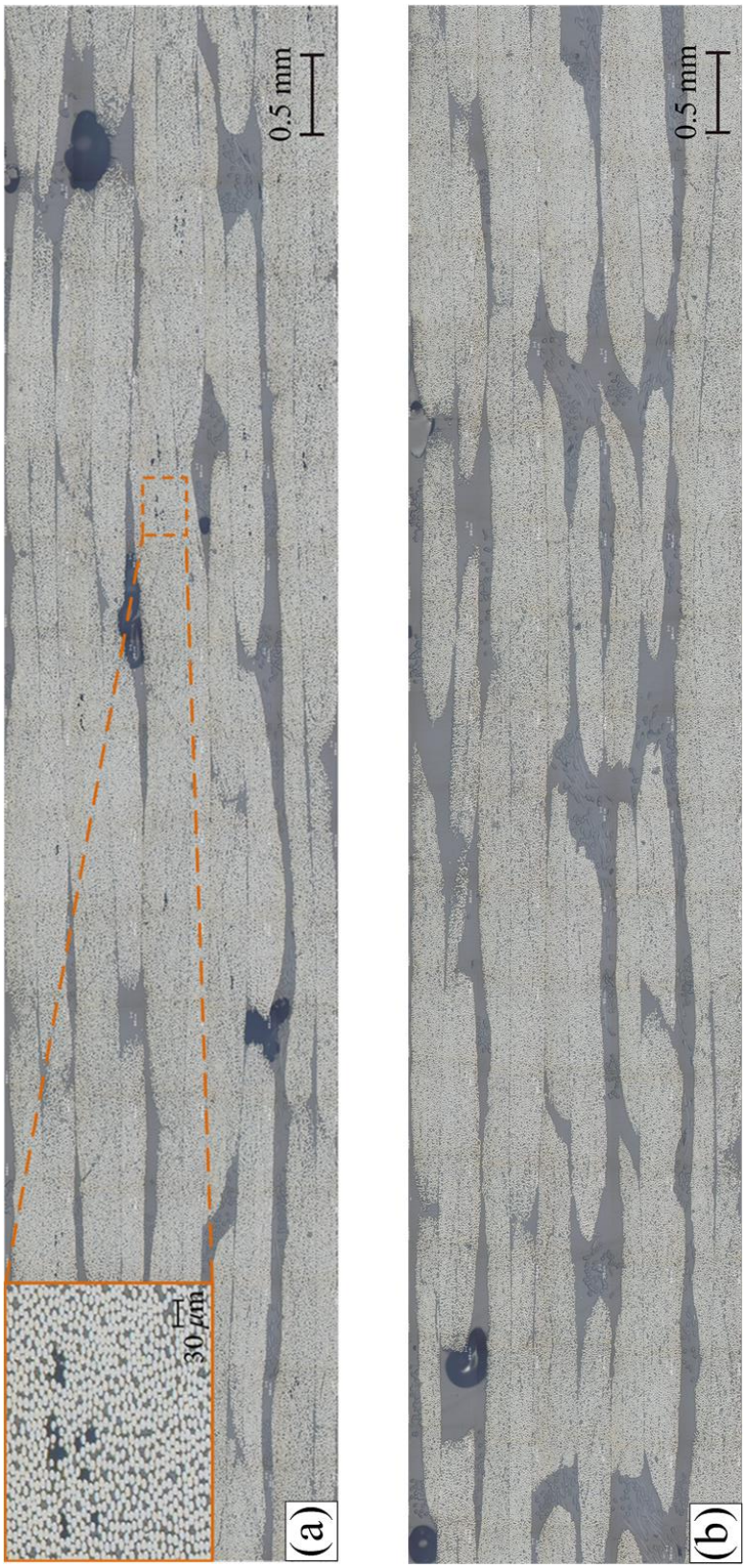

Figure 3-10 Micrographs of samples at the (a) 7 and (b) 26 cm locations for Case B.

distribution. According to Govignon [29], after the resin saturates the entire stack, the fluid pressure shows a decreasing distribution along the resin flow direction. After the inlet is closed, the fluid pressure of the entire part, especially the part near the inlet, begins to decrease. The reduced fluid pressure in the part distant from the vent can cause the generated voids to expand. After closing the vent, the fluid pressure near the vent increases slightly, leading to a slight shrinkage of the voids. Figure 3-9(a) shows voids inside fiber tows and in the resin-rich areas, confirming a complex flow beneath the distribution medium. In Figure 3-9(b), there are no small voids inside fiber tows. There are two possible reasons for this difference. First, resin flows faster inside tows than between tows, and consequently the air is only entrapped between tows. Second, the increased fluid pressure after the vent is closed causes small voids inside tows to shrink and then disappear. The void analyses of Cases *A* and *B* indicate that the effect of entrapped air is more important on void formation, particularly for a stack covered by a distribution medium.

Figure 3-11 shows the void content distributions for Cases *C* and *D*. For Case *C*, the average void content and fiber volume fraction were 0.82% and 58.6%, respectively. For Case *D*, the values were 0.07% and 57.8%, respectively. The micrograph for Case *C* in Figure 3-12 was imaged at the 9 cm location. Voids are evident both inside and between tows. The micrograph in Figure 3-13 was imaged at the 11 cm location for Case *D*. Only small voids inside tows are present.

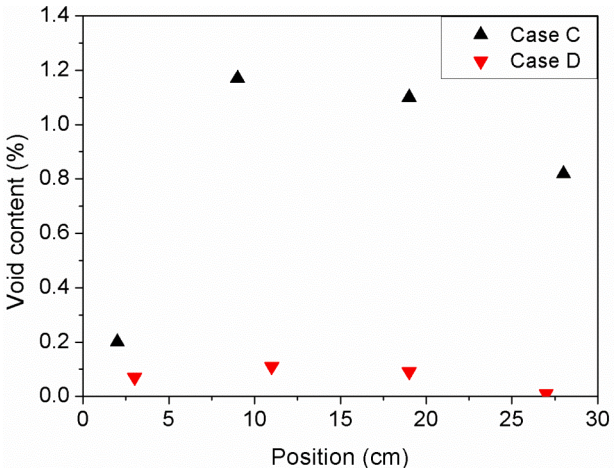

Figure 3-11 Void content distributions of CFRP plates fabricated for Cases C and D.

The void content for Case *C* was only slightly lower than that for Case *B*. The sources of voids in these two cases were dissolved air and evaporated resin. As discussed in Section 3.2, the resin had a constant evaporation rate at a fixed pressure. Consequently, the only difference in the infusion process between the two cases was the amount of dissolved air. Similar void contents indicate that the effect of degassing at pressures of 0-8.3 kPa was small. Although the degassing process is important to exhaust the dissolved air and thereby reduce the void content, the actual pressure requirement is not critical.

The CFRP plate fabricated in Case *D* had the lowest void content among all the tests. This demonstrated that increasing the pressure at the vent when the resin finished saturating the stack successfully reduced the void content. At the beginning of infusion, full vacuum ensured that there was almost no air remaining in the vacuum package; void formation due to entrapped air was avoided. After the resin arrived at the vent, increasing the pressure restrained evaporation of the resin. In this way, the two primary causes of voids were minimized and a composite with a

very low void content was obtained. Large voids in the resin-rich areas are notable in Figure 3-12 (Case *C*), but are absent in Figure 3-13 (Case *D*). This indicates that such large voids were mainly generated in the post-filling process (after closing the inlet) and are thus attributed to the evaporation of resin. Therefore, keeping the vent drawing vacuum during the whole VARTM process is not recommended.

Increasing the pressure slightly to obtain a low void content may negatively affect the fiber volume fraction of the product. High pressure under the vacuum bag will lead to big thickness of stacking. However, the effect of such small increase of the pressure is limited. On the other hand, increasing the pressure at the vent reduces the fluid pressure gradient, making it difficult to extrude the extra resin out from the stack. However, this is offset by the high pressure at the vent, which releases the stack and increases its permeability. Consequently, the fiber volume fraction was only reduced by 0.8%. Govignon [29] reported a similar result.

3.2.3 Summary

The void content of composites manufactured by VARTM was experimentally studied. Two main sources of voids were experimentally identified: non-uniform resin flow and continuous evaporation of resin under low pressure. A simple yet effective modification to the operation was proposed to reduce the effects of these two factors, i.e., setting the full vacuum of the equipment at the vent from the beginning of infusion and switching the pressure to a slightly higher value after the resin finished saturating the entire reinforcement. Void content measurements validated the approach.

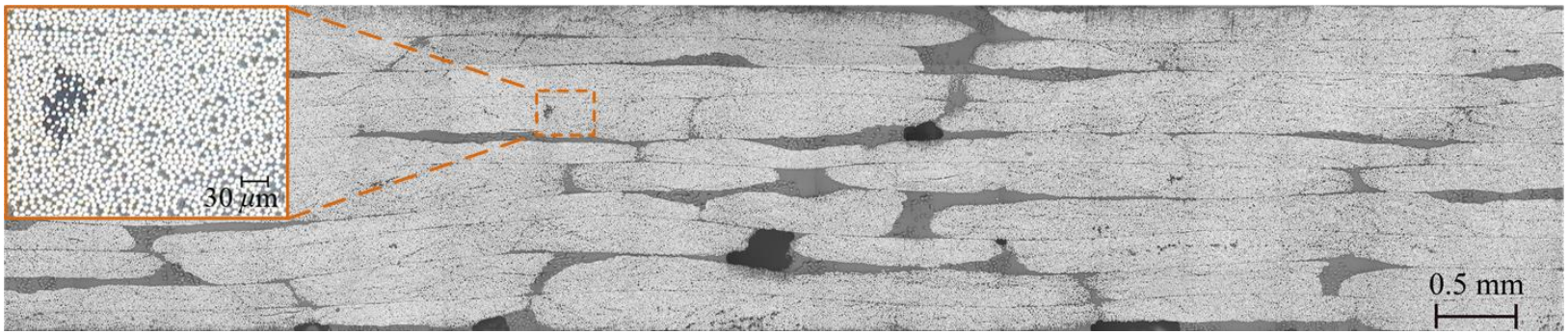

Figure 3-12 Micrograph of a sample at the 9 cm location for Case C.

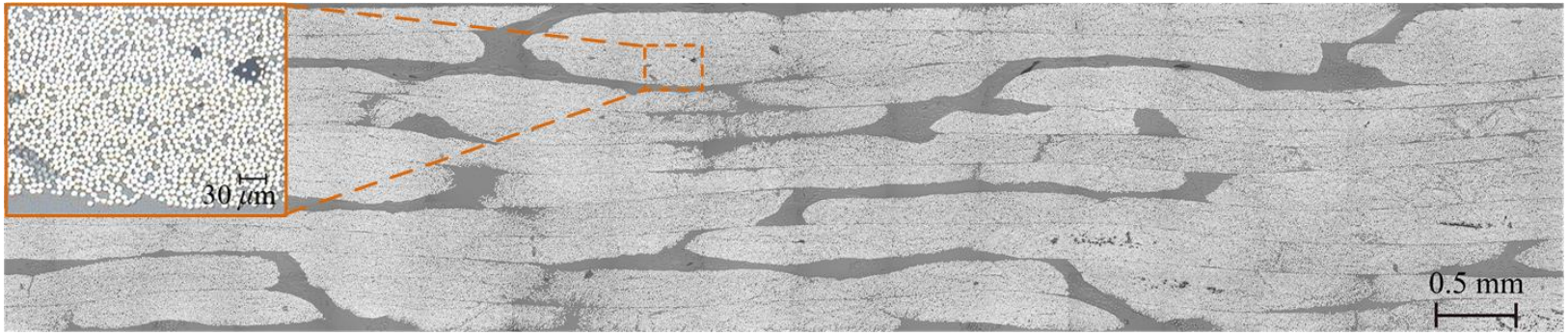

Figure 3-13 Micrograph of a sample at the 11 cm location for Case D.

3.3 Increase of fiber volume fraction

3.3.1 Experimental design

An additional cover mold is proposed to be used as shown in Figure 3-14 to improve the VARTM process to get a high fiber volume fraction. In order to study the effects of the cover mold, two groups of experiments were designed. Group 1 cases were designed to study the details of the resin flow with and without a cover mold in place. Group 2 cases were designed to assess the effect of a cover mold on normal VARTM processes. Table 3-3 and Table 3-4 provide details of the two groups. The thickness evolution of the package during the infusion step was monitored in all cases by the system introduced in Chapter 2 (Figure 3-14). Data at five points (*A* to *E*, Figure 3-14(b)), positioned on the centerline from the inlet to the vent, were analyzed to obtain the infusion details.

In the Group 1 cases, the reinforcement was only 130 mm wide by 170 mm long, allowing the resin to saturate the entire reinforcement layer without needing a distribution medium. Thus, a distribution medium was not used in Cases 1-1 and 1-2. Here, the displacement of the vacuum bag along the axis of the thickness evolution indicated the change in the thickness of the reinforcement layer. The difference between Cases 1-1 and 1-2 is the usage of a cover mold. Case 1-1 was similar to the conventional VARTM practice that does not use a cover mold. In Case 1-2, a 5-mm-thick poly(methylmethacrylate) (PMMA) plate with the same dimensions as the reinforcement layer was inserted between the vacuum bag and the peel ply layer (Figure 3-14(a)). The time when infusion began (opening the inlet) was set as the start time for

subsequent analyses. In these two cases, the inlet was closed after ca. 70 min and the vent was closed after ca. 135 min. Point *A* was ca. 5 mm from the edge of the reinforcement. The distance between neighboring points was ca. 40 mm (Figure 3-14(b)).

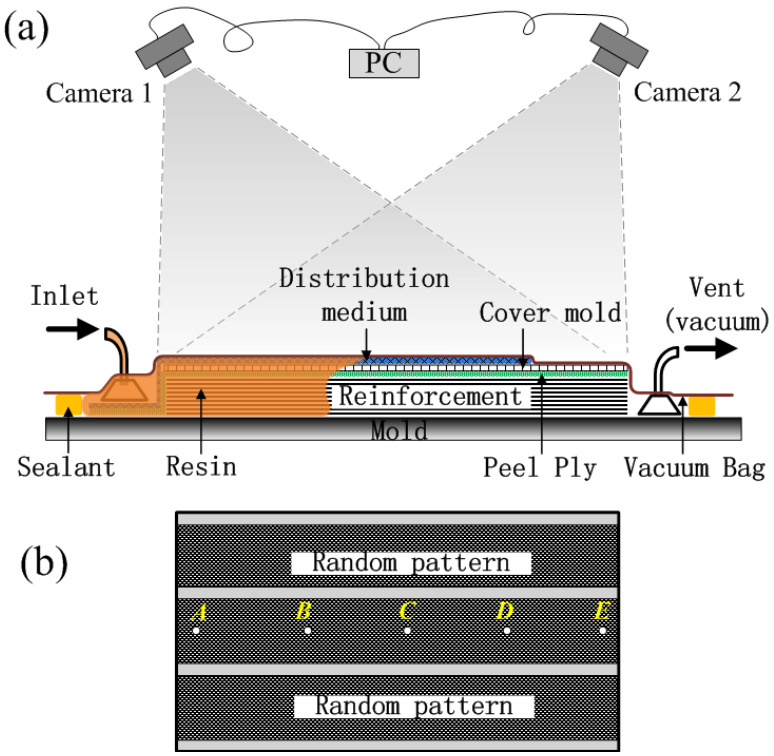

Figure 3-14 (a) Schematic diagram showing the VARTM process with the 3D–DIC test system. (b) Top view of the vacuum package.

Table 3-3 Experimental details for the Group 1 manufacturing processes.

Case	Size (mm)	Distribution medium	Cover mold	Time inlet was closed (min)*	Time vent was closed (min)*
1-1	130 × 170	no	none	70	135
1-2	130 × 170	no	5-mm-thick PMMA plate	70	135

*The time for closing the inlet and the vent are referenced to the initial opening of the inlet.

Table 3-4 Experimental details for the Group 2 manufacturing processes.

Case	Size (mm)	Distribution medium	Cover mold	Time inlet was closed (min)*	Time vent was closed (min)*
2-1	200 × 300	yes	none	19	150
2-2	200 × 300	yes	0.5-mm-thick perforated aluminum plate	19	150
2-3	200 × 300	yes	0.5-mm-thick perforated steel plate	19	150
2-4	200 × 300	yes	0.8-mm-thick perforated steel plate	19	150

*The time for closing the inlet and the vent are referenced to the initial opening of the inlet.

In the Group 2 cases (Table 3-4), the reinforcements were much larger, i.e., 200 mm wide by 300 mm long. A distribution medium was used, as is the case in conventional VARTM. The reinforcement layer was partially covered by the distribution medium (Figure 3-14(a)). The distance between the end of the distribution material and the end of the reinforcement was 65 mm. Case 2-1 did not use a cover mold and can be considered as a normal VARTM process. In Cases 2-2 to 2-4, cover molds with different flexural rigidities were used, i.e., 0.5-mm-thick aluminum plate, 0.5-mm-thick steel plate, and 0.8-mm-thick steel plate. These were inserted between the peel ply and the distribution medium, and were used to study the effects of different rigid cover molds on VARTM processes. All of the plates had the same size as the reinforcement. To allow the resin to flow from the distribution medium to the reinforcement, the plates were perforated identically. The perforated pattern is the same as introduced in Section

3.2.2 (Figure 3-6). In these four cases, the inlet was closed after 19 min and the vent was closed after 150 min. Point *A* was ca. 20 mm from the edge of the reinforcement. The distance between neighboring points was ca. 65 mm.

All Group 1 and 2 cases used an inlet and vent that were located on either side of the reinforcement (Figure 3-14(a)). These, made from a rubber connector and a segment of spiral tube, provided a linear inlet and vent configurations and uniform resin flow. The reinforcement was composed of five layers of the [30° / –30°] stitched carbon fiber fabric. The matrix was the epoxy resin XNR/H 6815 that can be cured at room temperature. All the VARTM processes were finished at 27 ^{o}C. The flexural rigidities of the four cover molds are given in Figure 3-15. The data for the 5-mm-thick PMMA plate were calculated through physical parameters. The other results are from three-point bending tests at a loading speed of 1 mm/min.

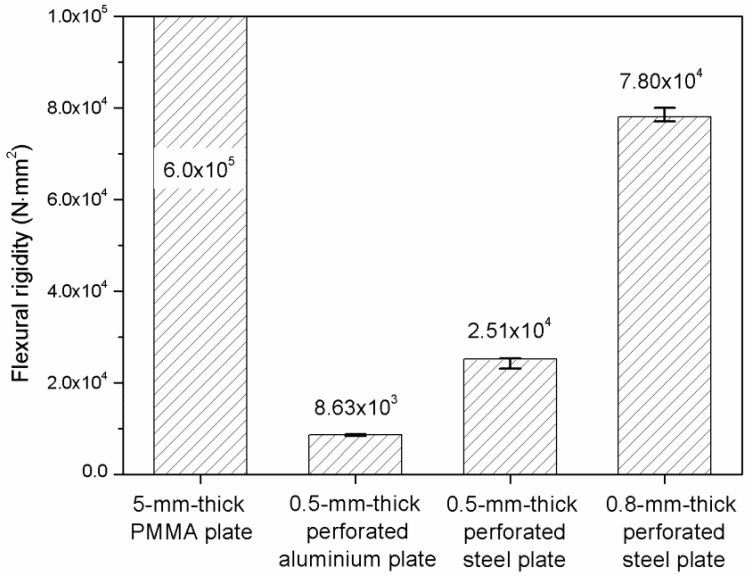

Figure 3-15 Flexural rigidity of 20-mm-wide plates made from the cover mold materials.

The fiber volume fraction of the carbon-fiber-reinforced polymer (CFRP) plates manufactured from the Group 2 cases was measured. The fiber volume fraction f_{fiber} was calculated using the equation

$$f_{fiber} = (\rho_{CFRP} + \rho_{resin} \cdot f_{void} - \rho_{resin}) / (\rho_{fiber} - \rho_{resin}), \quad (3\text{-}1)$$

where ρ_{fiber}, ρ_{resin}, and ρ_{CFRP} are the densities of the carbon fiber, the resin, and the CFRP specimen, respectively. They were tested in accordance with the ASTM D792 standard. The void content of the CFRP specimen, f_{void}, was calculated using a digital image analysis technique [30].

3.3.2 Effects of cover mold

Figure 3-16 shows the changes in thickness that occurred at the five points on the vacuum package for Case 1-1. After opening the inlet, point *1-1-A* quickly expanded because of the mass of infused resin. However, obvious signs of shrinkage were evident at the other points; they first shrank, and then expanded. Simacek et al. [18] and Yenilmez and Sozer [31, 32] observed a similar phenomenon. The entire part was fully saturated at ca. 54 min. After closing the inlet at ca. 70 min, the entire part began to shrink because no resin was being infused and excess resin continued to be extruded until the vent was closed. No significant further changes were observed after closing the vent at ca. 130 min because the viscosity of the resin had become too high to allow the resin to flow.

The shrinkage stage can be divided into two stages. Consider the thickness change at point *1-1-E* in Figure 3-16. Only a slight change is apparent in the first stage from the beginning of

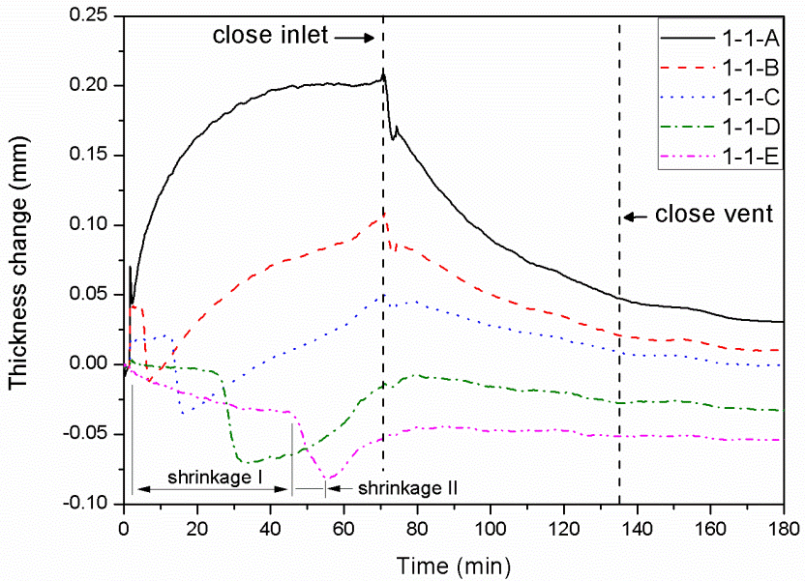

Figure 3-16 Thickness changes in the package for Case 1-1.

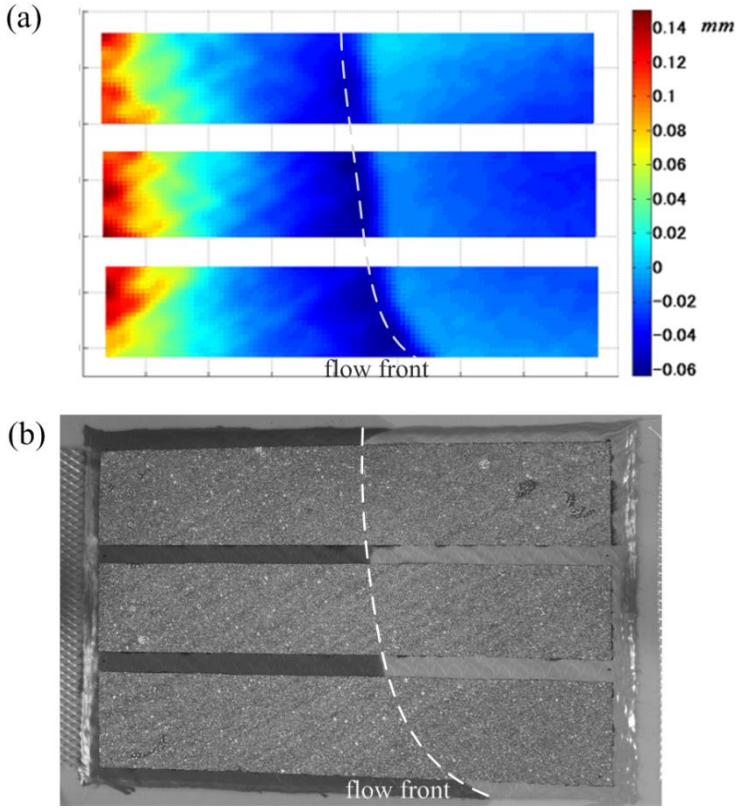

Figure 3-17 (a) Full-field thickness change distribution of the package for Case 1-1 at 17 min calculated using the DIC technique. A corresponding photo taken by a camera is shown in (b).

the infusion to the end when the resin arrives. This is attributed to a dry vacuum [31, 32]. The second stage is much more obvious, and starts at the arrival of the resin. We hypothesize that this stage stems from a reduction in friction between fibers upon their first contact with the resin, facilitating compaction of the stack. Additionally, the surface tension of the resin increases the compacting pressure. These two factors result in a thickness decrease. The friction between the fibers no longer decreases once the amount of resin exceeds that required for full saturation. Then, the stack expands as the increasing amount of resin shares more of the compacting pressure in the stack.

Figure 3-17(a) shows the full-field thickness change distribution of the entire package at 17 min, and Figure 3-17(b) shows a corresponding photo of the package taken by one of the cameras. The resin was infused from the left side. The layers in the stack changed from gray to black as the saturation with resin progressed. The dashed line in Figure 3-17(b) shows the flow front of the resin. Based on the previous analysis of the thickness evolution, the deep blue area approximately defined by the dashed line in Figure 3-17(a) is considered the flow front. The good agreement of Figure 3-17(a) and (b) validates the 3D–DIC system again.

Figure 3-18 shows the thickness change at five points on the vacuum package for Case 1-2. The use of a rigid cover mold significantly affected the thickness evolution. As for point *1-1-E* in Figure 3-16, the thickness at point *1-2-E* diminished through two stages and then expanded. Points from *1-2-A* to *1-2-D* presented totally different thickness change evolutions compared with the behavior of Case 1-1. These parts first expanded, then shrank, and expanded again,

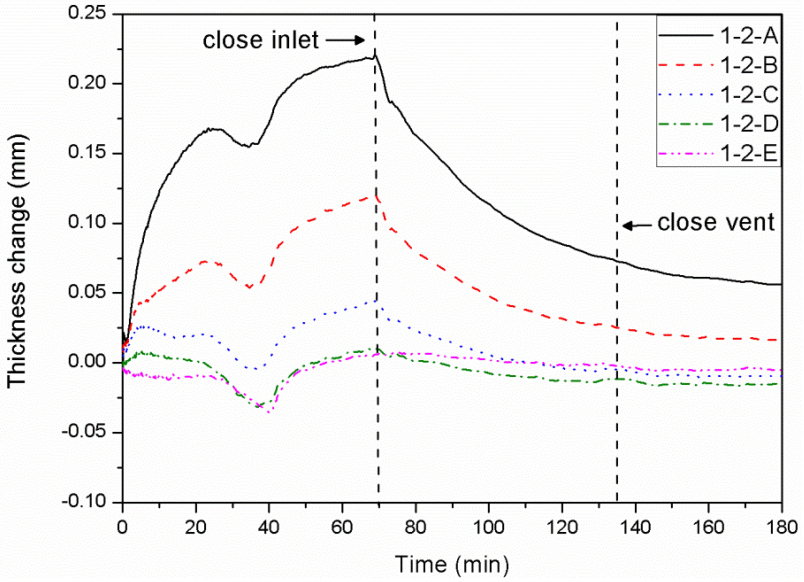

Figure 3-18 Thickness changes in the package for Case 1-2.

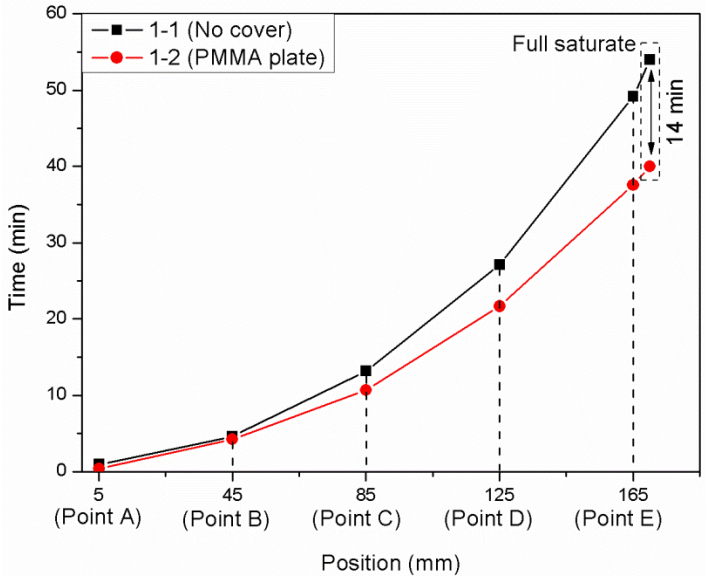

Figure 3-19 Arrival time of the resin at points A to E for the Group 1 cases.

synchronously. The time required for the resin to fill the entire part was ca. 40 min. The first expansion at point *1-2-A* was caused by the mass of infused resin. The expansion at points *1-2-B* to *1-2-D* was caused by a combined effect of the expansion of point *1-2-A* and the high flexural rigidity of the cover mold. We called this the ***"expansion effect"***. Point *1-2-E* did not reflect this

effect because it was near the end of the cover mold, which behaved as a supporting point. When the resin arrived at the supporting point (i.e., the end of the cover mold), this part began to shrink, causing the whole part to shrink. Then, as more resin was infused, the entire stack expanded together.

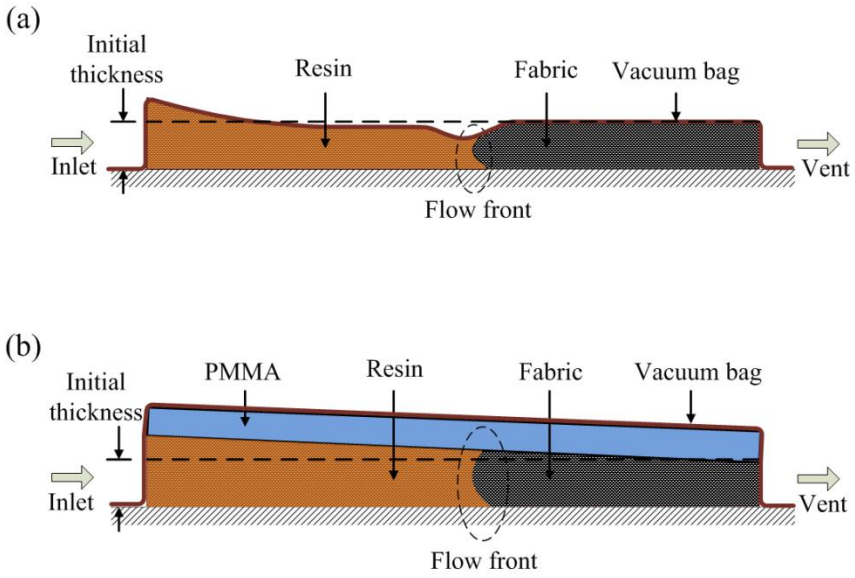

Figure 3-20 Illustrations of the infusion process (a) without and (b) with a cover mold.

The flow speed of the resin inside the reinforcement is evident from Figure 3-19, in which the arrival times of the resin at points *A* to *E* are noted. With a rigid cover mold in place, the time required for the resin to saturate the entire reinforcement was cut by 14 min. This behavior is attributed to the expansion effect caused by the rigid cover mold. A model for the filling stages (from the opening to the closing of the inlet) of Cases 1-1 and 1-2 is shown in Figure 3-20. During the filling stage of Case 1-1 (Figure 3-20(a)), the saturated part of the stack, except for the area nearest the inlet, remained in a shrunken state most of the time. Such shrinkage,

particularly that caused by the flow front, compacted the stack more tightly, making resin flow difficult. In contrast, in Case 1-2, the entire part was forced to expand because of expansion near the inlet and the rigid cover mold. This expansion state promoted the flow of resin. Consequently, the resin saturated the whole part more quickly in Case 1-2. In a production setting, the shorter filling time would permit the inlet to be closed earlier, and a longer time could be used to extrude the excess resin remaining in the package. The end result would be a higher fiber volume fraction in the finished part.

Figure 3-21 to Figure 3-24 show the thickness change of the package in the Group 2 cases. The fabric under points *A* to *D*, but not under point *E*, was covered by the distribution medium. Consequently, the thickness change at point *E* was completely different than that at the other points. After opening the inlet, the entire stack began to expand until the inlet was closed. The maximum thickness attained by the stack decreased with increasing flexural rigidity of the cover mold. In Case 2-1, the whole package gradually shrank after closing the inlet, and then maintained a constant thickness. In the other cases, the thickness decreased much more quickly to a stable, lower value.

The shrinkage speed of the various cases was estimated by fitting the slope of the thickness change of point *C* (from 19 min to 29 min) to a linear equation. The results and the time required for the resin to saturate the entire reinforcement are listed in Table 3-5. As the flexural rigidity of the cover mold increased, the resin finished saturating faster and the stack shrank more quickly once the inlet was closed. Figure 3-25 shows the fiber volume fractions and void

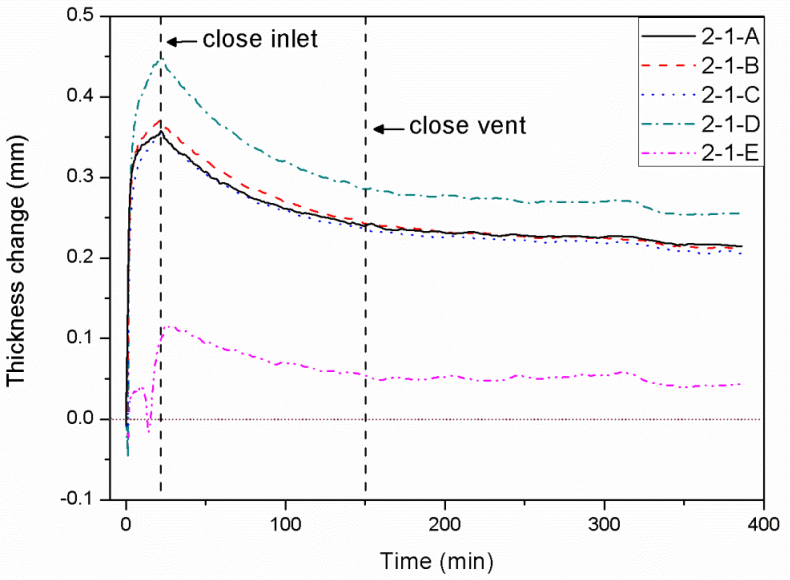

Figure 3-21 Thickness changes in the package for Case 2-1.

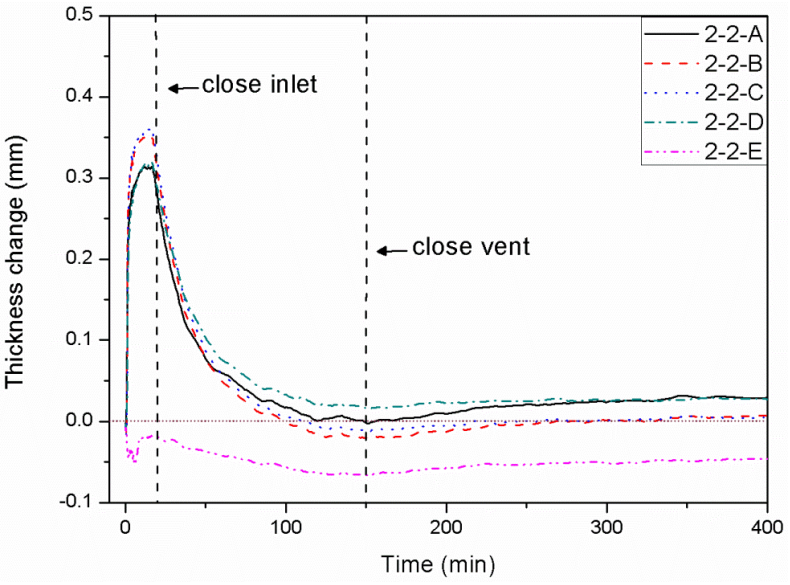

Figure 3-22 Thickness changes in the package for Case 2-2.

contents of the plates manufactured from Cases 2-1 to 2-4. Usage of a cover mold increased the fiber volume fraction of the final product.

Because of the high permeability of the distribution medium, the resin arrived at the end of the distribution medium (ca. 65 mm from the end of the reinforcement) almost immediately

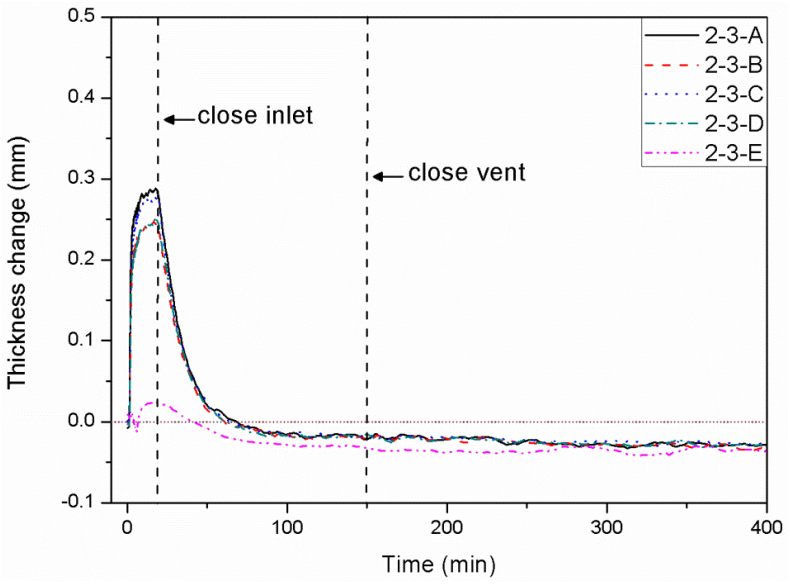

Figure 3-23 Thickness changes in the package for Case 2-3.

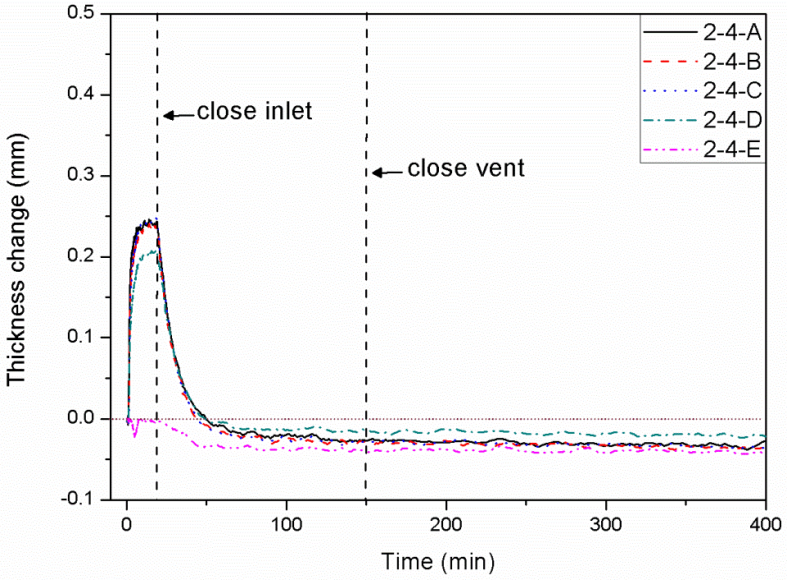

Figure 3-24 Thickness changes in the package for Case 2-4.

after the inlet was opened. Consequently, almost all of the infusion time was used to saturate the part not covered by the distribution medium. In Case 2-1 in which no cover mold was used, the thickness change of each part was independent. As noted in the previous section, when the resin arrived at the part not covered by the distribution medium, the part first shrank. Such shrinkage

Table 3-5 Shrinkage speed at point *C* and the time for full infusion

Case	Required time for complete infusion (min)	Linear fitting results	
		Shrinkage speed (mm/min)	Adjusted r^2
2-1	15	0.0023	0.985
2-2	8	0.0123	0.997
2-3	5	0.0146	0.994
2-4	4	0.0160	0.988

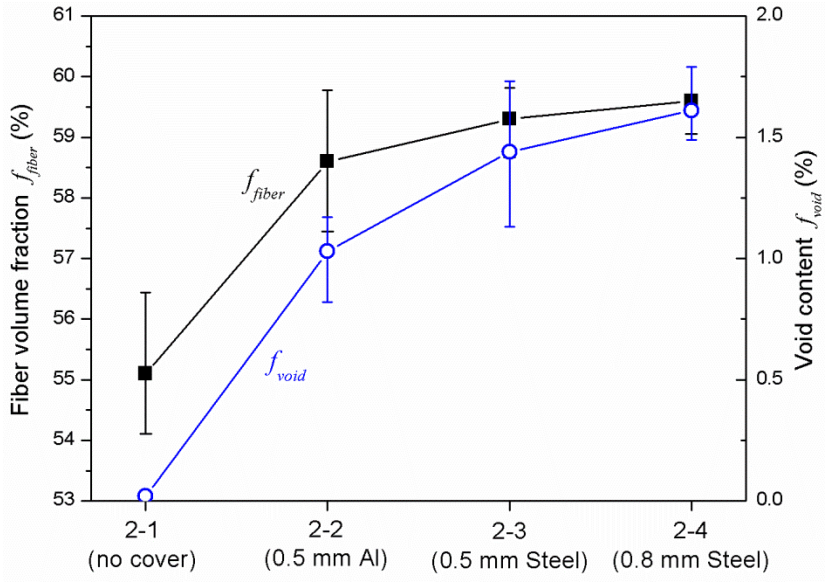

Figure 3-25 Fiber volume fraction and void content of manufactured CFRP plates for the Group 2 cases.

blocked the flow of the resin; consequently, more time was required for the resin to saturate the entire reinforcement. On the other hand, the unrestrained expansion caused a large amount of resin to collect in the region under the distribution medium. In the other cases in which a cover mold was used, the portion of the reinforcement not covered by the distribution medium was forced to expand through a combined effect of the expansion of the part under the distribution medium and the rigidity of the cover mold, promoting the flow of the resin. Consequently, a

shorter time was required for complete infusion. A cover mold restricted expansion of the part under the distribution medium, and the amount of resin that could be stored in the stack was limited. This explains why the maximum thickness of the stack was lower when a rigid cover mold was used. After closing the inlet, and with a more rigid cover mold, the stack shrank faster, which caused the excess resin to be extruded through the vent more quickly.

Less resin stored in the stack and higher extrusion speed of the excess resin caused by the cover mold enabled a higher fiber volume fraction in the final CFRP product. Figure 3-25 shows such a phenomenon, however, the improvement was not evident. We believe that the fiber volume fraction of the final CFRP product had already reached its maximum value with these raw materials, because the void content evidently increased as the cover mold became stiffer (Figure 3-25). As introduced in Section 3.2 and Ref. [30], the main source of voids in the VARTM process is evaporation of the resin. As more and more resin is extruded, the liquid pressure of the resin decreases, leading to evaporation and void formation after the resin cures. The evaporation prevents shrinkage of the stack, making it difficult to reach a higher fiber volume fraction.

3.3.3 Summary

VARTM processes with and without a cover mold were studied using a 3D–DIC thickness change monitoring system. This monitoring system was validated for monitoring full-field thickness changes during the VARTM process. The effects of a cover mold are three-fold. First, in the filling stage, a rigid cover mold can prevent shrinkage of the part at the resin flow front,

and even force the unsaturated part to slightly expand, making the resin easier to flow, and thereby shortening the time required for complete infusion. Second, the cover mold can prevent large expansion of the fully saturated part, which restricts the amount of excess resin that can be stored in the fully saturated part. Finally, in the post-filling stage, the cover mold can accelerate extrusion of the excess resin. Because of these effects, the modified VARTM process can provide a final product with a higher fiber volume fraction.

Bibliography

[1] Takeda F, Nishiyama S, Hayashi K, Komori Y, Suga Y, Asahara N. Research in the application of the VaRTM technique to the fabrication of primary aircraft composite structures. Tech Rev Mitsubishi Heavy Ind. 2005;42(5):1-6.

[2] Zhu HY, Wu BC, Li DH, Zhang DX, Chen YY. Influence of Voids on the Tensile Performance of Carbon/epoxy Fabric Laminates. J Mater Sci Technol. 2011;27(1):69-73.

[3] Huang H, Talreja R. Effects of void geometry on elastic properties of unidirectional fiber reinforced composites. Composites Science and Technology. 2005;65(13):1964-1981.

[4] Scott AE, Sinclair I, Spearing SM, Mavrogordato MN, Hepples W. Influence of voids on damage mechanisms in carbon/epoxy composites determined via high resolution computed tomography. Composites Science and Technology. 2014;90(0):147-153.

[5] Hagstrand PO, Bonjour F, Månson JAE. The influence of void content on the structural flexural performance of unidirectional glass fibre reinforced polypropylene composites. Composites Part A: Applied Science and Manufacturing. 2005;36(5):705-714.

[6] Seon G, Makeev A, Nikishkov Y, Lee E. Effects of defects on interlaminar tensile fatigue behavior of carbon/epoxy composites. Composites Science and Technology. 2013;89(0):194-201.

[7] Lundstrom TS, Gebart BR. INFLUENCE FROM PROCESS PARAMETERS ON VOID FORMATION IN RESIN TRANSFER MOLDING. Polymer Composites. 1994;15(1):25-33.

[8] Hamidi YK, Aktas L, Altan MC. Three-dimensional features of void morphology in resin

transfer molded composites. Composites Science and Technology. 2005;65(7–8):1306-1320.

[9] Kuentzer N, Simacek P, Advani SG, Walsh S. Correlation of void distribution to VARTM manufacturing techniques. Composites Part A: Applied Science and Manufacturing. 2007;38(3):802-813.

[10] Kedari VR, Farah BI, Hsiao K-T. Effects of vacuum pressure, inlet pressure, and mold temperature on the void content, volume fraction of polyester/e-glass fiber composites manufactured with VARTM process. Journal of Composite Materials. 2011;45(26):2727-2742.

[11] Hernández S, Sket F, González C, Llorca J. Optimization of curing cycle in carbon fiber-reinforced laminates: Void distribution and mechanical properties. Composites Science and Technology. 2013;85(0):73-82.

[12] Parnas RS, Walsh SM. Vacuum-assisted resin transfer molding model. Polymer Composites. 2005;26(4):477-485.

[13] Park CH, Lebel A, Saouab A, Bréard J, Lee WI. Modeling and simulation of voids and saturation in liquid composite molding processes. Composites Part A: Applied Science and Manufacturing. 2011;42(6):658-668.

[14] DeValve C, Pitchumani R. Simulation of void formation in liquid composite molding processes. Composites Part A: Applied Science and Manufacturing. 2013;51(0):22-32.

[15] Mathuw R, Advani SG, Heider D, Hoffmann C, Gillespie JW, Fink BK. Flow front measurements and model validation in the vacuum assisted resin transfer molding process. Polymer Composites. 2001;22(4):477-490.

[16] Song YS, Youn JR. Modeling of resin infusion in vacuum assisted resin transfer molding. Polymer Composites. 2008;29(4):390-395.

[17] Matsuzaki R, Kobayashi S, Todoroki A, Mizutani Y. Full-field monitoring of resin flow using an area-sensor array in a VaRTM process. Compos Pt A-Appl Sci Manuf. 2011;42(5):550-559.

[18] Simacek P, Eksik Ö, Heider D, Gillespie Jr JW, Advani S. Experimental validation of post-filling flow in vacuum assisted resin transfer molding processes. Composites Part A: Applied Science and Manufacturing. 2012;43(3):370-380.

[19] Govignon Q, Bickerton S, Morris J, Kelly PA. Full field monitoring of the resin flow and laminate properties during the resin infusion process. Composites Part A: Applied Science and Manufacturing. 2008;39(9):1412-1426.

[20] Johnson RJ, Pitchumani R. Flow control using localized induction heating in a VARTM process. Composites Science and Technology. 2007;67(3-4):669-684.

[21] Johnson RJ, Pitchumani R. Enhancement of flow in VARTM using localized induction heating. Composites Science and Technology. 2003;63(15):2201-2215.

[22] Govignon Q, Bickerton S, Kelly PA. Simulation of the reinforcement compaction and resin flow during the complete resin infusion process. Composites Part A: Applied Science and Manufacturing. 2010;41(1):45-57.

[23] Nalla AR, Fuqua M, Glancey J, Lelievre B. A multi-segment injection line and real-time adaptive, model-based controller for vacuum assisted resin transfer molding. Composites Part

A: Applied Science and Manufacturing. 2007;38(3):1058-1069.

[24] Alms JB, Glancey JL, Advani SG. Mechanical properties of composite structures fabricated with the vacuum induced preform relaxation process. Composite Structures. 2010;92(12):2811-2816.

[25] Tuladhar TR, Mackley MR. Experimental observations and modelling relating to foaming and bubble growth from pentane loaded polystyrene melts. Chemical Engineering Science. 2004;59(24):5997-6014.

[26] Fu BR, Pan C. Bubble growth with chemical reactions in microchannels. International Journal of Heat and Mass Transfer. 2009;52(3–4):767-776.

[27] Sul IH, Youn JR, Song YS. Bubble development in a polymeric resin under vacuum. Polym Eng Sci. 2012;52(8):1733-1739.

[28] Kang MK, Lee WI, Hahn HT. Formation of microvoids during resin-transfer molding process. Composites Science and Technology. 2000;60(12–13):2427-2434.

[29] Govignon Q, Bickerton S, Kelly P. Experimental investigation into the post-filling stage of the resin infusion process. Journal of Composite Materials. 2013;47(12):1479-1492.

[30] Chen D, Arakawa K, Xu C. Reduction of Void Content of Vacuum-Assisted Resin Transfer Molded Composites by Infusion Pressure Control. Polymer Composites.

[31] Yenilmez B, Sozer EM. Compaction of e-glass fabric preforms in the Vacuum Infusion Process, A: Characterization experiments. Composites Part A: Applied Science and Manufacturing. 2009;40(4):499-510.

[32] Yenilmez B, Sozer EM. Compaction of e-glass fabric preforms in the vacuum infusion process: (a) use of characterization database in a model and (b) experiments. Journal of Composite Materials. 2013;47(16):1959-1975.

CHAPTER 4
Applications for VARTM processes

This chapter introduces two applications of VARTM processes. First, two novel joints made from partially un-molded CFRP plates are designed to increase the strength of joints between CFRP parts. In the partially un-molded plate, a portion of the fabric stack is molded with resin while the rest of the fabric stack remains dry. The plate is made using a manufacturing process developed from VARTM. A new double-lap joint sandwiches a normal CFRP plate between the dry fabric layers of a partially un-molded plate. The other laminated joint overlaps the dry fabric layers of two partially un-molded plates. Both joints are molded by resin transfer. Tensile testing indicates that the two novel joints are more than twice as strong as a classical double-lap joint, and half as strong as a normal, joint-free CFRP plate. Second, a wind-lens was manufactured using VARTM. A simple and low cost method for manufacturing a mold for VARTM is presented. Two-dimensional structures were used to construct a three-dimensional skeleton of a mold. Putty was then applied to the skeleton to obtain a smooth, hard, and strong surface. Finally, a high-elongation plastic film was tightly stretched and attached to the surface of the mold to ensure an airtight seal. The approach was validated by the successful fabrication of a carbon fiber-reinforced plastic part using the mold.

4.1 Introduction

As described in Chapter 1, the goal of establishing VARTM in this research was to allow the fabrication of a wind-lens power system. In this chapter, the fabrication process for a wind-lens is introduced. The designed wind-lens consisted of six one-sixth CFRP parts bolted together. However, bolting may not the best method for joining; more work is required to assess better joining methods.

Multiple experimental studies and simulations have investigated the failure of different types of joints, including composites to composites [1-8] and composites to other materials [9-13]. In adhesive bonding situations, initial cracking usually occurs around overlapping ends due to stress concentrations [1]. There are seven failure modes, such as separation of the interface between the adhesive and composite, de-lamination within the composite, and a mixture of the first two modes [14-17]. Micromechanical investigations have revealed different dominant failure modes under tensile and shear loads [2]. The strength of the interface between the adhesive and composite at a joint is a key factor in determining the failure mode and the strength of a structure. On the other hand, the thickness of the bondline is also an important factor affecting the strength of a joint. Strength increases with decreasing bondline thickness [4, 7, 16]. However, thick bondlines are typically unavoidable in engineering practice due to uneven surfaces and different thicknesses of the connected parts. A typical method for improving the strength of adhesive joints is increasing the overlap length [4, 5]. However, some studies suggest that there is an effective bond length for double-lap joints between CFRP plates

and steel plates [9-11]. Classical adhesive joints have some inherent disadvantages that restrict the potential strength of a joint; consequently, many modifications have been attempted to improve their properties.

An adhesive tongue-and-groove joint has been proposed for joining of thick, woven E-glass/vinyl-ester composite laminated plates to steel or other composite plates [18]. In this case, the adhesive bond is stronger than the tongues, so that failure is transferred from the adhesive to the adherents. Smart cure cycles with cooling and reheating for co-cure bonded steel/carbon epoxy composite hybrid structures have been developed to reduce the fabrication thermal residual stress between the steel and carbon epoxy composite material to improve the strength of the joint [19]. Surface modification of adherents with aramid fibers, thereby bridging fibers and adhesive, has also been proposed to increase the strength of adhesive joints [20-22]. Because the interface strength is usually the weakest part of a structure, most of the reported methods have aimed to improve the strength of the adhesive or the strength of adhesive–composite interfaces. However, if the adhesive or adhesive–composite interface can be altogether avoided, the strength might be further improved.

The wind-lens we planned to make is for a 1-kW wind-lens turbine having an outer diameter of 2 m. The main issue we face is how to make a mold for the VARTM process. Traditional processes include lathing, chopping, or punching the required materials. However, the resulting size of the structure is limited using these conventional approaches, and custom-designing a machine would be very expensive. Although this might be acceptable for large-scale

manufacturing, it is not suitable for research purposes in a laboratory. Some companies, such as Easy Composites Ltd., specialize in supplying mold-making materials so that molds can be made from readily available parts. However, sometimes the requisite parts simply do not exist.

In our search, a manufacturing process developed from VARTM was proposed to fabricate partially un-molded CFRP laminates in which most of the carbon-fiber fabric layers are molded with resin, but some parts remain dry. Two novel joints were designed using the partially un-molded laminates. First, a new double-lap joint, which sandwiches a CFRP plate between the dry fabric layers of a partially un-molded plate, was molded by a resin-infusion process, thereby resulting in a joint with only one adhesive–adherent surface instead of the more typical two such surfaces. In addition, a laminated joint was fabricated in which the un-molded part of the two partially un-molded plates overlapped. The laminated joint also used resin-transfer molding, thereby avoiding the formation of an interface. Tensile tests were performed to estimate the strength of the two joints. The fracture modes were identified using scanning electron microscopy images of fractured surfaces. For manufacturing the wind-lens, a simple and low-cost method for making a large and complex mold for the VARTM process is introduced. All of the materials required by this approach are readily available and can be bought from a handwork materials market. A mold was made for a one-sixth portion of a wind-lens for a 1-kW turbine. Using this mold, six CFRP parts were produced and combined to obtain the full-sized wind-lens.

4.2 Novel joints developed from VARTM processes

4.2.1 Manufacture of partially un-molded CFRP laminates

Partially un-molded CFRP laminates are laminates in which a portion of the structure is fiber reinforced while the rest remains in the dry fabric state, as shown in the partially un-molded unidirectional CFRP example depicted in Figure 4-1. In the figure, the CFRP portion is on the left, and the dry carbon fabric is on the right. This partially un-molded laminate was used as the basis for fabricating the novel joints introduced in the next subsection.

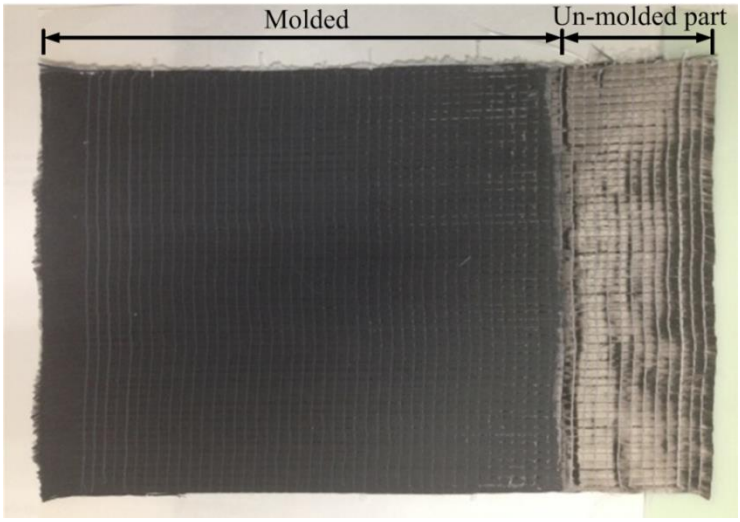

Figure 4-1 Manufactured partially un-molded laminate.

The partially un-molded laminate was made using a manufacturing process developed from VARTM. The entire process comprised three steps: fabricating a vacuum package, infusing the resin, and molding. The structure of the vacuum package used in the experiment is shown in Figure 4-2. A solid mold, covered with a piece of peel ply, was used. Four layers of the stitched unidirectional carbon-fiber fabric with dimensions of 30 cm in length and 20 cm in width were

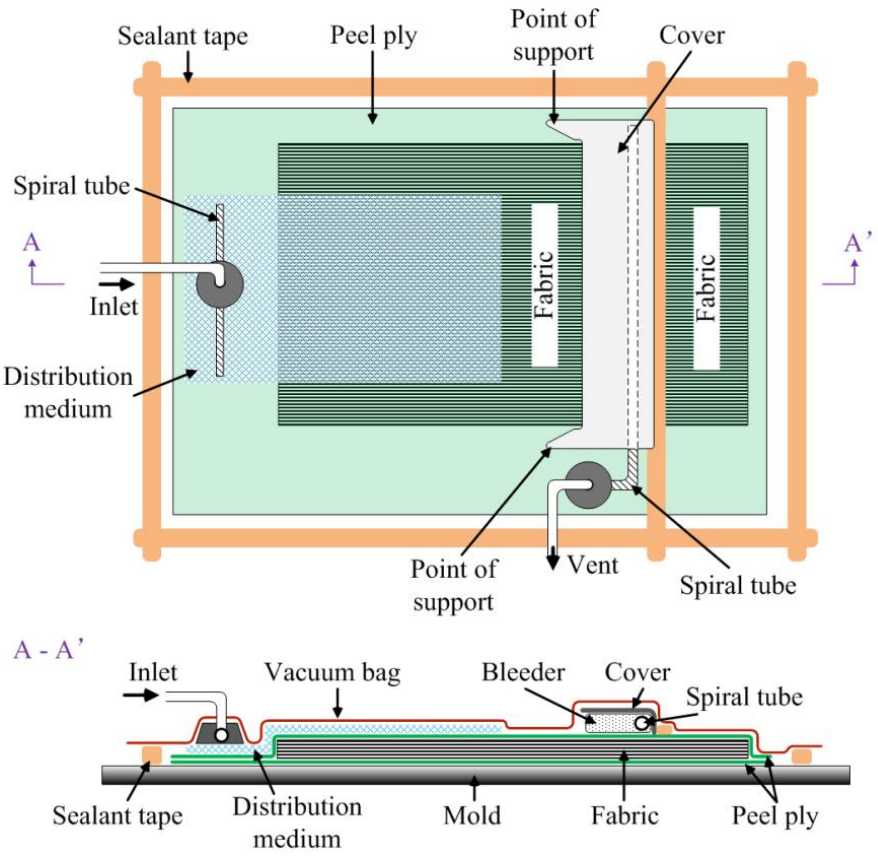

Figure 4-2 Manufacturing process for partially un-molded laminate.

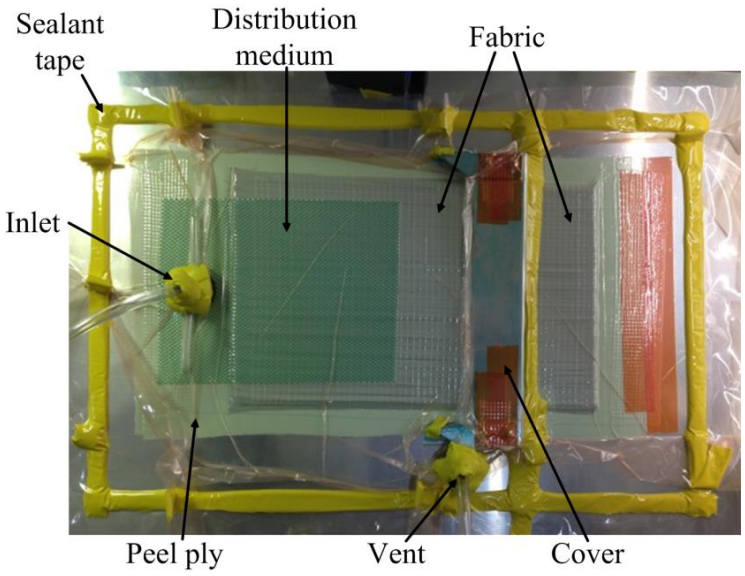

Figure 4-3 Photograph of the fabrication structure of partially un-molded laminates.

laid on the peel ply and then covered by another piece of peel ply. The horizontal direction of Figure 4-2 was the fiber direction. A small piece of distribution medium, a kind of mesh, was placed on the peel ply to promote the flow of resin. The inlet for infusion, which was composed of a rubber connecter and a segment of spiral tube, was positioned on the distribution medium. The entire fabric layer was then divided into two parts by a segment of sealant tape pressed on the peel ply. A curved aluminium cover was pressed onto the sealant tape and was supported by another two points, as shown in Figure 4-2. The distance from the end of the fabric layer to the sealant tape was approximately 5 cm. A segment of spiral tube was positioned in the corner of the cover and connected to a rubber connector, forming the vent for the infusion. The gap between the cover and the fabric layer was filled with a bleeder material. Finally, the entire package was enclosed in a vacuum bag and sealed with tape. Figure 4-3 shows a picture of the adopted structure. After establishing a vacuum, degassed resin was infused from the inlet. After 40 min, the inlet was closed, and the vent was left open until the resin cured. The epoxy resin XNR/H 6815 that could be cured at room temperature was used in the experiment. When the resin cured completely (about 24 hours later), the partially un-molded CFRP laminate was removed from the mold, as shown in Figure 4-1. The thickness of the plate was about 2 mm.

The curved aluminium cover and the bleeder material, as well as the position of the vent, were important to the process. The curved aluminium cover acted as a floodgate to stop the flow of the resin. After establishing a vacuum in the system, the atmospheric pressure on the cover was concentrated at the two support points and at the edge of the curvature, thereby generating a

high pressure that compacted the fabric tightly and further prevented resin flow through the area. Additionally, the space under the cover was used to collect extra resin. The spiral tube extending under the cover was used to extrude the excess resin out through the vent. The bleeder material was also used to absorb and trap any excess resin. The curved aluminium cover did not completely stop the flow of resin and a small quantity of resin flowed over this floodgate. However, in the experiments, the region further than about 5 mm away from the floodgate remained unaffected.

4.2.2 Novel joints

Two novel joints developed from the un-molded laminates were designed and fabricated using a resin-transfer molding process. Figure 4-4 depicts the joint fabrication process. The first joint, the new double-lap joint, was composed of a normal CFRP plate and a partially un-molded laminate. The second joint, the laminated joint, was composed of two partially un-molded laminates. After assembling the plates and arranging the other components, such as the inlet, vent, peel ply, etc., the connecting parts were enclosed in a vacuum bag, as shown inFigure 4-4(a). Figure 4-5(a) shows a photograph of the experimental package. Fabrication of a connected plate with two types of joints [Figure 4-5(b)] was completed after infusion, curing, and de-molding. The infused resin was the same as the resin used to make the partially un-molded laminates.

Figure 4-4(b) shows the details of the new double-lap joint. On the right is a partially un-molded plate, and on the left is a normal CFRP plate. One head of the CFRP plate was

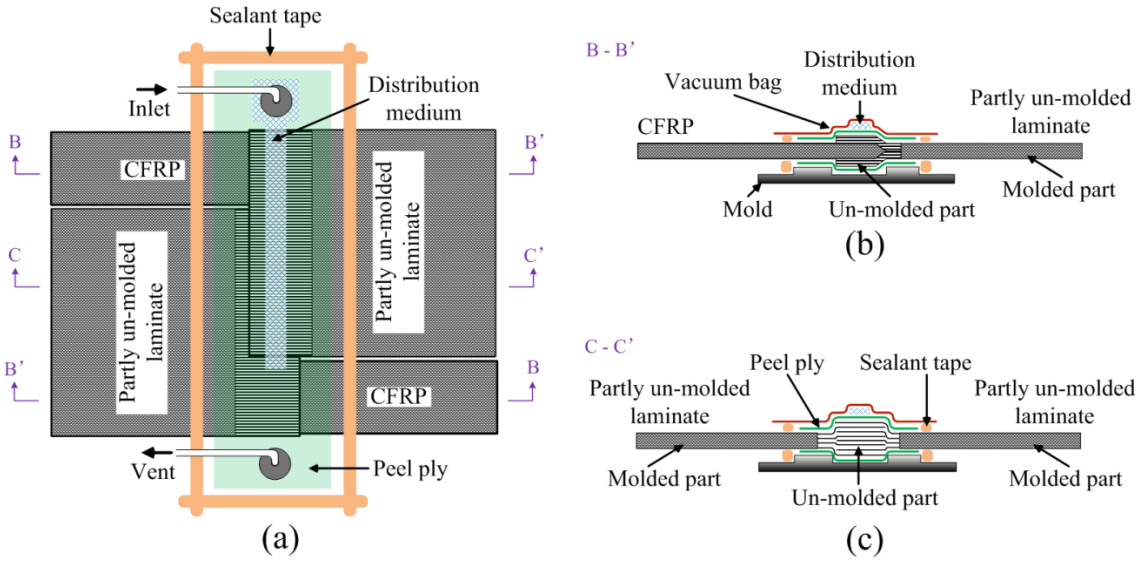

Figure 4-4 (a) Schematic diagram of the joint manufacturing process; (b) detailed depiction of the new double-lap joint; and (c) detailed depiction of the laminated joint.

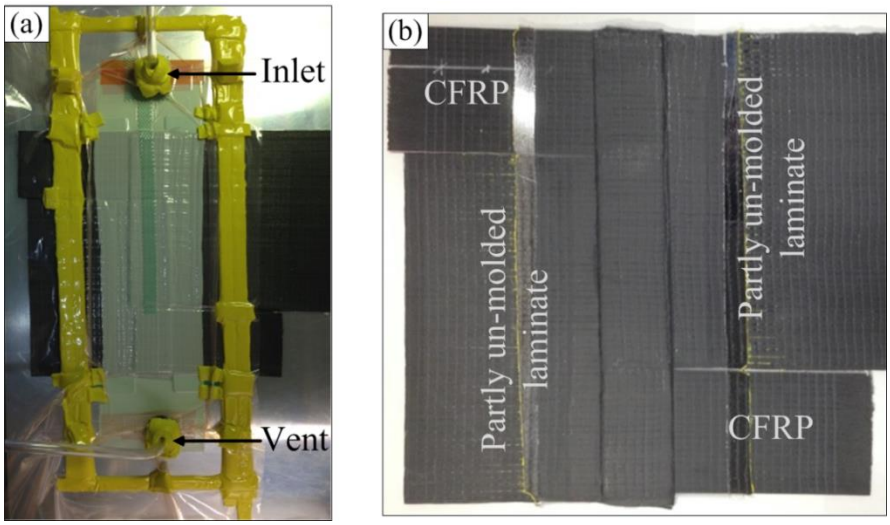

Figure 4-5 (a) Photograph of the structure used for making joints and (b) a connected plate with two types of joints.

inserted into the centre of the un-molded portion of the partially un-molded plate. The inserted head was prepared with two chamfers to reduce stress concentrations. The surface of the inserted part was abraded using a sand-blasting process (#80-sized grit) and then carefully

cleaned with ethanol. After sealing, establishing a vacuum, and resin infusion, the un-molded part was molded, and the two plates were connected. In this joint, there were two contact surfaces between the two plates. The bond length was approximately 4 cm. Figure 4-4(c) shows details of the laminated joint, which was composed of two partially un-molded plates. The two plates were connected by overlapping the un-molded parts with each other. After resin-transfer molding, the two parts were joined. In this joint, there were seven contact surfaces arising from the interfaces between the four fabric layers in each plate. A higher tensile strength was thus expected. The bond length was approximately 4 cm.

To highlight the advantages of the two novel joints, classical double-lap joints with different bond lengths were prepared using plate cut from the partially un-molded plate for comparison. Prior to adhesive bonding, the surfaces of the bonded parts were abraded using a sand-blasting process (#80-sized grit) and then carefully cleaned with ethanol. The bonded lengths were 4 and 8 cm. The nature of the adhesive is critical to the strength of a joint; the fracture toughness and ductility of the adhesive are important factors that influence the joint efficiencies in secondary bonded composite joints [23, 24]. To best directly compare the effects of different structures on joint strength, the adhesive for the classical double-lap joints was the same resin that was used to make the partially un-molded CFRP plate. The four joints are depicted in Figure 4-6.

Static tensile tests were performed to evaluate the four joints. The dimensions of the specimens are shown in Figure 4-7; the length was 250 mm and the width was 10 mm. Two pairs of tabs made with glass fiber-reinforced plastic (GFRP) were used for each specimen to

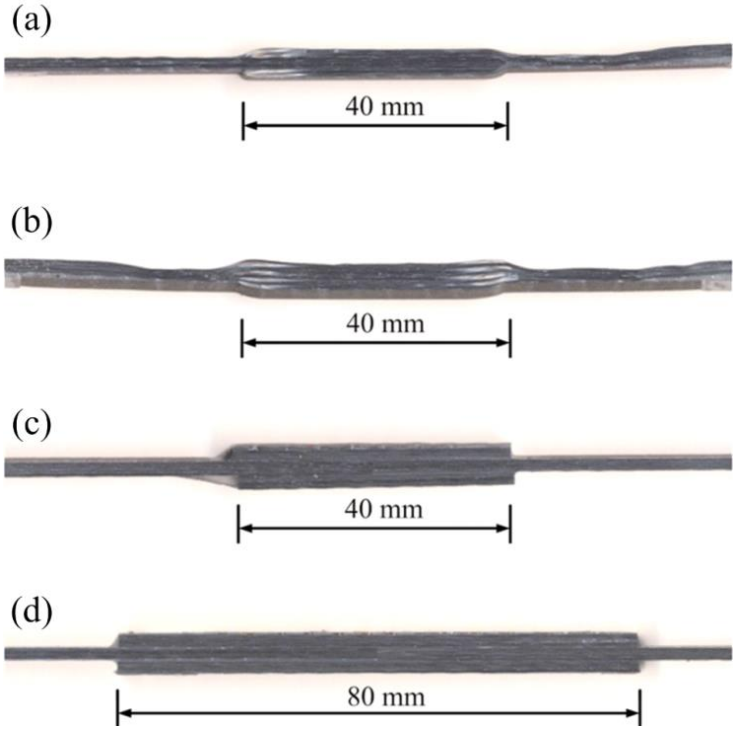

Figure 4-6 Photograph of four types of joints: (a) a new double-lap joint, (b) a laminated joint, (c) a 40-mm long classical double-lap joint, and (d) an 80-mm long classical double-lap joint.

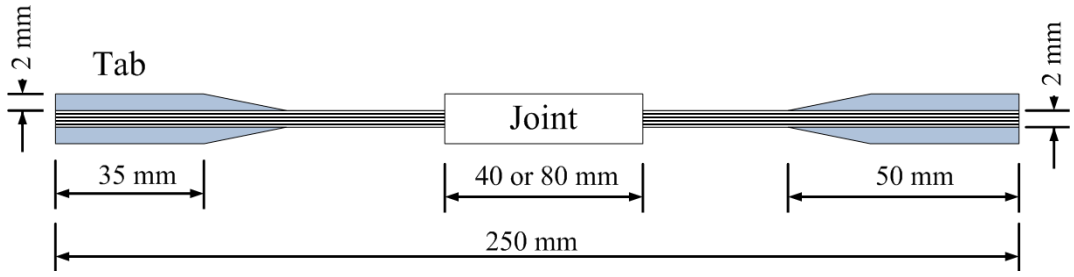

Figure 4-7 Dimensions of specimens used for tensile strength testing.

reduce stress concentrations. The length of the tab was 50 mm. The crosshead speed was 1 mm/min. The tensile stress was along the fiber direction. For the novel joints, at least three samples were tested to get the average tensile strength. Additionally, the tensile strength along the fiber direction of a normal CFRP specimen with the same dimensions was tested as a

reference.

Figure 4-8 presents the tensile strength of the four joints and the normal CFRP material. The final load of the CFRP specimen was 34 kN, indicating that the tensile strength along the fiber direction in the CFRP was 1.7 GPa. The observed strength was much lower in the classical double-lap joint: when the bond length was 4 cm, the average strength was 7.1 kN (the standard deviation was 0.05 kN), similar with the results in [25], and when the bond length was 8 cm (i.e., twice the contact surface), the strength increased by 20% to 8.5 kN (the standard deviation was 0.52 kN). Compared with classical double-lap joints, the new double-lap joint attained a much higher strength of 16.6 kN with a standard deviation of 0.52kN. The laminated joint even exhibited approximately half the strength of the CFRP specimen, reaching 19.8 kN. The standard deviation was 0.57 kN.

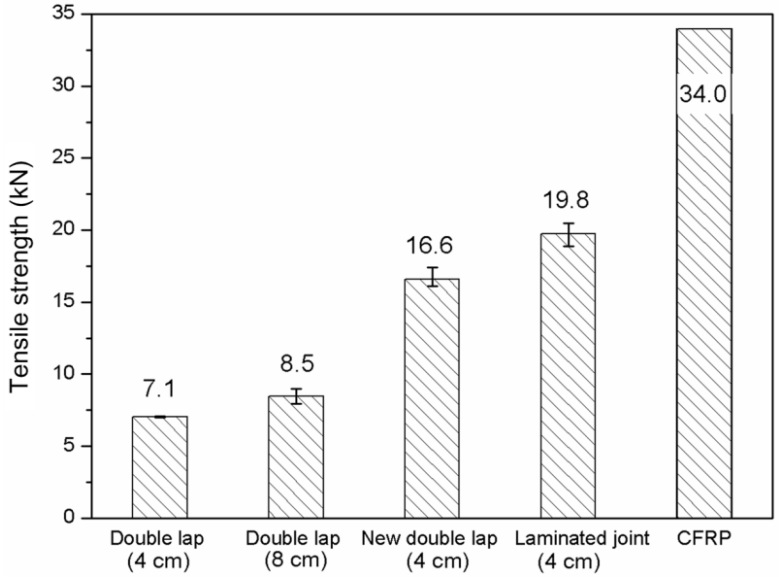

Figure 4-8 Strengths of different joints and the CFRP specimen.

As shown in Figure 4-8, the classical double-lap joint exhibited slightly unusual behaviour at different bond lengths. Typically, the strength of a joint is proportional to the contact area. However, in this study, the strength increased by only 20% when the contact area was doubled. This behaviour could be attributable to two factors. First, only a one-sided mold was used in the manufacturing process; consequently, the CFRP plate produced had only one smooth surface, and the thickness distribution was not uniform. The uneven surface and the mismatch of the thickness between the bonded plates resulted in a relatively thick bondline. Thick bondlines typically decrease the strength of a joint [7]. As the overlap area increases, the mismatch becomes more serious, and the resultant thicker bondline exerts a greater than expected influence on the strength. In addition, greater contact areas also potentially induce more defects. All of these factors are common in engineering practice. Therefore, doubling the contact area does not double the strength. The second possible reason for the lower than expected joint strength is the effective bond length. Zhao [9-11] reported an effective bond length phenomenon in joints between steel plates and CFRP plates. The 8-cm bond length may have already yielded the maximum effective bond length in our material.

The new double-lap joint was much stronger than the classical double-lap joint because it overcame this deficiency. In the new double-lap joint, the use of the un-molded portion of the plate and the VARTM process resulted in a very thin bondline, and solved the problem of thickness mismatch. In addition, the use of VARTM reduced the incidence of defects arising from the hand operation associated with the classical double-lap joint. The laminated joint

exhibited the same advantages; therefore, its strength was much higher than that of the classical double-lap joint. Additionally, the laminated joint possessed a contact area that was 2.5 times greater than the contact area of the new double-lap joint; therefore, the laminated joint can be expected to exhibit much higher strength. However, the strength of the laminated joint was only 19% greater than that of the new double-lap joint. This result will be discussed in the context of the loading process in the next paragraph.

Figure 4-9 and Figure 4-10 contain typical tensile load–displacement curves for the new double-lap joint and the laminated joint. In the new double-lap joint, an initial crack occurred near the tip of the CFRP plate, reducing the slope of the curve. As the load increased, the size of the crack also increased as the fibers covering the tip of the CFRP plate were stretched. At the ultimate load, the joint broke at the interface of the two parts. The laminated joints exhibited similar properties during the tensile test. Initial cracking occurred at both ends of the joint and decreased the modulus of the specimen. The cracks were enlarged due to the increasing tensile load; eventually, de-lamination of the joint resulted when the load reached the strength of the specimen.

As noted, initial cracking occurred at the end of the joint. This behaviour can be explained as follows. In the new double-lap joint, the joined portion of the CFRP plate was sandwiched between the fiber layers. Although the tip of the plate was wedge-shaped, inserting the CFRP plate into the un-molded laminate resulted in curving of the fibers near the tip. After stretching, the fibers straightened, thereby generating a tensile load along the through-thickness direction

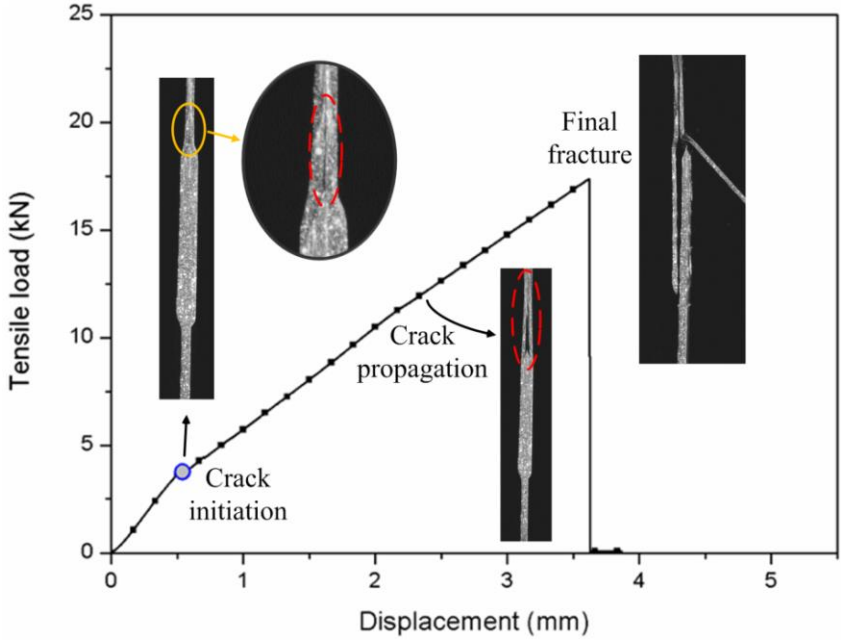

Figure 4-9 Typical load–displacement curve for a new double-lap joint.

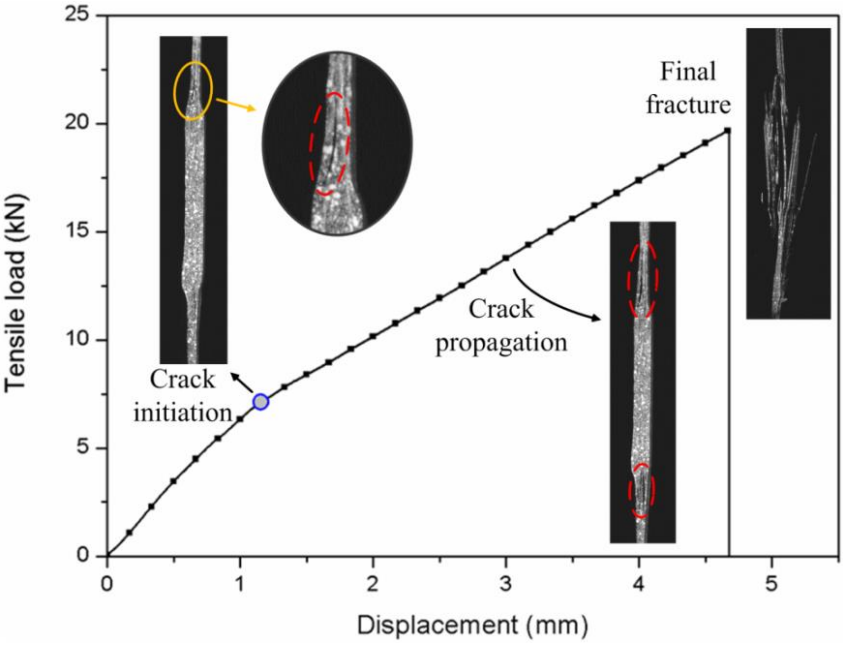

Figure 4-10 Typical load–displacement curve for a laminated joint.

where the strength was very weak [24], leading to initial cracking. The initial cracking behaviour was similar in the laminated joint. Upon initial cracking, the strength of the structure

was mainly determined by the stress concentrations caused by the defect rather than by the stress state of the entire structure. As indicated in Figure 4-9 and Figure 4-10, the load leading to initial cracking of the new double-lap and laminated joints was similar, which could be the reason why the strengths of the two structures were not significantly different. This evidence suggests that if initial cracking can be delayed, the strength might be improved further. In the new double-lap joint, the slope of tip of the CFRP plate could be reduced to decrease the tensile stress along the through-thickness direction. In the laminated joint, prior to overlapping the un-molded parts, every other layer of fabric in the un-molded part could be cut to form a straight joint, thereby eliminating the complex stress state near the ends of the joint.

To investigate the fracture modes of the different joints, the fracture surfaces of the joints were observed using SEM. Figure 4-11 shows the typical fracture surfaces of the classical double-lap joint, the new double-lap joint, and the laminated joint. As shown in Figure 4-11(a), nearly all of the fibers were neatly buried in the resin, indicating that the CFRP plate did not break; consequently, fracture occurred on the CFRP–adhesive interface. This fracture mode was defined as a bondline failure. In the new double-lap joint, a portion of the fractured surface was similar to the fractured surface of the classical double-lap joint, thereby indicating a fracture on the bondline. On the other part, as shown in Figure 4-11(b), some of the fibers were pulled out, and damage was evident on the CFRP plate. This fracture mode was defined as a mixed failure. Figure 4-11(c) shows the fractured surface of the laminated joint. In this case, nearly all of the fibers were pulled out, and the fracture mode was defined as a composite failure.

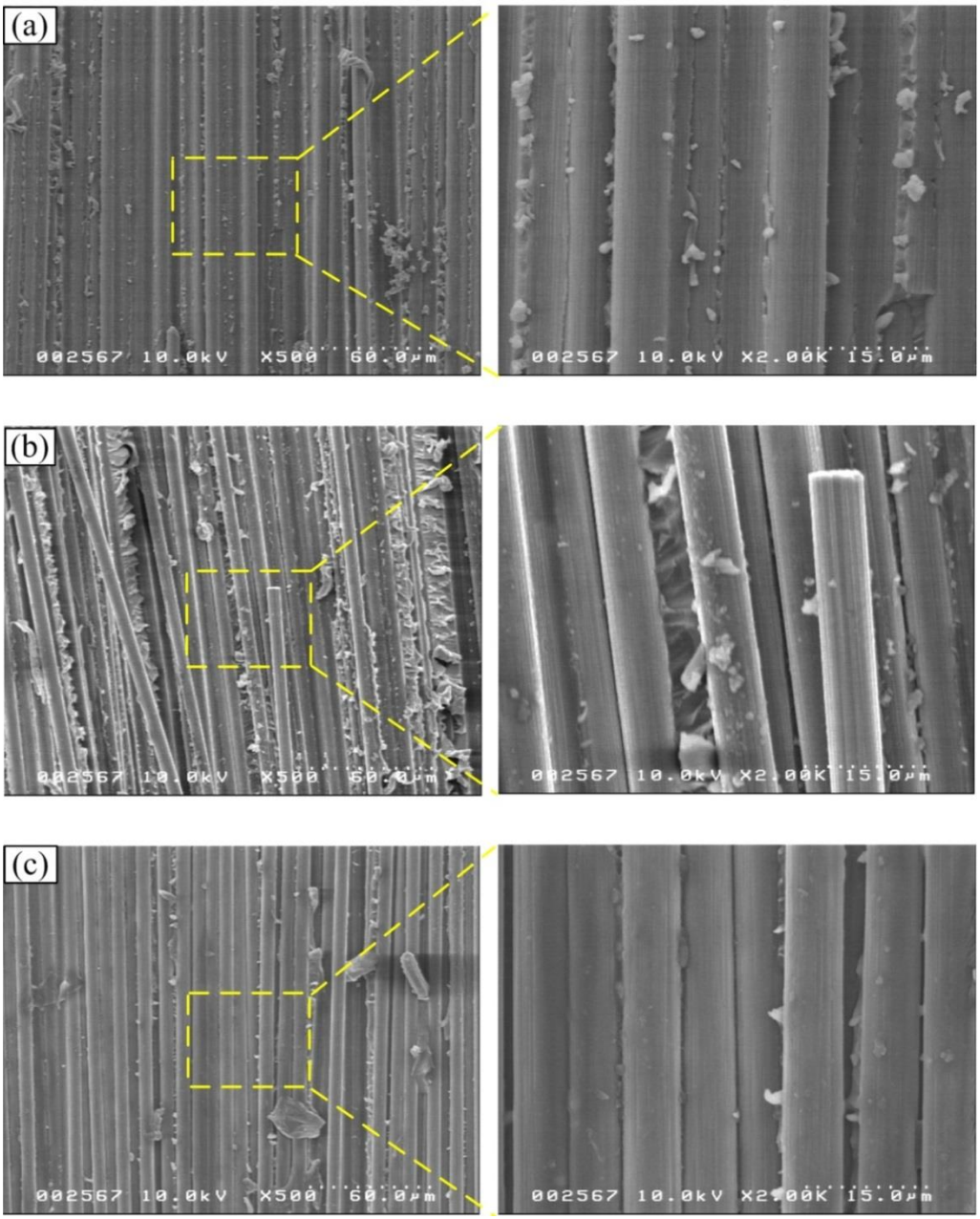

Figure 4-11 Fractured surfaces: (a) classical double-lap joint, (b) new double-lap joint, and (c) laminated joint.

Figure 4-12 illustrates the different fracture modes of the three joints. In a normal joint structure, there are two interfaces: the interface between the CFRP plate and the adhesive and the fiber–matrix interface. In the classical double-lap joint, fracture occurred along the CFRP–

adhesive interface, which indicates that this interface was weaker than the resin and the fiber–matrix interface. In the laminated joint, which was made of un-molded fabric, no CFRP–adhesive interface existed, and the strength of the fiber–matrix interface was typically lower than those of the resin and the fiber. Consequently, fracture occurred at the fiber–matrix interface in the laminated joint. This fracture mode was characteristic of normal CFRP materials [26], and the fracture behaviour indicated that the laminated joint has the potential to exhibit as much strength as a joint-free CFRP plate. The mixed failure observed for the new double-lap joint was attributed to two factors. First, the much thinner bondline in the new double-lap joint exhibited high strength, similar to that of the fiber–matrix interface. Second, the fibers of the un-molded portion attached to the CFRP plate provided a bridging effect between the fibers and adhesive, as reported in [21], thereby improving the strength of the joint.

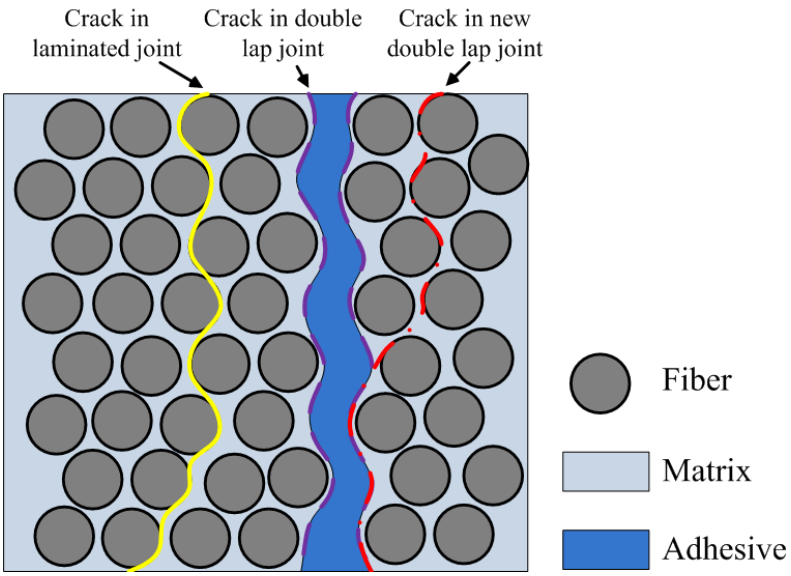

Figure 4-12 Illustration of different fracture modes for the three kinds of joints.

4.2.3 Possible applications

The laminated joint provides much more strength than the classical double-lap joint. However, it is difficult to manufacture the laminated joint structure in practice, especially for a complex structure. With a partially un-molded structure, the new double-lap joint can be easily constructed on a real structure. Consequently, the new double-lap joint is more meaningful in terms of engineering practice.

The novel joints cannot be repaired in a broken CFRP part because there is no un-molded part. They are useful for manufacturing large and complex structures. Although the RTM process can be used to make a complicated composite structure as one piece, some structures should be made piece-by-piece. Take a closed cavity, for example. If the structure is made as one piece, the mold cannot be removed, causing the structure to be much heavier. For some large and symmetric structures, a full-size mold would be very expensive. Constructing these from several small parts could significantly lower the cost. In these cases, the novel joints can provide high-strength connections.

How to obtain the un-molded part may be an issue in a real-life manufacturing setting. For some simple structures, the un-molded part can be obtained using the principles introduced in the “Partially un-molded laminates” subsection, i.e., tightly pressing the fabrics and timely extrusion of the excess resin. For complex structures, two possible methods are proposed here. First, some simple structures with two or more un-molded parts could be made as standard structures to connect two or more complex structures. Second, for an already molded structure,

the resin in the part where the join will be made may be removed using corrosive fluid.

4.2.4 Summary

Partially un-molded laminates were made using a manufacturing process developed from VARTM, and a new double-lap joint and a laminated joint were designed using the partially un-molded laminates. The joints were molded via infusion in a process similar to VARTM. The two novel joints had much higher tensile strength than conventional joints. The strength was twice that of a classical double-lap joint, and about half that of a normal, joint-free CFRP plate. Modification of the shape of the joint could be used to increase the strength of the two novel joints further. The laminated joint was particularly promising. No CFRP–adhesive interfaces existed in the laminated joint; thus, the strength could potentially reach that of normal, joint-free CFRP material.

4.3 Manufacture of wind-lens

A wind-lens is a centrosymmetric structure. In this study, one was made from six one-sixth parts. Each part was molded using VARTM processes based on the same mold. The entire work for making the wind-lens can be divided into two parts: preparation of mold and manufacturing of CFRP parts.

4.3.1 Mold fabrication

A mold for the one-sixth part was constructed in two steps: first a skeleton was constructed, and then the surface was modified with a hard material (Figure 4-13). Similar to building a steel-framed house, a skeleton of the rough structure was built first. Then, the surface was

modified with hard putty to obtain an accurate geometry. Surface 1 in Figure 4-13 is the final required surface. The distance between Surface 1 and Surface 2, which is the interface between the hard cover and the skeleton, was 3 mm.

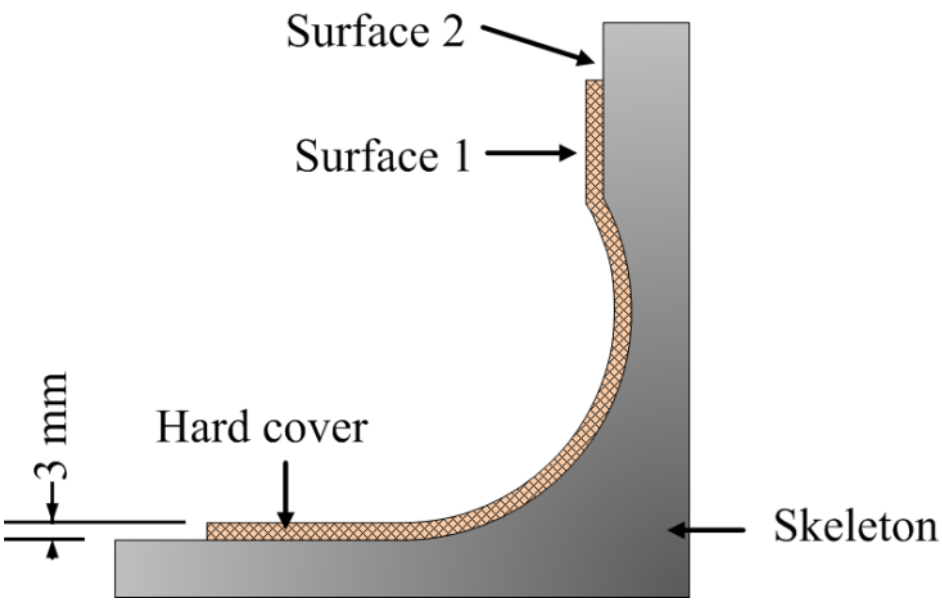

Figure 4-13 Sectional view of the mold structure.

Figure 4-14 shows the procedure used to make the skeleton. The concept was to construct a three-dimensional (3D) mold from two-dimensional (2D) structures. The frame of the skeleton was constructed from wood. A large, flat sheet of wood was cut in an arc to serve as the base of the mold. Several vertical and narrow wooden pieces were connected to the arc, one beside another, to form the basic assembly (Figure 4-14, Steps 1 and 2). Then, the surfaces of the wooden pieces were covered by multiple layers of 5-mm-thick foam sheet (Step 3) according to the required shape of the mold to obtain the semi-finished mold (Step 4).

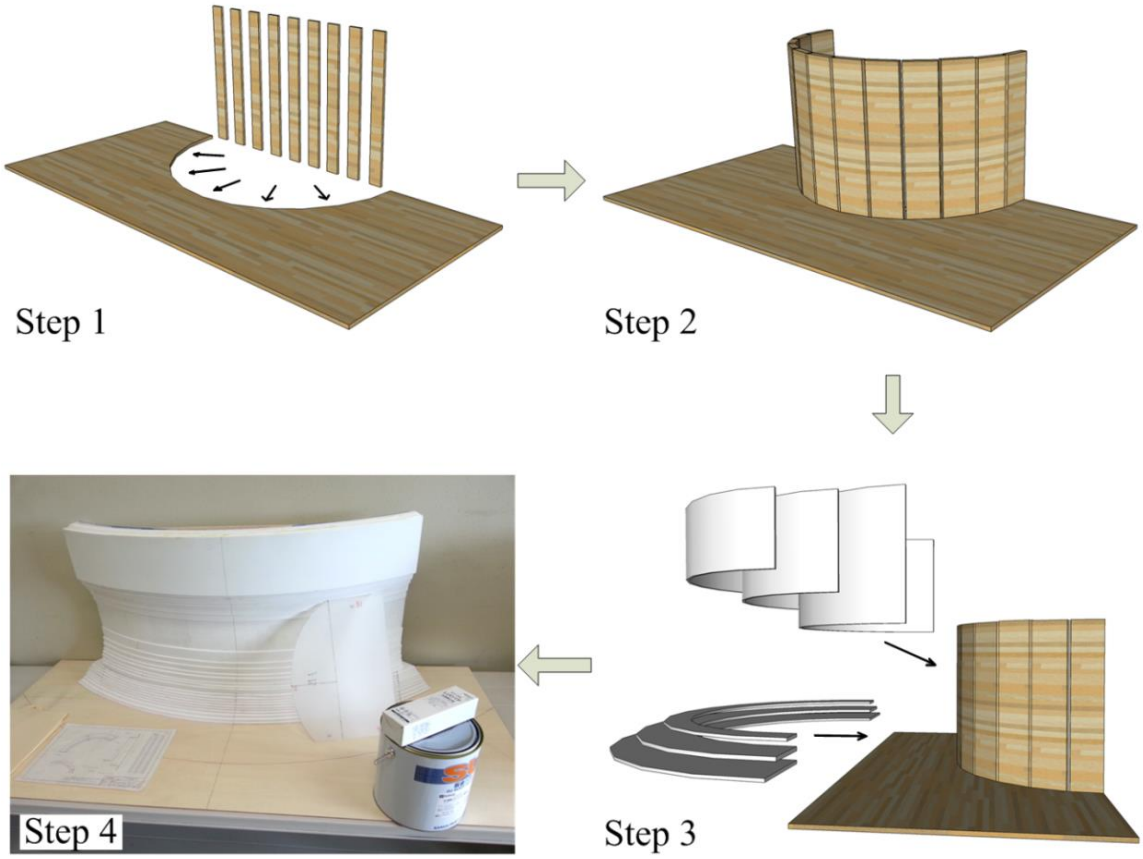

Figure 4-14 Construction of the mold skeleton for a wind-lens.

There were two problems with the semi-finished mold. First, the surface constructed from foam sheets was ladder-like instead of uniformly smooth. Second, the foam sheet was too soft to ensure accurate shape control during the VARTM process. Consequently, the surface of the semi-finished mold needed to be modified.

In Step 1 of the surface-modification process (Figure 4-15), putty used for painting walls was applied to the semi-finished mold to obtain Surface 2 in Figure 4-13. This putty had a long curing time, which enabled careful and meticulous operations. After the putty cured, the surface became smooth and hard, but it was not airtight.

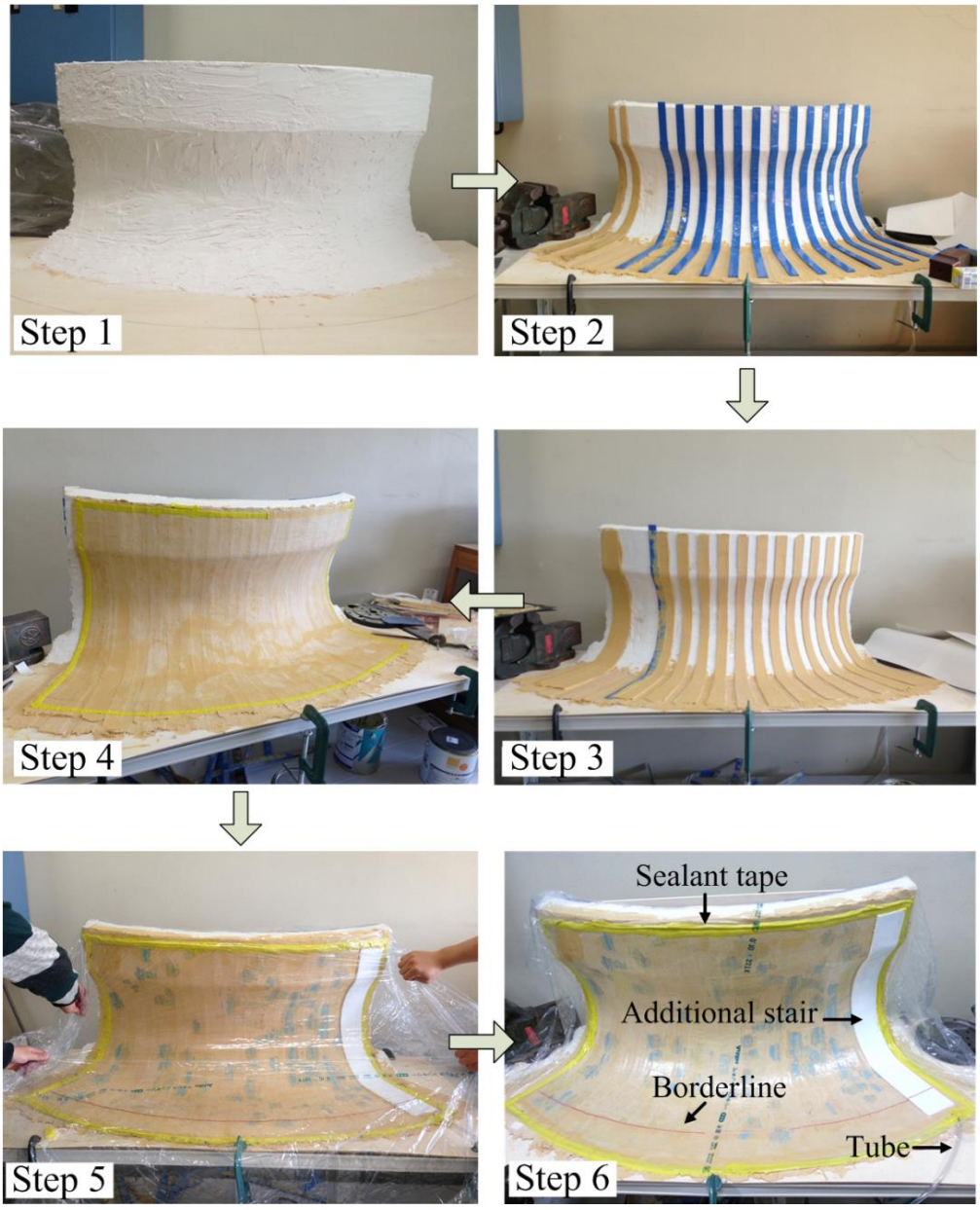

Figure 4-15 Surface preparation of the mold.

In Step 2, 3-mm-thick and 25-mm-wide foam bars were attached to Surface 2 to form channels. These were filled with SU body-filler putty, a type of putty used for car body repair. After the putty cured, the foam bars were removed, leaving channels (Step 3). These new channels were also filled with the same putty. After the putty cured, the final surface was

obtained (Step 4). Although the SU putty could potentially provide an airtight seal, it's very short curing time indirectly affected the quality of the seal. The channels made from the foam bars were designed to guide filling with the putty quickly and accurately. Because the hard putty was applied manually, the presence of gaps in the mold was inevitable; this led to a small amount of leakage from the mold.

In Steps 5 and 6, a high-elongation plastic film was tightly stretched and attached to the mold with sealant tape. The inside was connected with a tube to a vacuum pump. After drawing a vacuum inside, the plastic film was tightly flattened against the mold. The vacuum pump was kept running during the entire VARTM process. The plastic film adopted the topography of the mold surface. The most important feature of the plastic is that it provided an airtight seal. With this technique, it was unnecessary to locate the gaps in the mold and to fill them. Two structures were positioned under the plastic film. One was the border of the one-sixth mold part. A thread with a diameter of about 2 mm was attached to the mold to denote the border. This provided a concave line to guide the cut after the one-sixth mold part was demolded. The other structure was an additional stair. This feature provided the molded part with a concave edge to facilitate assembly. A solid and airtight mold was completed in this way.

4.3.2 Fabricating the wind-lens

Figure 4-16 shows how the one-sixth mold parts were fabricated using the constructed mold. A stack of reinforcement (one layer of stitched [+45°/0°/–45°/90°] carbon fiber fabric from Saertex GmbH & Co. KG), a peel ply, and a distribution medium were placed on the plastic

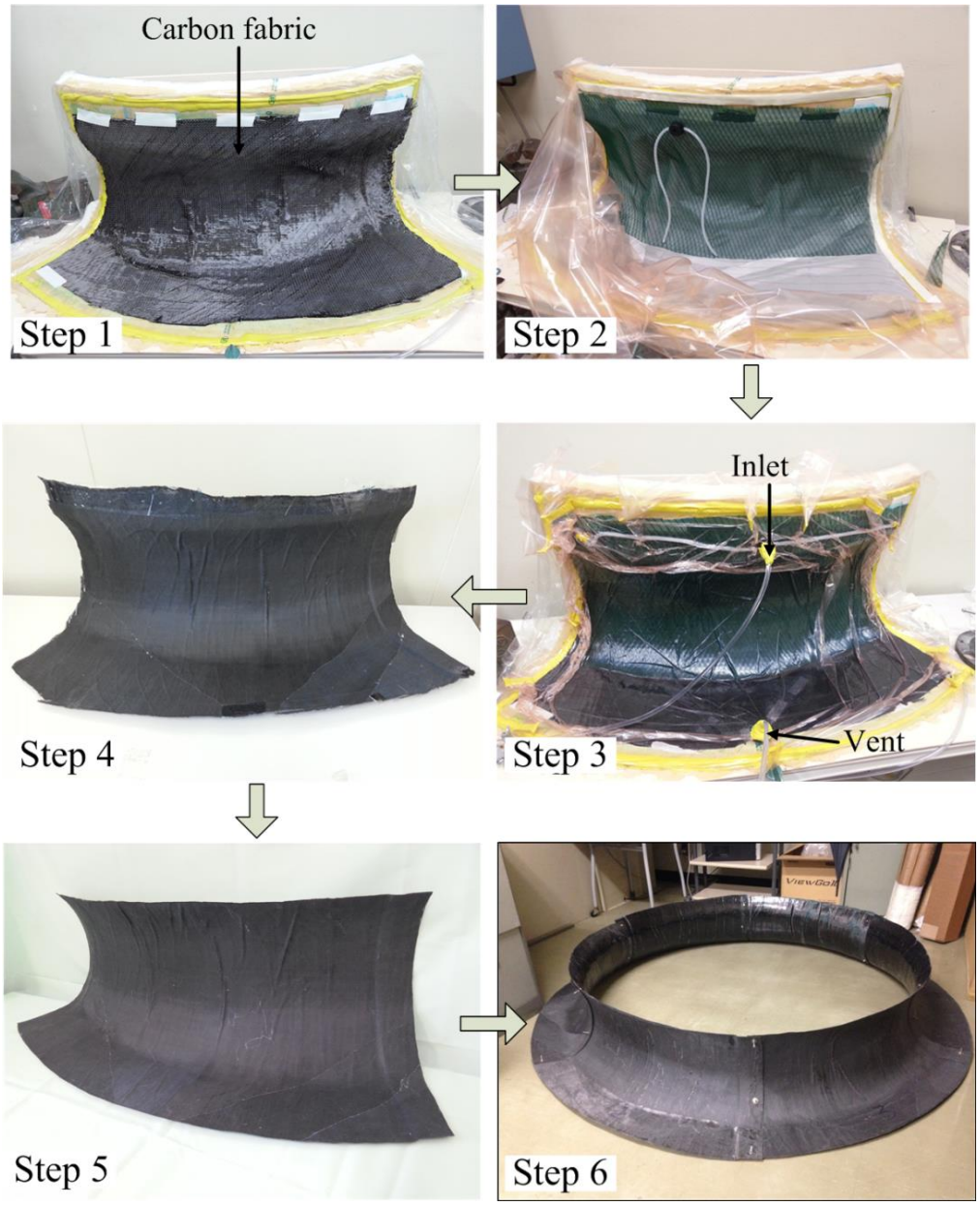

Figure 4-16 Molding of the CFRP wind-lens.

film. This assembly was enclosed in a vacuum bag equipped with an inlet and a vent, and sealed with tape (Figure 4-16, Steps 1 and 2). After resin infusion and resin curing, one-sixth of the CFRP wind-lens was completed (Figure 4-16, Steps 3 and 4). The resin was XNR/H6815 from Nagase & Co., Ltd. After trimming the edge, a standard one-sixth part was obtained (Figure

4-16, Step 5). A full-sized wind-lens was completed by connecting the six parts by bolts (Figure 4-16, Step 6). The success of molding the CFRP wind-lens validated the novel mold-making procedure.

4.3.3 Summary

A simple and low-cost method was used to make a mold for the VARTM process. Only readily available materials were used. The concept of constructing a 3D mold from 2D structures was used to make the skeleton of the mold. Putty applied to the skeleton provided a hard surface. An additional plastic film was used to cover the surface and ensure airtightness. This novel mold-making approach was validated by molding a CFRP wind-lens. Although this method is currently being used in a laboratory environment, it could potentially be used in an industrial production setting.

Bibliography

[1] Wang ZY, Wang L, Guo W, Deng H, Tong JW, Aymerich F. An investigation on strain/stress distribution around the overlap end of laminated composite single-lap joints. Composite Structures. 2009;89(4):589-595.

[2] O'Dwyer DJ, O'Dowd NP, McCarthy CT. Micromechanical investigation of damage processes at composite-adhesive interfaces. Composites Science and Technology. 2013;86(0):61-69.

[3] Liu F, Zhao L, Mehmood S, Zhang J, Fei B. A modified failure envelope method for failure prediction of multi-bolt composite joints. Composites Science and Technology. 2013;83(0):54-63.

[4] Quaresimin M, Ricotta M. Stress intensity factors and strain energy release rates in single lap bonded joints in composite materials. Composites Science and Technology. 2006;66(5):647-656.

[5] Quaresimin M, Ricotta M. Fatigue behaviour and damage evolution of single lap bonded joints in composite material. Composites Science and Technology. 2006;66(2):176-187.

[6] Quaresimin M, Ricotta M. Life prediction of bonded joints in composite materials. International Journal of Fatigue. 2006;28(10):1166-1176.

[7] Tang JH, Sridhar I, Srikanth N. Static and fatigue failure analysis of adhesively bonded thick composite single lap joints. Composites Science and Technology. 2013;86(0):18-25.

[8] Egan B, McCarthy CT, McCarthy MA, Gray PJ, O'Higgins RM. Static and high-rate

loading of single and multi-bolt carbon–epoxy aircraft fuselage joints. Composites Part A: Applied Science and Manufacturing. 2013;53(0):97-108.

[9] Al-Zubaidy H, Al-Mahaidi R, Zhao X-L. Experimental investigation of bond characteristics between CFRP fabrics and steel plate joints under impact tensile loads. Composite Structures. 2012;94(2):510-518.

[10] Fawzia S, Al-Mahaidi R, Zhao X-L. Experimental and finite element analysis of a double strap joint between steel plates and normal modulus CFRP. Composite Structures. 2006;75(1–4):156-162.

[11] Fawzia S, Zhao XL, Al-Mahaidi R, Rizkalla S. Bond characteristics between CFRP and steel plates in double strap joints. International Journal of Advanced Steel Construction. 2005;1(2):17-27.

[12] Jeong K-W, Park Y-B, Choi J-H, Kweon J-H. A study on the failure mode and load of the composite key joint. Journal of Composite Materials. 2013.

[13] Zhao X-L, Zhang L. State-of-the-art review on FRP strengthened steel structures. Engineering Structures. 2007;29(8):1808-1823.

[14] Katnam KB, Comer AJ, Stanley WF, Buggy M, Ellingboe AR, Young TM. Characterising pre-preg and non-crimp-fabric composite single lap bonded joints. International Journal of Adhesion and Adhesives. 2011;31(7):679-686.

[15] Feih S, Shercliff HR. Adhesive and composite failure prediction of single-L joint structures under tensile loading. International Journal of Adhesion and Adhesives. 2005;25(1):47-59.

[16] Kim K-S, Yi Y-M, Cho G-R, Kim C-G. Failure prediction and strength improvement of uni-directional composite single lap bonded joints. Composite Structures. 2008;82(4):513-520.

[17] Greenhalgh ES. Failure analysis and fractography of polymer composites. UK: Woodhead Publishing; 2009.

[18] Dvorak GJ, Zhang J, Canyurt O. Adhesive tongue-and-groove joints for thick composite laminates. Composites Science and Technology. 2001;61(8):1123-1142.

[19] Kim HS, Park SW, Lee DG. Smart cure cycle with cooling and reheating for co-cure bonded steel/carbon epoxy composite hybrid structures for reducing thermal residual stress. Composites Part A: Applied Science and Manufacturing. 2006;37(10):1708-1721.

[20] Sun Z, Jeyaraman J, Sun S, Hu X, Chen H. Carbon-fiber aluminum-foam sandwich with short aramid-fiber interfacial toughening. Composites Part A: Applied Science and Manufacturing. 2012;43(11):2059-2064.

[21] Choi I, Lee DG. Surface modification of carbon fiber/epoxy composites with randomly oriented aramid fiber felt for adhesion strength enhancement. Composites Part A: Applied Science and Manufacturing. 2013;48(0):1-8.

[22] Park SW, Lee DG. Strength of Double Lap Joints Bonded With Carbon Black Reinforced Adhesive Under Cryogenic Environment. Journal of Adhesion Science and Technology. 2009;23(4):619-638.

[23] Chen D, Arakawa K, Xu C. Reduction of void content of vacuum-assisted resin transfer molded composites by infusion pressure control. Polymer Composites. 2014:n/a-n/a.

[24] Katnam KB, Dhôte JX, Young TM. Experimental Analysis of the Bondline Stress Concentrations to Characterize the Influence of Adhesive Ductility on the Composite Single Lap Joint Strength. The Journal of Adhesion. 2013;89(6):486-506.

[25] Löbel T, Kolesnikov B, Scheffler S, Stahl A, Hühne C. Enhanced tensile strength of composite joints by using staple-like pins: Working principles and experimental validation. Composite Structures. 2013;106(0):453-460.

[26] Chen D, Lu F, Jiang B. Tensile properties of a carbon fiber 2D woven reinforced polymer matrix composite in through-thickness direction. Journal of Composite Materials. 2012;46(26):3297-3309.

CHAPTER 5

Conclusions and future works

This chapter summarizes the main conclusions of this dissertation and describes possible future major research topics related to this study.

5.1 Conclusions

A VARTM process was established to allow the fabrication of a high-strength, lightweight wind-lens power system. A rounded complete research project was undertaken to fabricate high-quality CFRP structures; this included developing basic testing techniques to evaluate composite materials, designing improvements to the VARTM process, and applying VARTM to fabricate a wind-lens. The main conclusions of this research can be summarized as follows.

1. A digital image analysis technique was used successfully to estimate the void content of a fiber-reinforced composite. Based on the different gray levels and geometric characteristics, voids were imaged correctly from a black and white micrograph of a specimen. The ratio between the void area and the size of the micrograph was used to estimate the void content of a sample. A 2D-DIC technique was used to estimate the distribution of the fiber volume fraction in a CFRP plate by measuring the area CTE of samples. A full-field thickness-change monitoring system was established using a 3D-DIC technique. This system provided a full-field thickness evaluation of the vacuum package in a VARTM process.
2. Methods were proposed to improve the conventional VARTM process to achieve a lower void content and higher fiber volume fraction CFRP material. Two main sources of voids were experimentally identified: non-uniform resin flow and continuous evaporation of resin under low pressure. A simple yet effective modification to the operation was proposed to reduce the effects of these two factors, i.e., setting the full

vacuum of the equipment at the vent from the beginning of infusion and switching the pressure to a slightly higher value after the resin finished saturating the entire reinforcement. Void content measurements validated the approach. In the VARTM process, the fiber volume fraction is determined by the amount of resin, depending on the infused resin less the extruded amount. A cover mold was proposed for the vacuum package in VARTM to promote resin flow and achieve a higher fiber volume fraction. The effects of a cover mold are three-fold. First, in the filling stage, a rigid cover mold can prevent shrinkage of the part at the resin flow front, and even force the unsaturated part to slightly expand, making the resin easier to flow, and thereby shortening the time required for complete infusion. Second, the cover mold can prevent large expansion of the fully saturated part, which restricts the amount of excess resin that can be stored in the fully saturated part. Finally, in the post-filling stage, the cover mold can accelerate extrusion of the excess resin. Because of these effects, the modified VARTM process can provide a final product with a higher fiber volume fraction.

3. Two applications were attempted using VARTM processes. The first is two novel joints for composite structures. Partially un-molded laminates were made using a manufacturing process developed from VARTM, and a new double-lap joint and a laminated joint were designed using the partially un-molded laminates. The joints were molded via infusion in a process similar to VARTM. The two novel joints had much higher tensile strength than conventional joints. The strength was twice that of a

classical double-lap joint, and about half that of a normal, joint-free CFRP plate. Modification of the shape of the joint could be used to increase the strength of the two novel joints further. The laminated joint was particularly promising. No CFRP–adhesive interfaces existed in the laminated joint; thus, the strength could potentially reach that of normal, joint-free CFRP material. The importance of the manufacturing process for partially un-molded laminates should be emphasis once more; in the absence of partially un-molded laminates, the two novel joints would be impossible to implement in engineering practice. The second is the successful application on making a wind-lens. A simple and low-cost method was used to make a mold for the VARTM process. Only readily available materials were used. The concept of constructing a 3D mold from 2D structures was used to make the skeleton of the mold. Putty applied to the skeleton provided a hard surface. An additional plastic film was used to cover the surface and ensure airtightness. This novel mold-making approach was validated by molding a CFRP wind-lens. Although this method is currently being used in a laboratory environment, it could potentially be used in an industrial production setting.

5.2 Future works

Although I will soon finish my doctoral program, in my opinion, this research is not complete. There are still some points deserving more effort and further research.

1. In Section 2.3, it was only shown that the CTE can be evaluated using 2D-DIC to estimate the fiber volume fraction distribution in a CFRP plate. If an accurate

relationship between the CTE and fiber volume fraction can be established, then the fiber volume fraction could be determined directly using the same technique.

2. In Section 2.4, the thickness change during the resin infusion step was calculated after the process was finished. Consequently, this system is only allows a post-fabrication analysis. If a real-time monitoring system could be established, it would be helpful for controlling the VARTM process.

3. As described in Section 4.2, novel joints resulting from modified structures have the potential to achieve higher strength. And, these joints were not used in the fabricated wind-lens. Further research is required to determine how best to improve the strength of the joints and how to apply them to a wind-lens.

LIST OF FIGURES

LIST OF TABLES

LIST OF PUBLICATIONS

Journal papers

[1] Chen DD, Xu CH, Yoon S-J, Jiang SY, Matsumoto R, Shen YY, et al. A Method for Making a Large and Complex Mold for Vacuum-Assisted Resin Transfer Molding. International Journal of Advanced Manufacturing Technology. (Under review)

[2] Chen DD, Arakawa K, Uchino M. Effects of the Addition of a Cover Mold on Resin Flow and the Quality of the Finished Product in Vacuum-Assisted Resin Transfer Molding. Polymer Composites. (Under review)

[3] Chen DD, Yoon S-J, Arakawa K, Uchino M. Laminate thickness evolution during the resin infusion step of VARTM. Advanced Composites Letters. (Accepted)

[4] Yoon S-J, Chen DD, Gu J-U, Choi N-S, Arakawa K, AE analysis of delamination crack propagation in laminated material. Journal of Mechanical Science and Technology. 2014. (Accepted)

[5] Chen DD, Arakawa K, Jiang SY. Novel joints developed from partially un-moulded carbon-fibre-reinforced laminates. Journal of Composite Materials. (Published online)

[6] Chen DD, Arakawa K, Xu CH. Reduction of void content of vacuum-assisted resin transfer molded composites by infusion pressure control. Polymer Composites. (Published online)

[7] Chen DD, Matsumoto R, Arakawa K, Yoon S-J. Energy absorption property of CFRP under impact loadings. Applied Mechanics and Materials. 2014; 566: 219-224.

[8] Chen DD, Arakawa K, Uchino M, Xu CH. Application of Digital Image Correlation

Technique on Vacuum Assisted Resin Transfer Molding Process and Performance Evaluation of the Produced Materials. International Journal of Mechanical, Industrial Science and Engineering. 2014;8(1):93-98.

[9] Yoon S-J, Chen DD, Gu J-U, Choi N-S, Arakawa K. Interlaminar Fracture Testing Method for CFRP Using Tensile Loading with Acoustic Emission Analysis. International Journal of Fracture. 2014;187(1):173-178.

[10] Chen DD, Lu F, Lin Y, Jiang B. Effects of Strain Rate and Temperature on Compressive Properties of an Aluminized PBX. Chinese Journal of High Pressure Physics. 2013;27(3):361-366. (In Chinese)

[11] Chen DD, Lu F, Jiang B. Tensile properties of a carbon fiber 2D woven reinforced polymer matrix composite in through-thickness direction. Journal of Composite Materials. 2012;46(26):3297-3309.

Conferences

[1] Chen DD, Arakawa K, Uchino M, Xu CH. Application of digital image correlation technique on vacuum assisted resin transfer molding process and performance evaluation of the produced materials. 2014 International Conference on Composite Materials, Dubai, UAE2014.

[2] Chen DD, Arakawa K, Uchino M. Monitoring of resin transfer in CFRP molding using 3D-DIC technique. International Conference on Experimental Mechanics 2013 and The Twelfth Asian Conference on Experimental Mechnics, Bangkok Thailand2013.

[3] Chen DD, Matsumoto R, Arakawa K, Yoon S-J. Energy absorption property of CFRP under impact loadings. The 8-th International Symposium on Impact Engineering (ISIE2013) Program, Osaka, Japan2013.

[4] Yoon S-J, Chen DD, Gu J-U, Choi N-S, Arakawa K. Fracture characteristic of laminated material fabricated by VaRTM method. The 88th Ordinary Conference of Kansai Branch of JSME, Osaka2013.

[5] Xu CH, Chen DD, Arakawa K. Application of digital image correlation technique on performance evaluation of FRP materials. The 15th Cross Straits Symposium on Energy and Environmental Science and Technology (CSS-EEST15), Shanghai, China2013.

[6] Jiang SY, Arakawa K, Chen DD. Digital image analysis on void content calculation. The 15th Cross Straits Symposium on Energy and Environmental Science and Technology (CSS-EEST15), Shanghai, China2013.

[7] Chen DD, Arakawa K. Flexural Properties of VARTM Manufactured CFRP Plate. The 9th International Conference on Fracture & Strength of Solids, Jeju, Korea2013.

[8] Yoon S-J, Chen DD, Gu J-U, Choi N-S, Arakawa K. AE analysis of delamination crack propagation in laminated material. The 9th international Conference on Fracture & Strength of Solids (FEOFS 2013), Jeju, Korea2013.

[9] Chen DD, Arakawa K. Mechanical properties of a VARTM manufactured 2D carbon woven/expoxy composite. The 8th International Forum on Advanced Material Science and Technology, Fukuoka, Japan2012.

ACKNOWLEGEMENTS

This study was carried out at Kyushu University during the years 2011–2014. I wish to express my gratitude to all those who helped me during my studies.

First and foremost, I would like to show my deepest gratitude to my supervisor, Prof. Kazuo Arakawa. I appreciate his instruction style for a Ph.D. student: setting up a final target, then giving me the maximum freedom to design and carry out my research while providing illuminating direction on key problems. During my work, I began to understand what real research is, how to find a valuable research topic, and how to study it gradually. Prof. Arakawa also taught me how to construct a story and how to make my expression clear to produce a high-quality manuscript. Without his consistent and patient instruction, this dissertation would not have reached its present form. His direction will help guide me continuously in my future work.

Because I entered the doctoral program at Kyushu University without finishing my studies for a Masters degree, I did not have a chance to express my thanks to my Masters course supervisor, Prof. Fangyun Lu, and her research group. I would like to do so here. Under their guidance, I established a solid foundation to perform various types of mechanic experiments. Without these skills, I could not have finished my doctoral program so smoothly.

I extend my thanks to Prof. Wenxue Wang and Mr. Terutake Matsubara for their permission to use equipment in their laboratory and for providing instruction on how to use it. I also thank Mr. Minoru Zenin, the technical assistant in the workshop, for his help in processing materials

for my experiments. My gratitude extends to the other members of our laboratory, too, for their cooperation with my studies and their friendship.

My gratitude is also due to my dissertation committee members for helpful suggestions and comments during their review.

As an international student, extracurricular life is also important. I appreciate the International Education Promotion Program headed by Mrs. Keiko James for organizing many activities for us to enjoy life in Japan and to experience Japanese culture. I also appreciate my friends here for comforting me when I felt alone and missed my family.

I thank my family for their various forms of encouragement and support. In particular, I thank my wife, Ying Peng. She remained in China working alone, and is now pregnant.

Finally, I acknowledge China Scholarship Council for financial support and the National University of Defense Technology for providing me with an opportunity to study in Japan.